

1 Ensovibep, a novel trispecific DARPIn candidate that protects against 2 SARS-CoV-2 variants

3 Sylvia Rothenberger^{1,2,*}, Daniel L. Hurdiss^{4,5,*}, Marcel Walser^{3,*}, Francesca Malvezzi^{3,*}, Jennifer Mayor^{1,2},
4 Sarah Ryter¹, Hector Moreno², Nicole Liechti¹, Andreas Bosshart³, Chloe Iss³, Valérie Calabro³, Andreas
5 Cornelius³, Tanja Hospodarsch³, Alexandra Neculcea³, Tamar Looser³, Anja Schlegel³, Simon Fontaine³,
6 Denis Villemagne³, Maria Paladino³, Yvonne Kaufmann³, Doris Schaible³, Iris Schlegel³, Dieter Schiegg³,
7 Christof Zitt³, Gabriel Sigrist³, Marcel Straumann³, Feyza Sacarcelik³, Julia Wolter³, Marco Comby³, Julia
8 M. Adler⁹, Kathrin Eschke⁹, Mariana Nascimento⁹, Azza Abdelgawad⁹, Achim D. Gruber¹⁰, Judith Bushe¹⁰,
9 Olivia Kershaw¹⁰, Heyrhyoung Lyoo⁴, Chunyan Wang⁴, Wentao Li⁴, Ieva Drulyte⁶, Wenjuan Du⁴, H. Kaspar
10 Binz⁷, Rachel Herrup⁸, Sabrina Lusvardi⁸, Sabari Nath Neerukonda⁸, Russell Vassell⁸, Wei Wang⁸,
11 Susanne Mangold³, Christian Reichen³, Filip Radom³, Charles G. Knutson¹¹, Kamal K. Balavenkatraman¹²,
12 Krishnan Ramanathan¹³, Seth Lewis³, Randall Watson³, Micha A. Haeuptle³, Alexander Zürcher³, Keith
13 M. Dawson³, Daniel Steiner³, Carol D. Weiss⁸, Patrick Amstutz³, Frank J.M. van Kuppeveld⁴, Michael T.
14 Stump^{3,14,**}, Berend-Jan Bosch^{4,**}, Olivier Engler^{1,**}, Jakob Trimpert^{9,**}

15

16 * These first authors contributed equally to this work

17 ** These senior authors contributed equally to this work

18 ¹Spiez Laboratory, Austrasse, 3700 Spiez, Switzerland

19 ²Institute of Microbiology, University Hospital Center and University of Lausanne, Rue du Bugnon 48,
20 1011 Lausanne, Switzerland

21 ³Molecular Partners AG, Wagistrasse 14, 8952 Zurich-Schlieren, Switzerland

22 ⁴Department Biomolecular Health Sciences, Division Infectious Diseases & Immunology - Virology
23 section, Faculty of Veterinary Medicine, Utrecht University, 3584 CL, Utrecht, The Netherlands.

24 ⁵Cryo-Electron Microscopy, Bijvoet Center for Biomolecular Research, Department of Chemistry,
25 Faculty of Science, Utrecht University, Padualaan 8, 3584 CH Utrecht, The Netherlands

26 ⁶Materials and Structural Analysis, Thermo Fisher Scientific, Eindhoven, 5651 GG, The Netherlands.

27 ⁷Binz Biotech Consulting, Lüssirainstrasse 52, 6300 Zug, Switzerland

28 ⁸Laboratory of Immunoregulation, Division of Viral Products, Center for Biologics Evaluation and
29 Research, U.S. Food and Drug Administration, Silver Spring, Maryland, USA

30 ⁹Freie Universität Berlin, Institut für Virologie, Robert-von Ostertag-Straße 7-13, 14163 Berlin, Germany

31 ¹⁰Freie Universität Berlin, Institut für Tierpathologie, Robert-von Ostertag-Straße 15, 14163 Berlin,
32 Germany

33 ¹¹Novartis Institutes for BioMedical Research, PK Sciences, Cambridge, MA, USA

34 ¹²Novartis Institutes for BioMedical Research, Preclinical Safety, Basel, Switzerland

35 ¹³Novartis Pharma AG, Basel, Switzerland

36

37 ¹⁴To whom correspondence should be addressed:

38 Michael T. Stumpp

39 +41 44 755 77 00

40 info@molecularpartners.com

41

42 **Keywords:** SARS-CoV-2, COVID-19, coronavirus, mutations, emerging variants, antiviral therapy,
43 ensovibep, MP0420, DARPin drug, ankyrin repeat protein, DARPin, multispecific, K417N, K417T, L452R
44 E484K, N501Y, B.1.1.7, B.1.1.529, B.1.351, P.1, B.1.429, B.1.526, B.1.617, B.1.618, B.1.621, AY.1, alpha,
45 beta, gamma, delta, mu, omicron, Roborovski dwarf hamster

46

47 **Conflict of interests:** authors from Molecular Partners own performance share units and/or stock of the
48 company. H.K.B. owns stock of the company. I.D. is an employee of Thermo Fisher Scientific. C.G.K.;
49 K.K.B. and K.R. are employees of Novartis. The other authors declare no competing interests.

50 **Abstract**

51 SARS-CoV-2 has infected millions of people globally and continues to undergo evolution. Emerging
52 variants can be partially resistant to vaccine induced immunity and therapeutic antibodies, emphasizing
53 the urgent need for accessible, broad-spectrum therapeutics. Here, we report a comprehensive study
54 of ensovibep, the first trispesific clinical DARPIn candidate, that can simultaneously engage all three
55 units of the spike protein trimer to potently inhibit ACE2 interaction, as revealed by structural analyses.
56 The cooperative binding of the individual modules enables ensovibep to retain inhibitory potency
57 against all frequent SARS-CoV-2 variants, including Omicron BA.1 and BA.2, as of February 2022.
58 Moreover, viral passaging experiments show that ensovibep, when used as a single agent, can prevent
59 development of escape mutations comparably to a cocktail of monoclonal antibodies (mAb). Finally,
60 we demonstrate that the very high in vitro antiviral potency also translates into significant therapeutic
61 protection and reduction of pathogenesis in Roborovski dwarf hamsters infected with either the SARS-
62 CoV-2 wild-type or the Alpha variant. In this model, ensovibep prevents fatality and provides substantial
63 protection equivalent to the standard of care mAb cocktail. These results support further clinical
64 evaluation and indicate that ensovibep could be a valuable alternative to mAb cocktails and other
65 treatments for COVID-19.

66 Introduction

67 The extent of the COVID-19 pandemic allowed SARS-CoV-2 to quickly undergo adaptive evolution. The
68 main mutations localize to the spike protein, a metastable prefusion trimer on the viral membrane that
69 mediates virus entry into the host cell. The spike protein comprises multiple functional subunits: S1,
70 which includes the N-terminal domain (NTD) and the receptor binding domain (RBD), responsible for
71 interaction with the angiotensin-converting enzyme 2 (ACE2) host receptor¹⁻⁴, and the S2 subunit,
72 which is responsible for virus-host cell membrane fusion via extensive, irreversible conformational
73 changes⁵⁻⁸. In the first months of the pandemic, a single mutation, D614G, located in the S2 domain,
74 became prevalent. This mutation impairs premature conformational change of the spike protein, thus
75 increasing the number of infectious viral particles and therefore overall viral infectivity⁹. By November
76 2021, more viral lineages have been identified and designated as Variants of Interest (VOIs) or Variants
77 of Concern (VOCs) based on their associated increased risk to public health. These were first isolated in
78 the UK (Alpha, B.1.1.7 lineage), South Africa (Beta, B.1.351), Brazil (Gamma, P.1), South California
79 (Epsilon, B.1.429), Nigeria (Eta, B.1.525), New York, (Iota, B.1.526), Peru (Lambda, C.37), Japan (R.1),
80 India (Kappa, B.1.617.1 and Delta, B.1.617.2), Uganda (A.23.1), and, more recently, in Colombia (Mu,
81 B.1.621), the UK (Delta Plus, AY.1), as well as Africa (Omicron, B.1.1.529)¹⁰⁻²².

82 Many of these variants harbor mutations in the RBD domain of the spike protein, mainly in the ACE2
83 binding site (K417T/N, N439K, L452R, E484K/Q, N501Y). Since this region is also highly immunogenic,
84 these mutations have been linked to a dual effect: either increasing the affinity to the human ACE2
85 receptor (N439K, N501Y) and therefore transmissibility, and/or facilitating immune escape of the virus
86 (K417T/N, L452R, E484K/Q)^{10,11,15-17,23-25}. In particular, the E484K substitution has been shown to play a
87 key role in attenuating the potency gain and resistance to the majority of antibodies, according to a
88 study analyzing clinical-stage therapeutic antibodies¹².

89 Fighting the COVID-19 pandemic requires a coordinated global effort to maximize the benefits of
90 vaccinations and therapeutics¹. The presence of an unvaccinated portion of the population and the
91 evolution of escape mutants highlights the medical need for globally accessible therapeutics²⁶.
92 Neutralizing mAbs are a critically important therapeutic approach against COVID-19. To circumvent
93 their loss of potency due to viral mutational escape, antibody cocktails were generated to provide
94 increased protection against variants²⁷⁻²⁹.

95 We have applied the DARPIn platform³⁰, which allows fast generation and cost-effective production of
96 biological therapeutics, to generate ensovibep, an anti-SARS-CoV-2 multispecific DARPIn antiviral
97 clinical candidate^{31,32}. DARPIns are an emerging class of novel therapeutics that are actively being
98 developed in ophthalmology and oncology^{33,34}. They are structurally fully differentiated from antibodies

99 and consist of a single chain of linked DARPin binding domains. In the case of ensovibep, the molecule
100 comprises two human serum albumin binding DARPin domains for systemic half-life extension³⁵ (H1
101 and H2) and three spike protein RBD-binding DARPin domains at the C-terminus (R1, R2 and R3). The
102 relatively small size of ensovibep (85 kDa), in conjunction with high thermal stability³¹, high production
103 yields³¹ and demonstrated high protection against viral escape mutations and variants makes this
104 molecule an attractive alternative to other treatments.

105 Using structural analysis, we provide an explanation for ensovibep-mediated neutralization of the SARS-
106 CoV-2 spike protein. The three distinct DARPin domains can simultaneously target the receptor binding
107 ridge on each RBD of the spike trimer, locking the spike in an open-conformation and occluding the
108 ACE2 binding site. Thanks to the cooperative binding of this novel trispecific design, ensovibep confers
109 very high protection against a panel of relevant spike mutants as well as all frequent SARS-CoV-2
110 variants identified around the globe to date. We show in a viral passaging experiment that the
111 protection provided by ensovibep against development of viral escape mutants is equivalent to that of
112 a well characterized and clinically evaluated monoclonal antibody cocktail^{27,36,37}.

113 Following our *in vitro* characterization, we demonstrate high *in vivo* efficacy in a therapeutic Roborovski
114 dwarf hamster model of COVID-19. Here ensovibep protects against severe disease induced by either
115 wild-type or the Alpha variant SARS-CoV-2. The Roborovski dwarf hamster is highly susceptible to SARS-
116 CoV-2 infection and develops strong lung pathology, with most animals reaching a defined humane
117 endpoint within two to five days after infection³⁸. In the presented study, ensovibep protects the
118 animals to an extent equivalent to a standard-of-care mAb cocktail. For both therapeutic agents, a
119 significant reduction of fulminant disease, as well as significantly reduced viral loads and attenuated
120 lung pathology was observed.

121 In brief, the trispecific design of ensovibep provides great protection against all currently known SARS-
122 CoV-2 variants with the potential to protect against emerging variants in the future. Our findings
123 strongly support the progressing clinical development of ensovibep as a potential therapeutic for
124 COVID-19.

125 Results

126 Structural basis for ensovibep-mediated neutralization of the SARS-CoV-2 spike

127 Ensovibep comprises of five covalently linked DARPin domains. Three of them (R1, R2 and R3) bind the
128 RBD of SARS-CoV-2 with picomolar affinity (Supplementary Figure 1) and two of them (H1-H2) bind to
129 human serum albumin (HSA), extending the systemic half-life (Figure 1A). To understand how
130 ensovibep binds to the SARS-CoV-2 spike (S), we selected one of the three RBD-targeting DARPin
131 domains of ensovibep for cryo-EM analysis in complex with the trimeric S-ectodomain. The RBD-binding
132 domains are from the same sequence family and are thus expected to target a common epitope (Figure
133 1B). Upon incubation of the trimeric spike protein with the monovalent DARPin R2 for 15 seconds prior
134 to vitrification, 3D classification revealed that 65% of the S-ectodomains were in the closed
135 conformation, 20% had two RBDs in the open conformation and 15% had all three RBDs in the open
136 conformation (Supplementary Figure 2A, B). For the open RBD classes, additional density, consistent
137 with the size of the monovalent DARPin molecule, was present on the RBD receptor binding ridge (RBR).
138 When the incubation time was increased to 60 seconds, 66% of S-ectodomains had three monovalent
139 DARPin molecule-bound RBDs in the open conformation (Supplementary Figure 2C). Interestingly, 18%
140 of the S-ectodomains had two DARPin-bound RBDs in the open conformation and one trapped in a
141 partially closed conformation (Supplementary Figure 2C and 3A-B). These results demonstrate that
142 monovalent DARPin domain binding prevents closure of the RBD through a previously described
143 ratcheting mechanism³⁹. 3D refinement of the fully open class, from the 60 second incubated sample,
144 produced a 4.2 Å global resolution map (Figure 1C and Supplementary Figure 2D-F). Following focused
145 refinement of the RBD region, the quality of the map was sufficient to unambiguously assign the pose
146 of the monovalent DARPin domain, which binds perpendicular to the RBD receptor binding motif (RBM),
147 with its N-terminus orientated toward the spike three-fold symmetry axis (Figure 1C). The concave
148 DARPin binding surface covers the RBD and would prevent ACE2 binding through steric hindrance
149 (Figure 1D). Guided by the cryo-EM data, molecular docking experiments were performed between the
150 RBD of SARS-CoV-2 and DARPin R2.

151 The top scoring model indicated that the interface area is $\sim 700 \text{ \AA}^2$ and that key epitope residues are
152 F456, Y473, F486, N487 and Y489, which form an interface of hydrophobic interactions and hydrogen-
153 bonds with the DARPin domain (Figure 1E-F). Because the three DARPin domains share a similar
154 paratope composition and architecture, we were able to conceptually model the entire ensovibep
155 molecule bound to the fully open S-ectodomain (Figure 1G). This demonstrated that the linkers would
156 permit simultaneous binding of all three DARPin modules, allowing very high avidity of ensovibep
157 (Supplementary Figure 1), and that the half-life extension modules have sufficient space to bind HSA

158 (not shown). Taken together, these data suggest that ensovibep inhibits SARS-CoV-2 by blocking ACE2
159 binding and promoting the premature conversion of spike to the post-fusion state. This mechanism of
160 inhibition through receptor functional mimicry was observed for a number of SARS-CoV-2 neutralizing
161 antibodies^{39,40}.

162 **Ensovibep is highly potent against globally identified SARS-CoV-2 variants as well as the most frequent** 163 **spike protein point mutations**

164 In order to assess the neutralizing potencies of ensovibep against the initial SARS-CoV-2 (Wuhan) and
165 emerging variants, we used vesicular stomatitis virus (VSV)-based as well as lentivirus-based
166 pseudoviruses carrying the SARS-CoV-2 wild-type or mutant spike protein at their surface. In addition,
167 we tested the authentic SARS-CoV-2 variants for the Wuhan reference and for lineages B.1.1.7, B.1.351
168 and P.1. Ensovibep is able to neutralize the reference wild type strain with an IC₅₀ of ~1 ng/mL, when
169 either the authentic SARS-CoV-2 or the pseudovirus is used (Figure 2A). Remarkably, the high
170 neutralization efficacy is retained in all the frequent variants circulating to date, which display a diverse
171 set of mutations over the entire length of the spike protein (Figure 2A and 2B; Supplementary Table 2;
172 Supplementary Figure 4). In particular, ensovibep can neutralize the variants of concern (VOC) and
173 variants of interest (VOI) of the lineage B.1.1.7/Alpha (69-70 del, del145, E484K, N501Y, A570D, D614G,
174 P681H, T716I, S982A, D1118H and with the addition of E484K or S494P), lineage B.1.351/Beta (L18F,
175 D80A, D215G, Del242-244, R246I, K417N, E484K, N501Y, D614G, A701V), lineage P.1/Gamma (L18F,
176 T20N, P26S, D138Y, R190S, K417T, E484K, N501Y, D614G, H655Y, T1027I, V1176F), B.1.617.2/Delta
177 (T19R, G142D, del156-157, R158G, L452R, T478K, D614G, P681R, D950N), AY.2/Delta Plus (T19R,
178 G142D, del156-157, R158G, K417N, L452R, T478K, D614G, P681R, D950N), AY.4.2/Delta Plus (T19R,
179 T95I, G142D, Y145H, E156G, F157-, R158-, A222V, L452R, T478K, D614G, P681R, D950N), Lambda
180 (C.37; G75V, T76I, del246-252, D253N, L452Q, F490S, D614G, T859N), Mu (B.1.621; T95I, Y144S,
181 Y145N, R346K, E484K, N501Y, D614G, P681H, D950N), Omicron (B.1.1.529, BA.1; A67V, Δ69-70, T95I,
182 G142D, Δ143-145, Δ211, L212I, ins214EPE, G339D, S371L, S373P, S375F, K417N, N440K, G446S, S477N,
183 T478K, E484A, Q493K/R, G496S, Q498R, N501Y, Y505H, T547K, D614G, H655Y, N679K, P681H, N764K,
184 D796Y, N856K, Q954H, N969K, L981F) and Omicron (B.1.1.529, BA.2; T19I, L24-, P25-, P26-, A27S,
185 G142D, V213G, G339D, S371F, S373P, S375F, T376A, D405N, R408S, K417N, N440K, S477N, T478K,
186 E484A, Q493R, Q498R, N501Y, Y505H, D614G, H655Y, N679K, P681H, N764K, D796Y, Q954H, N969K).
187 The neutralization potencies of ensovibep remain within 10-fold difference from the reference virus
188 (Wuhan or D614G variant) with IC₅₀ values in the low single-digit ng/mL range, even against those
189 variants that have been shown to be, to a large extent, refractory to vaccine- or infection-related
190 antibody neutralization, such as Beta, Gamma, Delta, Delta Plus, and the newly evolved Omicron
191 variants BA.1 and BA.2.^{25,41-43} When testing the neutralizing potency in a VSV-based pseudotype assay,

192 containing more than 30 substitutions of the Omicron spike protein, ensovibep maintained
193 neutralization at low single digit ng/mL IC₅₀ values without loss in potency, when compared to the wild
194 type. In contrast, many of the tested clinically relevant monoclonal antibodies and antibody cocktails
195 demonstrated a major loss in neutralization (Figure 2D).

196 Using the VSV- and lentivirus-based pseudovirus neutralization assays, we also evaluated the influence
197 of single mutations on the neutralization potency of ensovibep, of the monovalent DARPin molecules
198 and of the mAbs REGN10933 and REGN10987, as a reference within the same experiment. The panel
199 included mutations present on variants of interest/concern, appearing frequently, or located within the
200 binding epitope of ensovibep. Most notably, ensovibep protected well against all point mutations
201 tested, in contrast to the single monoclonal antibodies, with the only exception of substitution F486V,
202 which affects all three monovalent DARPin RBD binders incorporated in ensovibep (Figure 2C). A major
203 impact of this mutation is not surprising, as our structural analysis and modelling identifies F486 as a
204 core interacting residue for the three related but distinct RBD binders³¹ (Figure 1B,F). Consequently,
205 the mutation F486V destabilizes the binding of the entire tri-specific ensovibep molecule to the spike
206 protein. However, F486 is also a critical residue for the interaction between the RBD of SARS-CoV-2 and
207 human ACE2 and its mutation leads to a ~8.5-fold reduction of the binding affinity as well as a ~17-fold
208 reduction of the ability of ACE2 to reduce the infection of a VSV-based pseudovirus carrying the F486L
209 mutation (Supplementary Figure 6). The functional importance of F486 is reflected by a low frequency
210 of naturally occurring substitutions at this site (Figure 2C; Supplementary Table 3; Supplementary
211 Figure 4) where the selective pressure on the virus favors a phenylalanine, thus maintaining the key
212 anchoring element for ensovibep binding. A reduction of the potency of ensovibep from one-digit to
213 double-digit ng/mL IC₅₀ was also observed for mutation N234Q. This residue is located outside of the
214 RBD binding region of ensovibep. This minor effect of substitution N234Q could be related to the loss
215 of the conserved glycosylation site at this position, favoring the kinetics of the down conformation of
216 the RBD domain and thus reducing binding of ensovibep as well as ACE2 to the RBD, which only bind
217 the RBD up confirmation.⁴⁴

218 It is interesting to note that ensovibep retains potency against spike proteins carrying mutations at
219 locations where the single DARPin domains partially lose activity, such as E484K and Q493K/R. We
220 hypothesize that the cooperative binding in combination with the complementarity of the three
221 independent RBD-binding DARPin modules provides resistance to mutation escape. Taken together,
222 our analysis demonstrates that the trispecific design of ensovibep enables very high potencies against
223 spike proteins carrying the most frequently observed mutations as well as mutations known to impact
224 the binding of neutralizing antibodies.

225 ***Passaging of SARS-CoV-2 under therapeutic pressure of DARPin antivirals and monoclonal antibodies***

226 Previous studies have shown that SARS-CoV-2 escape mutants may arise under selective pressure of a
227 therapy^{29,45}. Using a viral passaging model, we compared the risk of mutational escape from therapeutic
228 pressure of ensovibep compared to that of its monovalent R2 module, the mAbs REGN10933 and
229 REGN10987, singly and as a 1:1 mixture, as well as the mAb S309.

230 In order to generate a stringent therapeutic pressure, a relatively high viral load of 1.5×10^6 pfu of an
231 authentic French SARS-CoV-2 WT isolate (with the following differences to the Wuhan wild-type spike
232 protein: V367F; E990A) was serially passaged in the presence of increasing concentrations of DARPin
233 molecules and antibodies (Figure 3A, 3B). Resistant escape variants were further selected by passaging
234 the supernatant of cultures showing significant virus-induced cytopathic effect (CPE) under the
235 selection pressure of the highest therapeutic concentration onto fresh cells while maintaining the
236 selective pressure of increasing concentrations of therapeutic antivirals (Supplementary Figure 5). After
237 the first incubation cycle of four days (passage 1), ensovibep, DARPin R2, REGN10933 and the antibody
238 mixture conferred protection at the same concentration of 0.4 $\mu\text{g}/\text{mL}$. S309 was less efficient, requiring
239 a higher concentration (10 $\mu\text{g}/\text{mL}$) for protection and REGN10987 was not protective up to the highest
240 tested concentration of 50 $\mu\text{g}/\text{mL}$. Under continuous selective pressure through passage 2 to 4, DARPin
241 R2 and the individual mAbs S309 and REGN10933 lost the capacity to protect cells, which manifested
242 in complete CPE up to 50 $\mu\text{g}/\text{mL}$. In contrast, ensovibep and the cocktail of two mAbs remained effective
243 and protected cells from CPE throughout the four passages (Figure 3A).

244 To identify putative escape mutations in the spike protein upon therapeutic pressure of the DARPins,
245 RNA was extracted and deep-sequenced from the supernatant of wells with the greatest selective
246 pressure showing a significant cytopathic effect in each passage (Figure 3B). Mutations were found near
247 the spike protein cleavage site (H655Y, N679_R685del, R682W, R682Q), which are likely related to
248 adaptations to the experimental cell system and thus would not account for escape mutations due to
249 the therapeutic pressure of the DARPin^{36,37}, as well as a potential escape mutation, F486L, which was
250 found for the monovalent DARPin R2 but not for ensovibep, up to passaging round four. Still, supporting
251 this finding, mutations in F486 were shown to influence also the potency of ensovibep, when analyzed
252 separately.

253 ***In vivo antiviral efficacy of ensovibep in a COVID-19 SARS-CoV-2 Roborovski dwarf hamster model***

254 To test the *in vivo* efficacy of ensovibep in treating SARS-CoV-2 infection, we employed the Roborovski
255 dwarf hamster, a species susceptible to severe COVID-19 like illness⁴⁶. Unlike the more commonly used
256 Syrian golden hamster⁴⁷, this species is prone to develop a lethal course of disease, notably without the

257 extrapulmonary disease manifestations observed in highly susceptible transgenic mice⁴⁸. We used this
258 particular animal model to judge the *in vivo* efficacy of ensovibep and to compare it to the REGN10933
259 & REGN10987 antibody mixture. Moreover, evaluation of the virological and histopathological outcome
260 of infection enabled comparison across a variety of important parameters of infection.

261 We first aimed to determine *in vivo* protection conferred by ensovibep against a SARS-CoV-2 wild type
262 reference strain (BetaCoV/Germany/BavPat1/2020). In an initial series of experiments, we determined
263 both dose and time dependency of treatment efficacy based on clinical and virological parameters. In
264 absence of venous access in dwarf hamsters, we choose intraperitoneal (i.p.) treatment for delivery of
265 ensovibep. It is important to note, that the course of disease in Roborovski dwarf hamsters is rapid,
266 with first animals developing severe disease and reaching termination criteria within 48 hours of
267 infection. For this reason, we considered 24 hours post-infection (p.i.) the latest possible intervention
268 time point. Both dose and time of ensovibep administration (relative to time of infection) were found
269 to positively affect the outcome of infection. Specifically, the use of ensovibep resulted in markedly
270 reduced virus loads in the respiratory tract of treated animals (Supplementary Figure 7).

271 From these initial results, we determined 10 mg/kg to be the optimal dose for ensovibep treatment
272 and in further studies compared this dose with the same dose of the REGN10933 & REGN10987 cocktail
273 using the SARS-CoV-2 alpha (B.1.1.7) variant of a more recent isolate
274 (BetaCoV/Germany/ChVir21652/2020) for infection of animals. We chose two treatment time points,
275 the first at the time of infection to mimic clinical post exposure prophylaxis and the second at 24 h p.i.
276 to mimic treatment at the onset of clinical symptoms (Figure 4A). For the post exposure prophylaxis
277 dosed directly after infection (0 h p.i.), we confirmed full protection for both treatments with notable
278 reduction of viral loads, particularly in the lungs of treated animals compared to placebo treated
279 controls at all time points (Figure 5A). There were no obvious differences between the two agents,
280 however, based on virological parameters, a slight trend towards lower viral load in the antibody
281 cocktail group was observed at 5 days p.i. (Figure 5A).

282 In contrast to the similarities in the post exposure prophylaxis setting we observed differences between
283 the groups treated 24 hours p.i. (Figure 4B, C). In this scenario, animals treated with ensovibep
284 presented with improved condition at 2 days p.i. with 0/12 of the animals reaching a defined humane
285 endpoint, while 5/12 animals were euthanized in the mAb cocktail group and 5/12 in the placebo group
286 (Figure 5B) due to reached humane endpoints. Nevertheless, 3/10 hamsters in the ensovipeb group
287 and an additional three hamsters in the placebo group reached defined endpoints at day 3 p.i., while
288 no further animals in the mAb cocktail group developed severe illness after day 3 p.i. (Figure 5B).
289 Following 24 h p.i. treatment, no significant differences in average body weights or temperatures were

290 observed in any of the treatment groups (Figure 5C, Supplementary Figure 8). This is likely a result of
291 the early termination of severely sick animals, while the healthier animals remained in the study.
292 However, examination of these parameters on day 2 p.i. revealed significant trends towards reduced
293 body weight loss in both treatment groups compared to the placebo and a similar trend towards higher
294 body temperatures in the ensovibep group compared to the other groups (Figure 5C). As body
295 temperature decrease is a very sensitive parameter of disease in this species⁴⁶, this in particular is
296 reflective of the improved condition in the ensovibep treated group at 24h p.i., when compared to the
297 antibody cocktail treated or the placebo treated animals. Virological readouts were not significantly
298 different between groups treated with ensovibep and the mAb cocktail at 24 hours post-infection. Both
299 treatments resulted in drastic reductions of viral load compared to the placebo group (Figure 5A, B).
300 This result was more pronounced at the level of replicating virus, indicating efficient neutralization of
301 cell-free virus in both treatment groups (Figure 5B). These trends were likewise reflected by the results
302 of histopathological examinations of animals treated at 24 h p.i.. While the histological outcome of
303 infection was similar between both treatment groups (Figure 6), semi-quantitative assessment of SARS-
304 CoV-2 induced lesions revealed consistently higher scores for the mAb treated group compared to
305 ensovibep. Interestingly, scores for inflammation in the mAb treated group were on average exceeding
306 the scores obtained for the placebo group. These findings need to be interpreted knowing that 5/6
307 animals in the mAb treated group which had been scheduled for termination and analysis at day 3 had
308 to be taken out of the study already on day 2 due to rapid onset of fulminant disease, which is reflected
309 by these readouts.

310 To account for possible differences in exposure, we performed pharmacokinetic analysis for both
311 treatments. These assessments identified that overall, comparable exposures were achieved in non-
312 infected hamster following i.p. administration. It was noted that, ensovibep achieved a higher maximal
313 serum concentration (C_{max}) and a shorter systemic half-life compared to the mAb cocktail
314 (Supplementary Figure 9).

315 Considering the small size of the Roborovski dwarf hamster, failure of i.p. injection due to an accidental
316 injection into body compartments other than the peritoneum may occur. We thus screened for animals
317 which lacked a proper drug exposure in terminal serum samples and removed data of these animals
318 from all other analyses (Supplementary Table 4).

319 Whole genome sequencing using virus RNA recovered from lungs and upper respiratory tract was
320 performed to investigate whether SARS-CoV-2 escape mutants were selected under ensovibep
321 treatment. Viral RNA from individual animals with higher viral load compared to other animals of the

322 same treatment group was analyzed and no escape mutations affecting the ensovibep epitope located
323 in the RBD were discovered (Supplementary Table 5).

324 Discussion

325 Multiple strategies are urgently needed to combat the COVID-19 pandemic. Next to preventive
326 vaccination approaches and small molecules, mAbs are showing therapeutic promise, based on highly
327 potent virus inhibition and encouraging animal and clinical efficacy. However, manufacturing capacities
328 are limiting a global supply and novel emerging variants of SARS-CoV-2 are an ever-present threat, as
329 they may escape the antibodies generated during immunization or in response to therapeutics. A
330 number of alternative molecules are being developed to complement and partially overcome these
331 limitations.

332 In the present study, we provide the structural and functional analysis of ensovibep, a trispecific DARPin
333 designed as a potential alternative to antibodies and other therapeutics^{32,49-53}. The structural analysis
334 provides insights into the mode of action, which enables low picomolar neutralizing activity against the
335 currently most frequent SARS-CoV-2 mutations as well as recently identified variants. We measured the
336 effect of ensovibep on a panel of single spike protein mutations which have been shown to be of
337 concern because they may be associated with increased transmissibility, disease severity, or affect
338 neutralization of some monoclonal- or polyclonal antibodies^{27,54,55}. Among all mutations tested, only
339 F486 substitutions caused a strong decrease in ensovibep potency when compared to the wild-type or
340 reference virus. The effect of this mutation was also noted in the viral passaging study: sequencing of
341 mutations allowing escape from inhibition by the monovalent RBD binder (R2, incorporated in
342 ensovibep) identified F486L (Figure 3B). These findings are in line with our structural analysis (Figure
343 1F) showing that F486 is one of the key binding residues for the interaction of ensovibep with the RBD.
344 Most importantly, F486 is a critical residue for the virus itself, allowing an efficient binding to the ACE2
345 receptor and thus cell infection. Therefore, mutations of the phenylalanine at position 486 will decrease
346 the affinity between the RBD and human ACE2 receptor and lower the infectivity of the virus^{17,56-58}
347 (Supplementary Figure 6). We thus expect that position F486 in the SARS-CoV-2 spike protein will
348 remain conserved to maintain efficient binding to the human ACE2 receptor or that the virus might lose
349 fitness if mutated at this position. So far, based on the global SARS-CoV-2 database sequences published
350 in the GISAID database (<https://www.gisaid.org/hcov19-variants/>; visited November 2021), mutations
351 in position F486 occur at very low frequencies.

352 A small reduction of neutralization potency observed for ensovibep and its single DARPin moieties for
353 viruses bearing the N234Q mutation outside of the RBD might be explained by the impact of the
354 mutation on the RBD conformational dynamics. An *in-silico* simulation study showed that this
355 conserved glycosylation site, together with N165, might be involved in the stabilization of the RBD up-
356 conformation. Since the epitope of ensovibep is exposed only in the up-conformation, a mutation in

357 one of these glycosylation sites might affect its binding equilibrium, as indicated in our neutralization
358 assays. The N234Q mutation might thus impact all protein binding scaffolds that are binding exclusively
359 to the up-conformation of the RBD. By the same token, reduced affinity of the spike protein for the
360 human ACE2 receptor was demonstrated elsewhere in *in vitro* assays⁴⁴. Accordingly, mutations of the
361 N165 and N234 amino acids have been observed only at low frequencies (<0.02%).

362 Some mutations that are not predicted to be key interaction residues for the three distinct RBD binders
363 of ensovibep (e.g., E484K or Q493K), led to a reduction in potency for one or several of the RBD-binding
364 monovalent DARPins, while the trispecific ensovibep molecule maintained full neutralization capacity.
365 This demonstrates that the trispecific DARPin design of ensovibep, with cooperative binding of three
366 distinct paratopes (Supplementary Figure 1), permits high neutralizing potency, even in the case when
367 an individual monovalent DARPin domain exhibits decreased affinity (Figure 2A). This cooperative
368 binding of multiple paratopes is a hallmark of the trispecific nature of ensovibep and differentiates the
369 molecule from mAb candidates to allow full neutralization of highly mutated SARS-CoV-2 variants such
370 as Omicron BA.1 and BA.2, that are substantially different from the original virus that the mAb was
371 selected against⁵⁹.

372 The high level of protection against viral escape mutations by ensovibep demonstrated in the virus
373 challenge studies was also clearly apparent in a viral passaging experiment. The single mAbs and the
374 monovalent DARPin binder were rapidly overcome by escape mutants whereas ensovibep maintained
375 potency to an extent comparable to a clinically validated mAb cocktails.

376 Translatability of the observed *in vitro* activity of ensovibep against SARS-CoV-2 was evaluated in a
377 COVID-19 model using the highly susceptible Roborovski dwarf hamsters. Using this *in vivo* model, we
378 confirmed the therapeutic benefit of ensovibep, which displayed comparable outcomes to a clinically
379 validated antibody cocktail (REGN10933 & REGN10987). In our comparison, we found evidence for a
380 better performance of ensovibep in a late intervention scenario with prolonged survival of animals and
381 reduced inflammation of the lungs. Potential reasons for this difference include differences in
382 pharmacokinetics where ensovibep demonstrated a higher maximal concentration compared to the
383 antibody cocktail (Supplementary Figure 9). Another possible explanation could be that ensovibep lacks
384 an Fc-fragment when compared to antibodies stimulating pro-inflammatory immune responses mostly
385 via their Fc-fragment. Regardless of this, we clearly demonstrate that ensovibep has great potential to
386 prevent disease and eliminate the virus in a highly susceptible *in vivo* model under different treatment
387 scenarios. The clinical translatability of these results is currently being investigated in the EMPATHY trial
388 for the treatment of ambulatory COVID-19 patients.

389 In conclusion, ensovibep, has been shown to have highly potent neutralization against the currently
390 most frequent SARS-CoV-2 variants due to its cooperative and complementary binding to a highly
391 conserved epitope region on the spike RBD. *In vitro* and *in vivo* single agent efficacies closely match the
392 performance of one of the best clinically validated mAb cocktails. In addition, the albumin binding
393 domains of the molecule have been demonstrated to confer a plasma half-life compatible with single
394 dose treatment. Translation of these preclinical findings into the clinic is currently under investigation
395 and if successful, the *E. coli* based-manufacturing of the agent will allow rapid and large-scale
396 production for global access to this alternative class of therapeutics as an addition to other treatment
397 approaches for COVID-19.

398 **Data availability**

399 The EM density maps for the SARS-CoV-2 spike ectodomain in complex with monovalent DARPin R2
400 (state 1 and state 2), have been deposited to the Electron Microscopy Data Bank under the accession
401 codes EMD-11953 and EMD-11954, respectively. The monovalent DARPin and multivalent DARPin
402 sequences, and pseudo-atomic models derived from molecular docking experiments, are available
403 here, to allow the use of the data for non-commercial purposes:

404 <https://www.guidetopharmacology.org/GRAC/LigandDisplayForward?tab=structure&ligandId=11470>

405

406 **Acknowledgements**

407 S.R. & J.M. were supported by Swiss Federal Office for Civil Protection (Grants Nr. 353008564/Stm,
408 353008218/Stm, and 353008560/Stm to Olivier Engler and Stefan Kunz).

409 D.L.H. is funded by the European Union's Horizon 2020 research and innovation program under the
410 Marie Skłodowska-Curie grant agreement (No 842333) and holds an EMBO non-stipendiary long-term
411 Fellowship (ALTF 1172-2018). Cryo-EM data processing was carried out on the Dutch national
412 e-infrastructure with the support of the SURF Cooperative.

413 The authors also thank Dr. Gert Zimmer for the gift of the recombinant VSV (Institute of Virology and
414 Immunology (IVI), CH-3147 Mittelhäusern, Switzerland, Department of Infectious Diseases and
415 Pathobiology, Vetsuisse Faculty, University of Bern, CH-3012 Bern, Switzerland).

416 The expression plasmid for the SARS-CoV-2 spike protein was kindly provided by Dr. Giulia Torriani and
417 Dr. Isabella Eckerle (Department of Medicine, University of Geneva, Switzerland).

418 We would like to thank Dr. Sylvie van der Werf for the supply of 2019-nCoV/IDF0372/2020 (National
419 Reference Centre for Respiratory Viruses hosted by Institut Pasteur (Paris, France)). Strain 2019-
420 nCoV/IDF0372/2020 was generously provided by Dr. X. Lescure and Pr. Y. Yazdanpanah from the Bichat
421 Hospital. Additionally, we would like to thank William Lee, former board member of Molecular Partners
422 - and the Virology group at Gilead Sciences for their helpful input.

423 We would like to thank the Centre for AIDS Reagents (National Institute for Biological Standards and
424 Control, Herts, UK) for providing VeroE6/TMPRSS2 cells.

425 Lentivirus pseudotype investigations were performed independently by investigators at the US Food
426 and Drug Administration, Center for Biologics Evaluation and Research as part of Therapeutics Research
427 Team for the US government COVID-19 response efforts. The work was supported by US government
428 research funds.

429

430 **Funding**

431 The work was funded by Molecular Partners AG, Switzerland, or as stated in the Acknowledgements.

432

433

434

435

Main Figures for

436

437

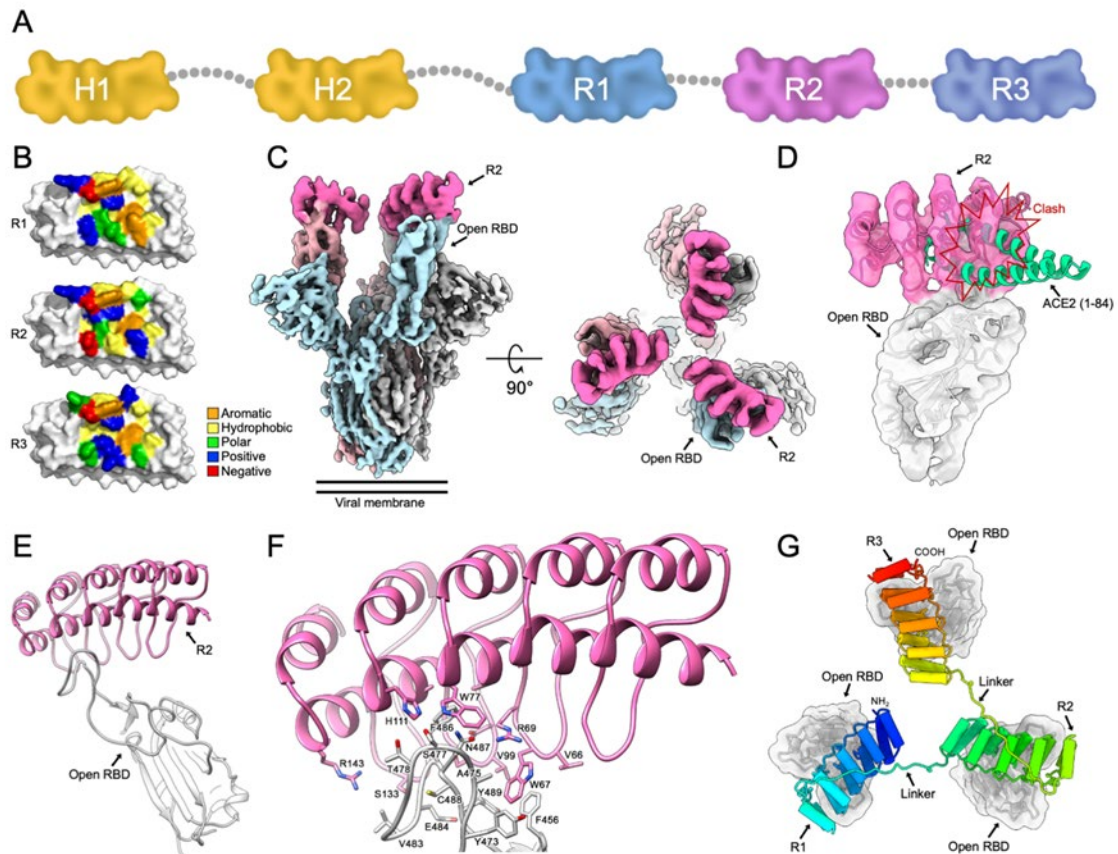
**Ensovibep, a novel trispesific DARPIn candidate that
protects against SARS-CoV-2 variants**

438

439

440

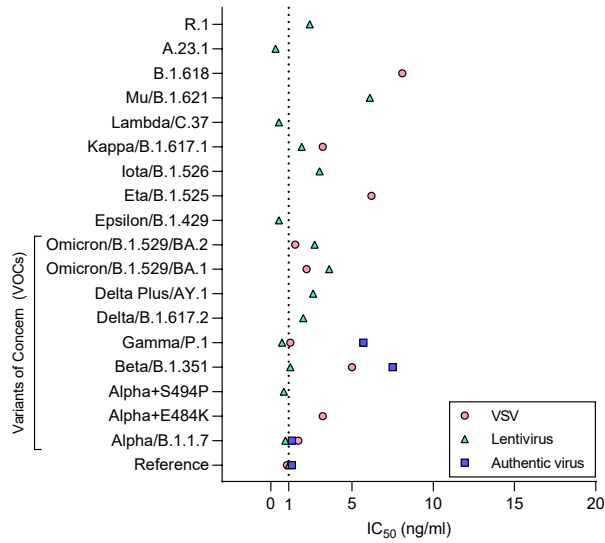
Rothenberger et al. 2021



441

442 **Figure 1: Structural modelling of ensovibep.** A) Schematic overview of the ensovibep
443 construct. Protein linkers are depicted as gray dashed lines and the half-life extending human
444 serum albumin binding monovalent DARPins (H1 and H2) are colored yellow. B) Surface
445 representations of the three monovalent DARPin molecules binding to the RBD, with the
446 amino acid residues in the paratope colored according to their biophysical characteristics as
447 indicated. C) Cryo-EM density for the SARS-CoV-2 spike ectodomain in complex with the
448 RBD-targeting monovalent DARPin R2, shown as two orthogonal views. The DARPin density
449 is colored magenta and the three spike protomers are colored light blue, grey and pale pink.
450 D) Zoomed in view of an RBD-bound to DARPin R2 with the cryo-EM density shown semi-
451 transparent. The atomic coordinates for the fitted open RBD (PDB ID: 6XCN) and the DARPin
452 model are overlaid. The atomic coordinates for residues 1-84 of the RBD-bound ACE2 (PDB
453 ID: 6M0J), colored green, is superimposed. E) Pseudo-atomic model of the monovalent
454 DARPin R2 in complex with the RBD, colored pink and grey, respectively. F) Zoomed in view
455 of the interface between monovalent DARPin R2 and RBD. G) Proposed model of the three
456 covalently linked RBD-targeting monovalent DARPin molecules of ensovibep bound to the
457 trimeric spike protein RBD domains. The three DARPin domains are shown in a rainbow color
458 scheme from the N terminus (blue) to the C terminus (red).

459 **A**

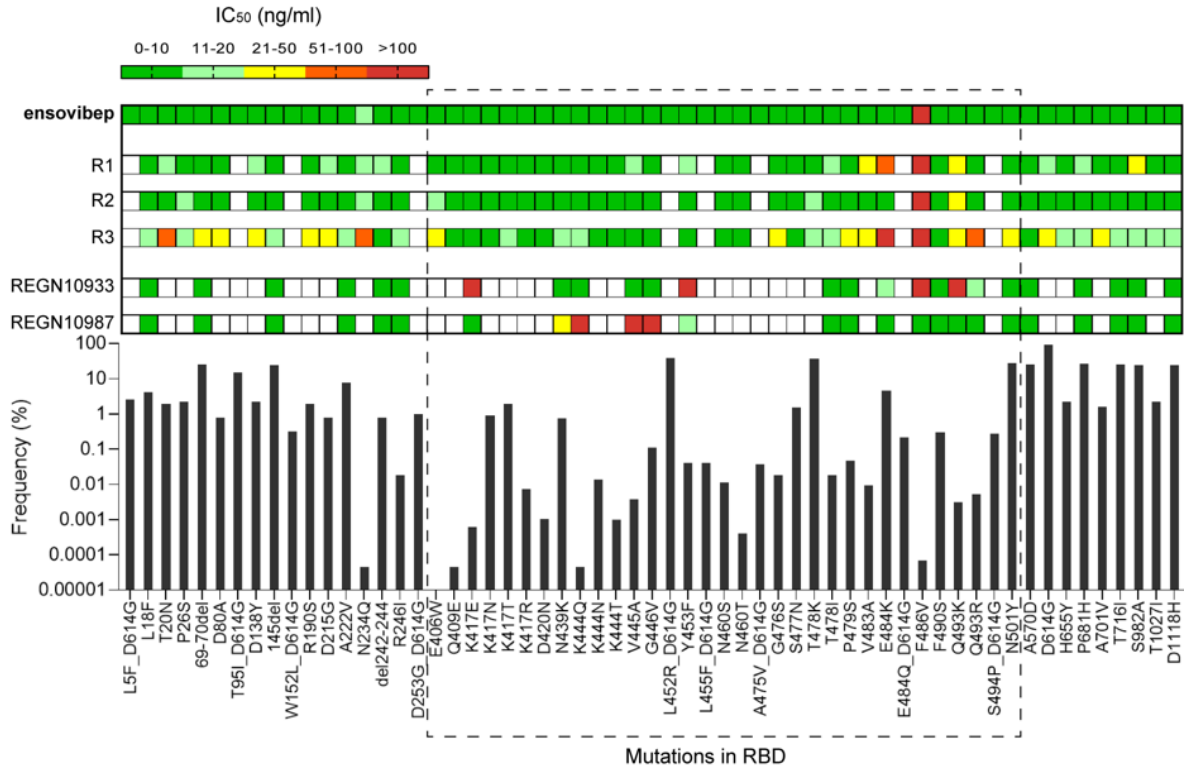


B

Variant	Substitutions / Deletions
R.1	W152L, E484K, D614G, G769V
A.23.1	F157L, V367F, Q613H, D614G, P681R
B.1.618	del145, del146, E484K, D614G
Mu / B.1.621	T95I, Y144S, Y145N, R346K, E484K, N501Y, D614G, P681H, D950N
Lambda / C37	G75V, T76I, del246, del247-252, D253N, L452Q, F490S, D614G, T859N
Kappa / B.1.617.1	T95I, G142D, E154K, L452R, E484Q, D614G, P681R, Q1071H
Iota/B.1.526	L5F, T95I, D253G, E484K, D614G, A701V
Eta/B.1.525	Q52R, del69-70, del145, E484K, D614G, Q677H, F888L
Epsilon/B.1.429	S13I, P26S, W152C, L452R, D614G
Omicron / B.1.1.529 / BA.2	T19I, L24-, P26-, P26-, A27S, G142D, V213G, G339D, S371F, S373P, S375F, T376A, D405N, R408S, K417N, N440K, G446S, S477N, T478K, E484A, Q493R, G496S, Q498R, N501Y, Y505H, T547K, D614G, H655Y, N679K, P681H, N764K, D796Y, Q954H, N969K
Omicron / B.1.1.529 / BA.1	A67V, del69-70, T95I, G142D, del143-145, del211, L212I, ins214EPE, G339D, S371L, S373P, S375F, K417N, N440K, G446S, S477N, T478K, E484A, Q493R, G496S, Q498R, N501Y, Y505H, T547K, D614G, H655Y, N679K, P681H, N764K, D796Y, N856K, Q954H, N969K, L981F
DeltaPlus / AY.1	T19R, T95I, G142D, E156G, del157-158, W258L, K417N, L452R, T478K, D614G, P681R, D950N
Delta / B.1.617.2	T19R, G142D, E156G, del157-158, L452R, T478K, D614G, P681R, D950N
Gamma / P.1	L18F, T20N, P26S, D138Y, R190S, K417T, E484K, N501Y, D614G, H655Y, T1027I, V1176F
Beta / B.1.351	L18F, D80A, D215G, del242-244, R246I, K417N, E484K, N501Y, D614G, A701V
Alpha / B.1.1.7 +S494P	del69-70, del145, S494P, N501Y, A570D, D614G, P681H, T716I, S982A, D1118H
Alpha / B.1.1.7 +E484K	del69-70, del145, E484K, N501Y, A570D, D614G, P681H, T716I, S982A, D1118H
Alpha / B.1.1.7	del69-70, del145, N501Y, A570D, D614G, P681H, T716I, S982A, D1118H
References	VSV: Wuhan wild-type; Lentivirus: D614G; Authentic: V367F, E990A

460

461 **C**



462

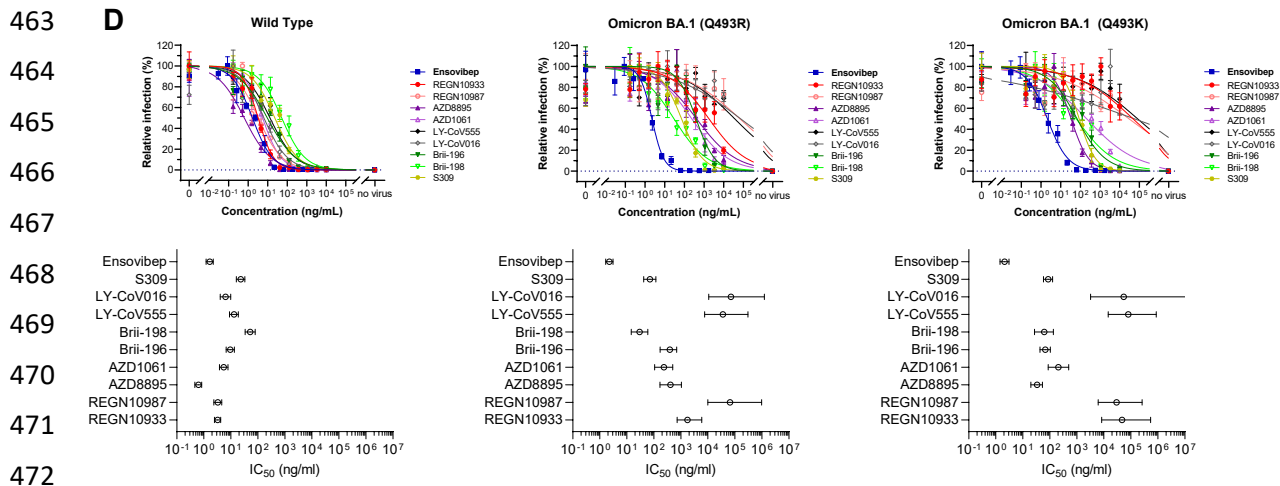


Table 2: Neutralization of ensovibep and a panel of monoclonal antibodies in two VSV-pseudotype assays (including Q493R or Q493K) containing the Omicron variant spike protein with >30 substitutions.

Compound	Wild Type	Omicron (Q493R) ¹		Omicron (Q493K) ²	
	IC ₅₀ (ng/mL)	IC ₅₀ (ng/mL)	fold change to wt	IC ₅₀ (ng/mL)	fold change to wt
ensovibep	1.6	2.2	1.4	2.1	1.3
REGN10933	3.2	>1000	>100	>1000	>100
REGN10987	3.3	>1000	>100	>1000	>100
LY-CoV555	13	>1000	>100	>1000	>100
LY-CoV016	6.4	>1000	>100	>1000	>100
S309	23	72	3.1	87	3.8
AZD8895	0.6	415	>100	34	56
AZD1061	5.5	237	43	207	38
Bii-196	9.5	392	41	68	7.1
Bii-198	52	30	0.6	62	1.2

IC₅₀: green: <10 ng/mL; orange: 10-100 ng/mL; dark orange: 100-1000 ng/mL; red: >1000 ng/mL
 fold change to wt: green: <10-fold; orange: 10-100-fold; red: >100-fold

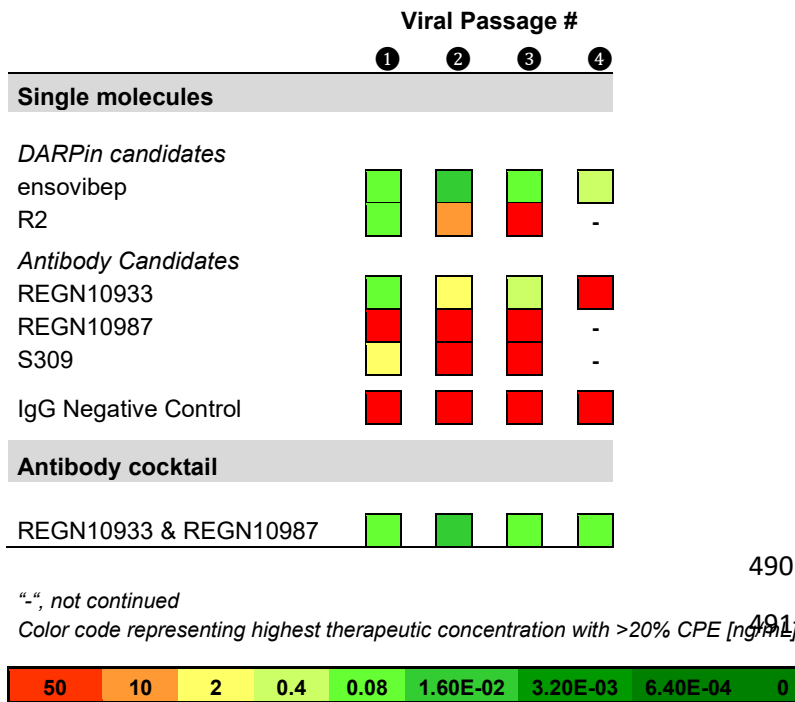
¹ Set of mutations: A67V, Δ69-70, T95I, G142D, Δ143-145, Δ211, L212I, ins214EPE, G339D, S371L, S373P, S375F, K417N, N440K, G446S, S477N, T478K, E484A, Q493R, G496S, Q498R, N501Y, Y505H, T547K, D614G, H655Y, N679K, P681H, N764K, D796Y, N856K, N969K, L981F.

² Set of mutations: A67V, Δ69-70, T95I, G142D, Δ143-145, Δ211, L212I, ins214EPE, G339D, S371L, S373P, S375F, K417N, N440K, G446S, S477N, T478K, E484A, Q493K, G496S, Q498R, N501Y, Y505H, T547K, D614G, H655Y, N679K, P681H, N764K, D796Y, N856K, Q954H, N969K, L981F.

473

474 **Figure 2:** A) Graph reporting IC₅₀ values (ng/mL) for ensovibep measured in neutralization
 475 assays performed with lentivirus-, VSV-based pseudoviruses or authentic viruses for the
 476 variants indicated. Reference variant is the Wuhan strain for VSV-based pseudovirus, a
 477 D614G variant for the lentivirus-based pseudovirus or a patient isolate from the early
 478 pandemic for the authentic virus. B) Schematic representation of the residues modified in the
 479 SARS-CoV-2 spike protein for the different variants tested compared to the Wuhan strain. C)
 480 Graph with global frequencies of point mutations in the spike protein of SARS-CoV-2
 481 according to the GISAID database (as of October 2021) including a heat map table with IC₅₀
 482 values for ensovibep, R1, R2, R3, REGN10933, REGN10987 for all point mutations tested
 483 (VSV/Lentivirus-based pseudovirus assays). Dashed box: mutations in RBD. D) Titration
 484 curves (mean ±SEM) and IC₅₀ values (mean ±CI at 95%) for VSV-pseudotype neutralization
 485 assays with wild-type and two different Omicron BA.1 variant spike proteins containing either
 486 an arginine or a lysine in position Q493. Ensovibep was tested together with a panel of
 487 clinically validated monoclonal antibodies. The table provides the numeric IC₅₀ values as well
 488 as the fold change towards the wild-type values.

489 **A**



493

494 **B**

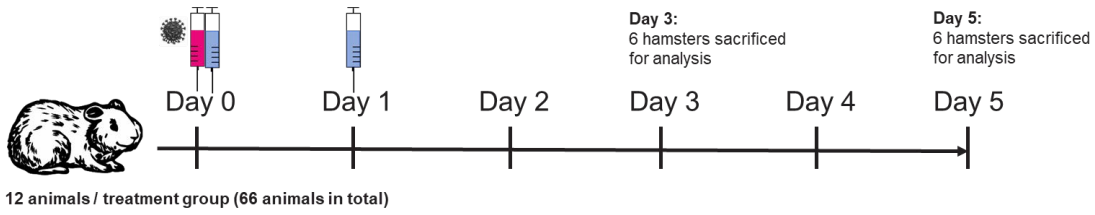


502 **Figure 3: Protection against SARS-CoV-2 escape mutations generated over four viral**
 503 **passages.**

504 A) Tabular representation of the cytopathic effects induced by SARS-CoV-2 cultured in the
 505 presence of increasing concentrations of mono-valent DARPin binder R2, multi-specific
 506 DARPin antiviral ensovibep and the antibody antivirals REGN10933, REGN10987 and S309
 507 or a cocktail of REGN10933 and REGN10987 through passage 1 to 4. Color code represents
 508 the highest concentration showing $\geq 20\%$ CPE, for which the culture supernatants was
 509 passaged to the next round and deep sequenced for the identification of potential escape
 510 mutations. B) Identification of escape mutations in viral passages using deep sequencing.

511 *SARS-CoV-2 virus was serially passaged with the mono-valent DARPin binder R2 and*
512 *ensovibep. To identify putative escape mutations in the spike protein, RNA was extracted and*
513 *sequenced from supernatant of wells with the greatest selective pressure showing a significant*
514 *cytopathic effect. All variants in the spike protein relative to the reference genome*
515 *(NC_045512.2) are shown. Passage 0 of the virus control corresponds to the inoculum used*
516 *for all experiments. The color of the fields is proportional to the fraction of the reads containing*
517 *the respective variant (red= 1.0 white=0.0).*

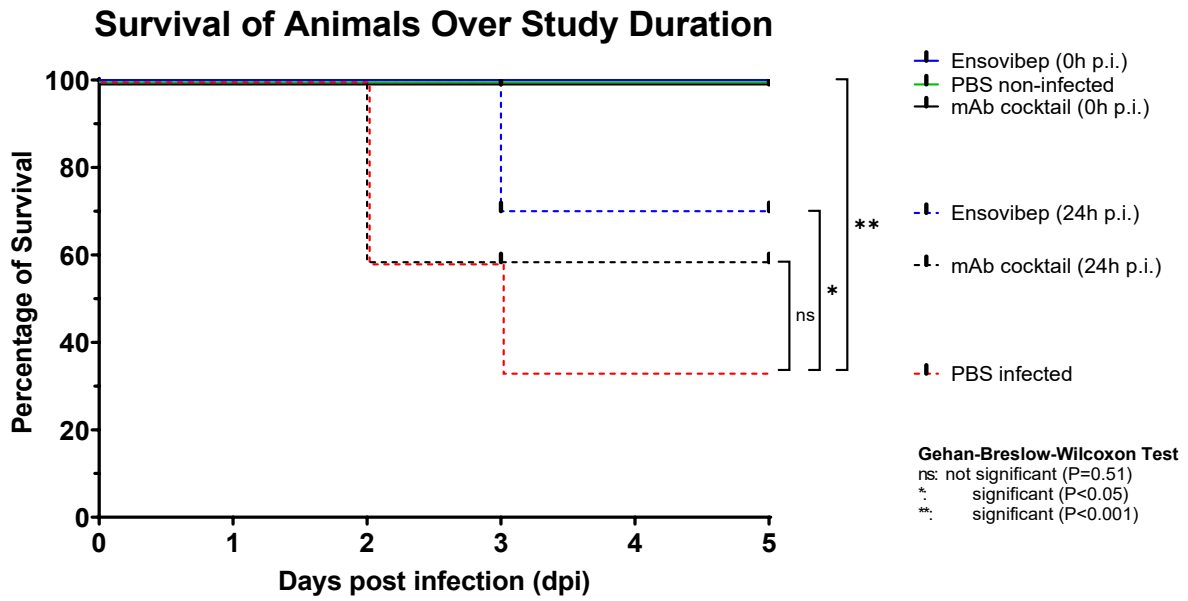
518 **A**



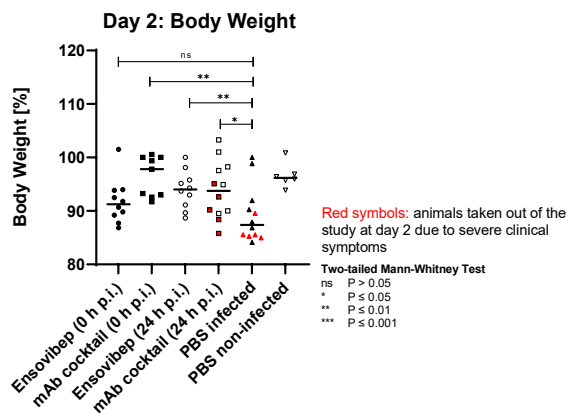
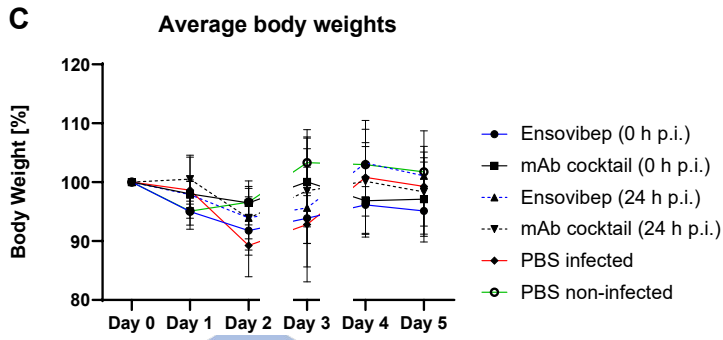
519

520

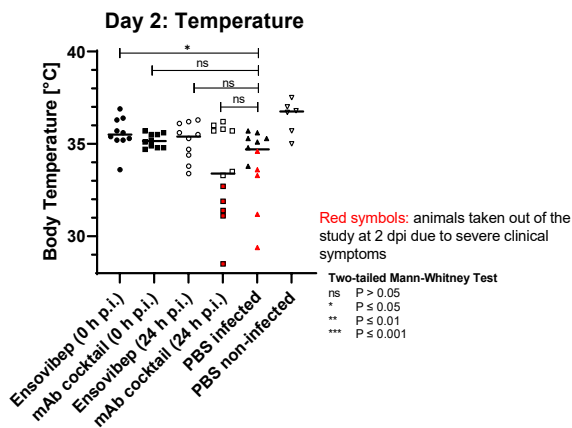
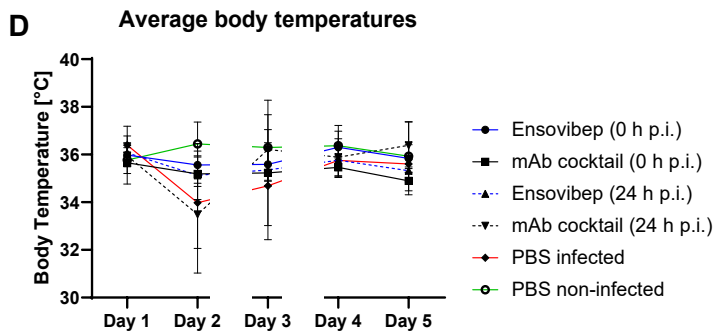
521 **B**



522



523

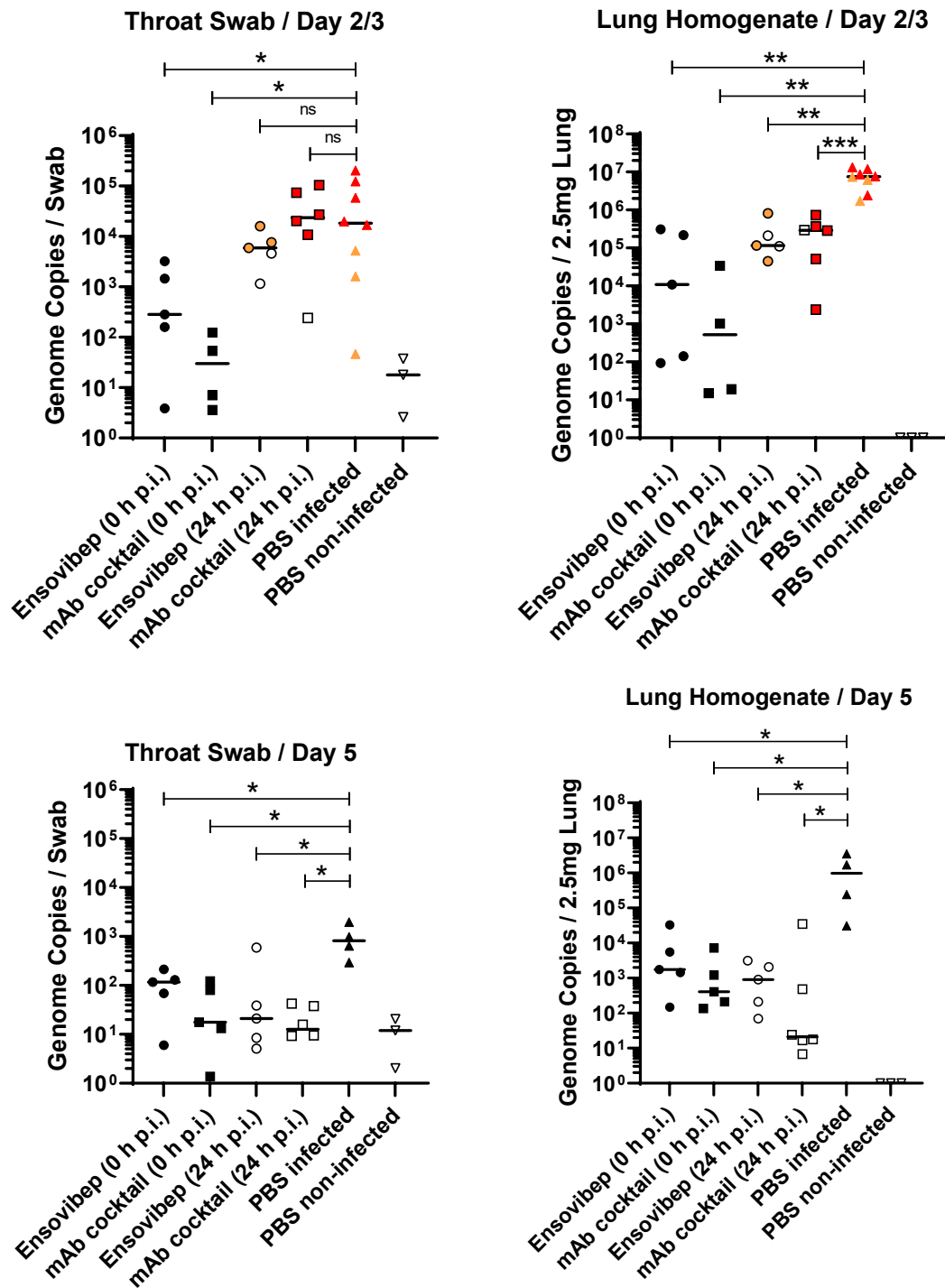


524

525 **Figure 4:** A) Design of the Roborovski dwarf hamster study. Animals were infected on day 0
526 with 10^5 pfu of SARS-CoV-2 alpha (B.1.1.7) variant. Treatment was administered either
527 directly following infection (0 h p.i.) or one day post infection (24 h p.i.). For each treatment
528 group, twelve animals were injected i.p. with either 10 mg/kg of esovibep, 10 mg/kg
529 monoclonal antibody cocktail (5 mg/kg REGN10933 & 5 mg/kg REGN10987), or PBS
530 (placebo). Additionally, a group of six non-infected and non-treated control animals were
531 included as comparators for the infected and treated groups. Daily measurement of body
532 weight and temperatures as well observation of vital symptoms was undertaken. Animals were
533 sacrificed on day 3 or 5 p.i. or immediately once an individual reached a defined humane
534 endpoint. B) Survival of animals for 5 days p.i.. Animals that had to be euthanized according
535 to defined humane endpoints were considered as non-survived. C) Body weight and D) body
536 temperatures throughout the study duration. Data points show mean +/- SD of the following
537 number of animals analyzed per treatment group at (0/1/2/3/4/5) days p.i.: Esovibep 0h:
538 n=10/10/10/10/5/5; mAb cocktail 0h: n=9/9/9/9/5/5; Esovibep 24h: n=10/10/10/10/5/5; mAb
539 cocktail 24h: n=12/12/12/7/6/6; Placebo, infected: n=12/12/12/7/4/4; Placebo, non-infected:
540 n=6/6/6/6/6/6. The rationale for excluding animals is the identification of animals with low drug
541 exposure, likely due to a failure of i.p. injections. These animals were excluded from all
542 analyses. Lines connecting dots are interrupted for any change in animal numbers between
543 consecutive days.

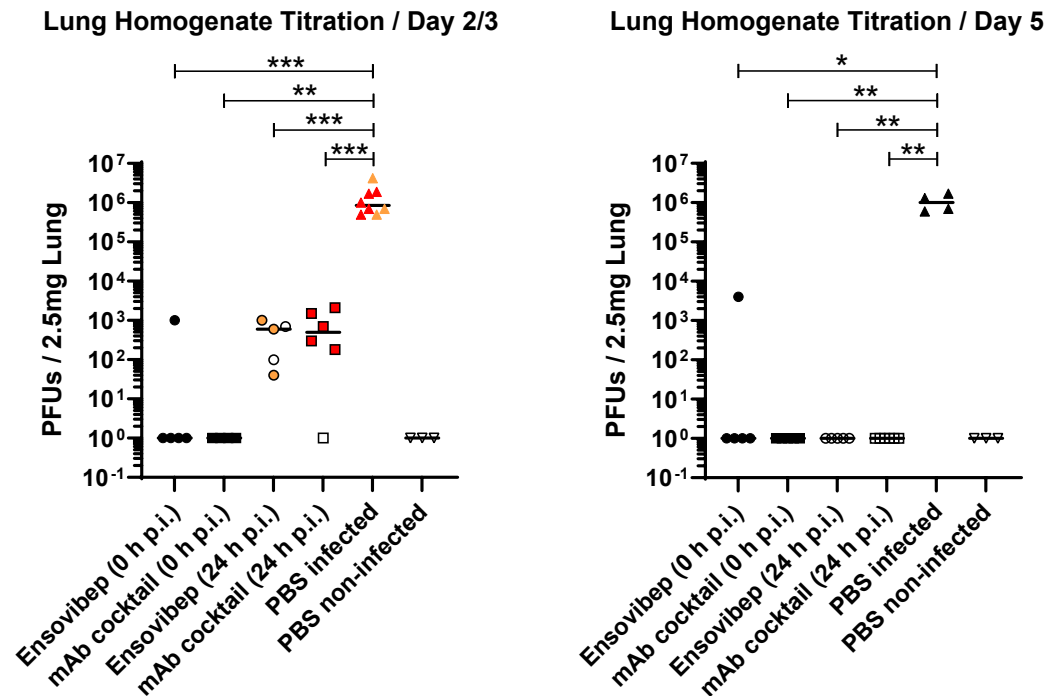
544 Since a considerable number of animals in the mAb cocktail and placebo groups reached
545 defined humane endpoints by day 2 p.i., This day is zoomed-in and values are presented the
546 median and for each individual animal with red symbols marking animals that had to be
547 euthanized at day 2.

548 **A**



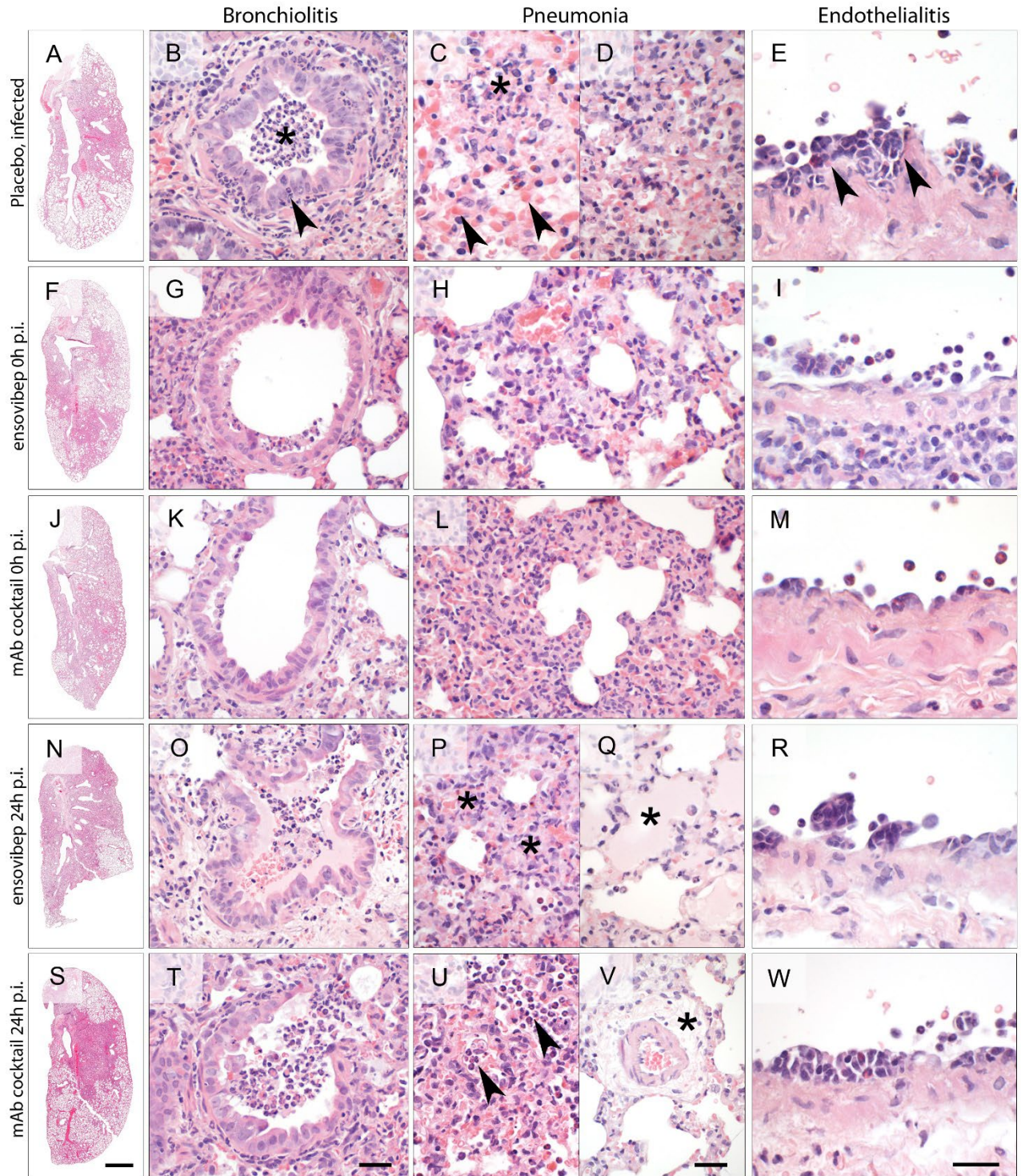
549

550 **B**



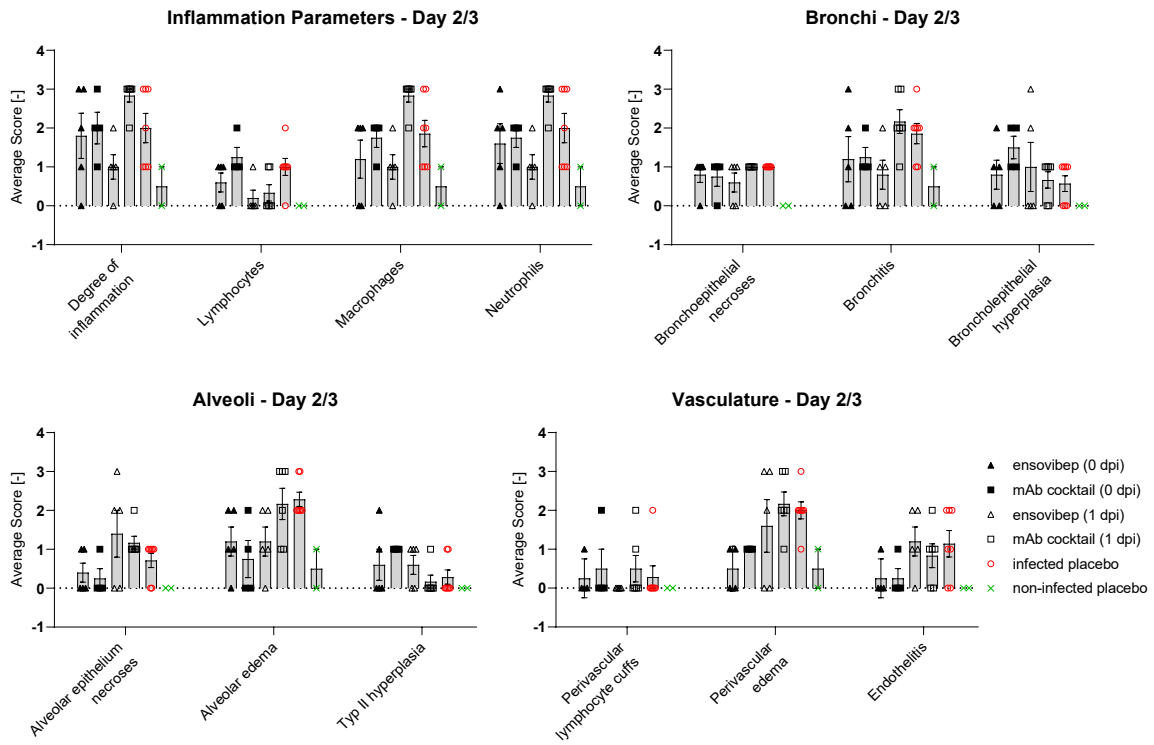
551

552 **Figure 5:** A) qPCR analysis of virus gRNA copy numbers in oropharyngeal swabs and lung
553 homogenates at day 2/3 or day 5 p.i. B) Titration of replication competent virus from lung
554 homogenates as plaque assay on Vero E6 cells at day 2/3 or day 5 post infection. Red
555 symbols: animals taken out of the study at day 2 due to severe clinical symptoms. Orange
556 symbols: animals taken out of the study at day 3 due to severe clinical symptoms. Data is
557 represented by the median and values for individual animals. Statistics: two-tailed Mann-
558 Whitney Test: ns $P > 0.05$; * $P \leq 0.05$; ** $P \leq 0.01$; *** $P \leq 0.001$.



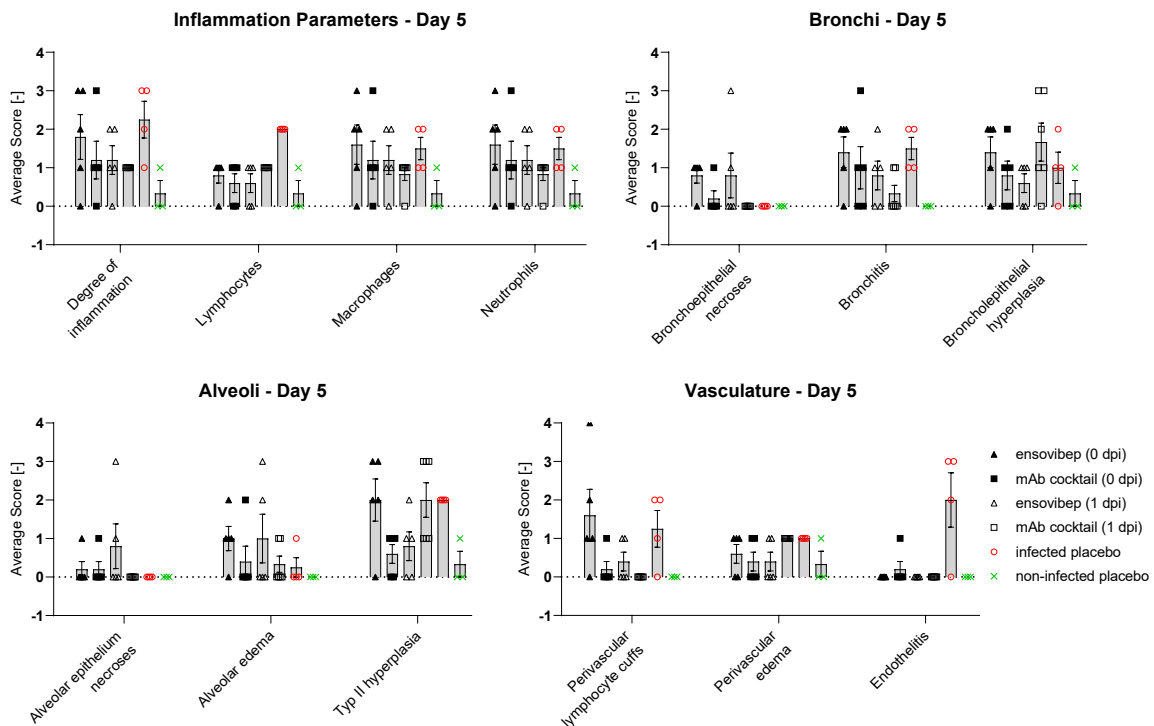
559

560 X



561

562 Y



563

564

565 **Figure 6:** A-W. Lung histopathology of Roborovski dwarf hamsters at 2 or 3 days p.i. with
566 SARS-CoV-2, hematoxylin and eosin stain. (A-E) Lungs of untreated hamsters at 3 days p.i.
567 developed marked inflammation with lesion patterns as described earlier. (A) Whole slide scan
568 revealing consolidation of approximately 60% of the left lung. (B) Untreated hamsters had
569 moderate necro-suppurative and hyperplastic bronchiolitis with intraluminal accumulation of
570 neutrophils and cellular debris (asterisk) as well as neutrophils transmigrating through the
571 bronchial epithelium into the lumen (arrowhead). The lung parenchyma presented with a
572 patchy distribution of acute necrosis (C, asterisk) with microvascular thrombosis (arrowheads)
573 or (D) with areas of dense infiltration by macrophages and neutrophils. (E) Pulmonary blood
574 vessels had mild to moderate endothelialitis. (F-I) In contrast, lungs of hamsters treated with
575 ensovibep on the day of infection developed (F) moderately less consolidation of their lungs.
576 (G) Bronchiolitis was milder with less inflammatory cell infiltrate compared to the untreated
577 group. Neutrophils were mostly absent. (H) Alveolar walls were only moderately expanded
578 by neutrophils and macrophages with less alveolar edema compared to untreated
579 hamsters. (I) Endothelialitis was virtually absent with marginating neutrophils as only immune
580 cells interacting with the vascular lining. (J-M) Hamsters treated with the antibody cocktail at
581 the day of infection developed lesions that were similar to those as described for the ensovibep
582 treated group.

583 (N-W) In contrast, lungs of hamsters treated at 1 dpi had lesions similar to the untreated
584 hamsters at that time, regardless of their treatments. (O, T): Both treatment groups developed
585 moderate bronchiolitis similar to the untreated group. (P, U): Lung parenchyma were
586 characterized by interstitial (asterisks) and alveolar (arrowheads) infiltration with neutrophils
587 and macrophages with variable necrosis of alveolar epithelial cells. Additional lesions in both
588 treatment groups included (Q) moderate to marked alveolar edema (asterisk), here shown for
589 the ensovibep group, and (V) moderate interstitial edema (asterisk), here shown for the
590 antibody group. (R, W): Both treatment groups developed moderate endothelialitis with
591 mononuclear infiltrates underneath detached endothelial cells, similar to the untreated
592 group.

593 Scale bars: A, F, J, N, S = 1 mm; B, G, K, O, T = 50 μ m; C, D, H, L, P, Q, U, V = 20 μ m; E, I,
594 M, R, W = 20 μ m

595 Histopathologic lesions were scored semi-quantitatively and scores plotted as graphs for
596 histologic signs of general inflammation and histologic parameters of bronchiolar, alveolar and
597 vascular lesions at day 2/3 p.i (X) or day 5 p.i. (Y).

598

599

600

601

602

603

604

605

606

607

Supplementary Materials for

608

609

Ensovibep, a novel trispecific DARPin candidate that

610

protects against SARS-CoV-2 variants

611

612

Rothenberger et al. 2021

613 **Materials and Methods**

614 *Generation of His-tagged monovalent RBD binders and ensovibep*

615 DARPin constructs selected and cloned as described in Walser et al.³¹ were transformed in *E.coli* BL21
616 cells, plated on LB-agar (containing 1% glucose and 50 µg/mL ampicillin) and then incubated overnight
617 at 37°C. A single colony was picked into TB medium (containing 1% glucose and 50 µg/mL ampicillin)
618 and incubated overnight at 37°C, shaking at 230 rpm. Fresh TB medium (containing 50 µg/mL ampicillin)
619 was inoculated with 1:20 of overnight culture and incubated at 37°C at 230 rpm. At OD₆₀₀ = 1.1 the
620 culture was induced by addition of IPTG (0.5 mM final concentration) and incubated further for 5 h at
621 37°C and 230 rpm. Harvest was done by centrifugation (10 min, 5000 x g). After cell disruption by
622 sonication, primary recovery was done by heat treatment for 30 min at 62.5°C and subsequent
623 centrifugation (15 min, 12000 x g). 20 mM Imidazole and 1% Triton X-100 was added to the supernatant
624 and the 0.22 µm filtered supernatant was further purified by immobilized metal affinity
625 chromatography (IMAC) (HisTrap FF crude, Cytiva, Sweden) using the N-terminal His-tag and including
626 a wash step with 1% Triton X-100 and a step elution with 250 mM Imidazole. In a subsequent step, the
627 elution fraction of the IMAC step was applied on a size exclusion chromatography (Superdex 200, Cytiva,
628 Sweden) and fractions of interest were pooled and concentrated. Finally, the concentrated sample was
629 filtered through a 0.22 µm Mustang E filter for Endotoxin removal and sterile filtration and quality
630 controlled.

631 *Cryo-electron microscopy*

632 4 µl of purified S-ectodomain (9 µM) was mixed with 1 µl of 50 µM mono-DARPin R2, and incubated for
633 15 seconds at room temperature. 3 µl of sample was then dispensed on Quantifoil R1.2/1.3 200-mesh
634 grids (Quantifoil Micro Tools GmbH) that had been freshly glow discharged for 30 s at 20 mA. Grids
635 were blotted using blot force +2, for 5 s using Whatman No. 1 filter paper and immediately plunge-
636 frozen into liquid ethane cooled by liquid nitrogen using a Vitrobot Mark IV plunger (Thermo Fisher
637 Scientific) equilibrated to ~95% relative humidity, 4°C. Movies of frozen-hydrated specimens were
638 collected using Glacios Cryo-TEM (Thermo Fisher Scientific) operating at 200 keV and equipped with a
639 Falcon 4 Direct Electron Detector (Thermo Fisher Scientific). For additional analysis of monovalent
640 DARPin R2, 4 µl of purified S-ectodomain (18 µM) was mixed with 1 µl of 100 µM DARPin, and incubated
641 for 60 s at room temperature. Grids were prepared as described above, and movies were collected
642 using a Titan Krios Cryo-TEM (Thermo Fisher Scientific) operating at 300 keV and equipped with a Falcon
643 4 Direct Electron Detector (Thermo Fisher Scientific). All cryo-EM data were acquired using the EPU 2
644 software (Thermo Fisher Scientific) with a 30-degree stage tilt to account for preferred orientation of

645 the samples. Movies were collected in electron counting mode at 92,000x (Glacios) or 75,000x (Titan
646 Krios), corresponding to a pixel size of 1.1 Å/pix or 1.045 Å/pix over a defocus range of -1.25 to -2.5 µm.

647 *Image processing*

648 Movie stacks were manually inspected and then imported in Relion version 3.1⁶⁰. Drift and gain
649 correction were performed with MotionCor2⁶¹, and GCTF⁶² was used to estimate the contrast transfer
650 function for each movie. Particles were automatically picked using the Laplacian-of-Gaussian (LoG)
651 algorithm and then Fourier binned (2 x 2) particles were extracted in a 160-pixel box. The extracted
652 particles were subjected to two rounds of 2D classification, ignoring CTFs until the first peak. Using the
653 ‘molmap’ command in UCSF chimera⁶³, a SARS-CoV-2 spike structure (PDB ID: 6VSB)⁶⁴ was used to
654 generate a 50Å resolution starting model for 3D classification. Particles selected from 2D classification
655 were subject to a single round of 3D classification (with C1 symmetry). Particles belonging to the best
656 classes were re-extracted unbinned in a 320-pixel box, 3D auto-refined (with C1 or C3 symmetry) and
657 post-processed. Iterative rounds of per particle defocus estimation, 3D auto-refinement and post-
658 processing were used to account for the 30-degree stage tilt used during data collection. When CTF
659 refinement did not yield any further improvement in resolution, Relion’s Bayesian polishing procedure
660 was performed on the particle stacks, with all movie frames included, followed by 3D auto-refinement
661 and post-processing. Subsequently, additional rounds of per particle defocus estimation, 3D auto-
662 refinement and post-processing were performed on the polished particles until no further
663 improvement in resolution or map quality was observed. The nominal resolution for each map was
664 determined according to the ‘gold standard’ Fourier shell correlation (FSC) criterion (FSC = 0.143) and
665 local resolution estimations were performed using Relion. Map sharpening was performed using
666 DeepEMhancer⁶⁵ as implemented in COSMIC2⁶⁶. To improve the quality of the mono-DARPin R2 density
667 in the fully open spike reconstruction, a focused 3D classification approach was employed. Briefly, each
668 particle contributing to the final C3-symmetry-imposed reconstruction was assigned three orientations
669 corresponding to its symmetry related views using the “relion_particle_symmetry_expand” tool. A soft
670 mask was placed over the map to isolate the mono-DARPin R2-bound RBD, and the symmetry-
671 expanded particles were subjected to masked 3D classification without alignment using a regularization
672 parameter (‘T’ number) of 20. Particles corresponding to the 3D class with the best resolved DARPin
673 density were re-extracted in a 200-pixel box and centered on the mask used for focused classification.
674 In conjunction with this, the signal for the protein outside the masked was subtracted. The re-extracted
675 particles were then 3D auto-refined (with C1 symmetry) using local angular searches (1.8 degrees) and
676 sharpened using DeepEMhancer⁶⁵. Three copies of the locally refined map were aligned to the globally
677 refined map using the UCSF Chimera ‘fit in map’ tool and resampled using the ‘vop resample’ command.

678 Finally, a composite map was generated using the “vop add” command. An overview of the image
679 processing workflows is shown in supplementary Figure 2A.

680 *Molecular modeling of mono and multivalent DARPin molecules*

681 Homology models of monovalent DARPin molecules R1, R2 and R3 were generated with Rosetta⁶⁷⁻⁶⁹.
682 The consensus designed ankyrin repeat domain PDB ID:2XEE was used as template. Mutations were
683 introduced with RosettaRemodel with fixed backbone, and the structure was refined with RosettaRelax.
684 Forty refined structures were clustered using RosettaCluster with 0.3 Å radius, and the lowest-energy
685 model from the largest cluster served as the final model. The UCSF Chimera ‘fit in map’ tool was used
686 to fit the monovalent DARPin R2 model into the cryo-EM map produced from focused refinement. This
687 fitted model of DARPin R2, together with the RBD domain (PDB ID:6MOJ) was further refined with
688 Rosetta. The structure was pre-relaxed for docking and served as input for local, high-resolution docking
689 with RosettaDock with fixed backbone. Five hundred models were generated and clustered with 1 Å
690 radius (RosettaCluster). Two largest clusters were inspected and the lowest-energy model from more
691 conserved group (i.e., with lower rigid-body perturbation from the input structure) was taken further
692 for additional all-atom refinement with RosettaRelax, with protocol optimized for interfaces
693 (InterfaceRelax2019). Fifty models were generated, and the lowest scoring model was selected. This
694 model was used to describe the interactions between DARPin R2 and the RBD. The PDB file with the
695 coordinates of the trimer of DARPin R2:RBD was used as an input structure for the conceptual modeling
696 of ensovibep bound to the spike ectodomain as shown in Figure 1G. The linkers were generated using
697 Rosetta modeling tools. Figures were generated using LigPlot⁷⁰, UCSF Chimera⁶³, UCSF ChimeraX⁷¹,
698 PyMOL (The PyMOL Molecular Graphics System, Version 2.0, Schrödinger, LLC) and BioRender
699 (BioRender.com).

700 *Generation of monoclonal antibodies*

701 Publicly available sequences of variable domains from monoclonal antibodies were used to synthesize
702 the corresponding cDNA fragments and cloned into a proprietary expression vector at Evitria AG
703 (Schlieren, Switzerland). Generated vectors containing the constant immunoglobulin chains were used
704 for transfection in Chinese hamster ovary cells by Evitria. Sterile filtered cell supernatants were purified
705 via affinity purification with HiTrap MabSelect column followed by a size exclusion chromatography
706 using HiLoad 26/600 Superdex 200 column in PBS pH7.4. Selected fractions were pooled and quality
707 controlled (by SDS-PAGE, size exclusion chromatography and endotoxin measurement) before use in
708 assays.

709 ***VSV-SARS-CoV-2 pseudotype mutation-vector generation***

710 Plasmid pCAGGS containing the Wuhan-hu-1 spike protein of SARS-CoV-2³¹ was used as a reference
711 and as a template for generation of single and multiple spike protein mutants. Forward and reverse
712 complementary primers encoding the mutation were synthesized by Microsynth (Balgach, Switzerland).
713 High-fidelity Phusion polymerase (New England Biolabs, USA) was used for all DNA amplification.

714 Single mutations of the spike protein were generated via two PCR fragments of the spike ORF using
715 high-fidelity Phusion polymerase (New England Biolabs, USA). The first fragment was generated via a
716 generic forward primer (pCAGGS-5) annealing upstream of the spike ORF and the specific reverse
717 primer encoding the mutation. The second fragment was generated using the specific forward primer
718 encoding the mutation and a reverse primer (rbglobpA-R). The two fragments were gel-purified and
719 used as input for an assembly PCR without addition of flanking primers.

720 For multi-mutation spike proteins, a complementary pair of primers (forward and reverse) encoding
721 each mutation was designed. Fragment 1 was generated with forward primer pCAGGS-5 and reverse
722 primer encoding mutation 1. Fragment 2 was generated using forward primer encoding mutation 1 and
723 reverse primer encoding mutation 2. All subsequent fragments were generated analogously. DNA
724 fragments were gel-purified and mixed in equimolar amounts. This mix was used for re-assembly of the
725 full spike ORF using outer primers pCAGGS-5 (GGTTCGGCTTCTGGCGTGTGACC) and rbglobpA-R
726 (CCCATATGTCCTCCGAGTG).

727 For both single as well as multi-mutation spike protein, the full-length spike ORF was isolated from an
728 agarose gel, digested by restriction enzymes NheI/EcoRI and inserted into the pCAGGS vector
729 backbone. The correct sequence was verified via sequencing the whole ORF of the spike protein by
730 Microsynth (Balgach, Switzerland).

731 ***VSV-SARS-CoV-2 pseudotype neutralization assay for mutational analysis***

732 The pseudotype viral system was based on the recombinant VSV*DELG-Luc vector in which the
733 glycoprotein gene (G) had been deleted and replaced with genes encoding green fluorescent protein
734 and luciferase. For the neutralization assay of ensovibep, MPO420 or their his-tagged variants
735 ALE049/ALE070, an initial dilution of the compounds was followed by three-fold dilutions in
736 quadruplicates in DMEM-2 % [vol/vol] FCS supplemented with 20 µM human serum albumin (CSL
737 Behring). The mixture was mixed with an equal volume of DMEM-2 % FCS containing 250 infectious
738 units (IU) per well of SARS-CoV-2 pseudoviruses and incubated for 90 min at 37°C. The mix was
739 inoculated onto Vero E6 cells in a clear bottom white walled 96-well plate during 90 min at 37°C. The
740 inoculum was removed and fresh medium added, and cells further incubated at 37°C for 16 h. Cell were

741 lysed according to the ONE-Glo™ luciferase assay system (Promega, Madison, US) and light emission
742 was recorded using a Berthold TriStar LB941 luminometer. The raw data (relative light unit values) were
743 exported to GraphPad Prism v8.4.3. IC50/IC90 were modelled with a nonlinear regression fit with
744 settings for log (inhibitor) vs normalized response curves. Data points are plotted by the mean ± SEM
745 (standard error of mean) of quadruplicate data.

746 *SARS-CoV-2 lentivirus-based pseudovirus neutralization assay*

747 The neutralizing activity of therapeutic antibodies against SARS-COV-2 variants was measured using
748 lentiviral particles pseudotyped with spike proteins of SARS-COV-2 variants, as previously described⁷².
749 Briefly, pseudoviruses bearing the spike proteins and carrying a firefly luciferase⁷³ reporter gene were
750 produced in 293T cells by co-transfection of pCMVΔR8.2, pHR'CMVLuc and pCDNA3.1-spike variants.
751 Plasmids encoding human codon-optimized spike genes with the desired mutations were purchased
752 (GenScript, Piscataway, NJ). Supernatants containing pseudoviruses were collected 48 h post-
753 transfection, filtered through a 0.45 μm low protein binding filter, and stored at -80oC. Pseudovirus
754 titers were measured by infecting 293T-ACE2.TMPRSS2s cells for 48 h prior to measuring luciferase
755 activity (Luciferase assay reagent, Promega, Madison, WI). For neutralization assays, pseudoviruses with
756 titers of approximately 10⁶ relative luminescence units (RLU)/ml were incubated with serially diluted
757 DARPin for two h at 37°C before adding the pseudovirus and DARPin mixtures (100 μl) onto 96 well
758 plates pre-seeded one day earlier with 3.0 x 10⁴ 293T-ACE2.TMPRSS2s cells/well. Pseudovirus infection
759 was scored 48 h later by measuring luciferase activity. The DARPin concentration causing a 50%
760 reduction of RLU compared to control (ID50) was reported as the neutralizing DARPin titer. Titers were
761 calculated using a nonlinear regression curve fit (GraphPad Prism software Inc., La Jolla, CA). The ratio
762 of the neutralizing DARPin titer of the variant compared to the neutralizing DARPin titer of wild-type
763 reference was calculated. The D614G mutation background was used for the variants and the reference
764 virus. The mean titer from at least two independent experiments with intra-assay duplicates was
765 reported as the final titer. This work was performed independently by investigators at the US Food and
766 Drug Administration, Center for Biologics Evaluation and Research as part of Therapeutics Research
767 Team for the US government COVID-19 response efforts.

768 *SARS-CoV-2 lentivirus-based pseudovirus neutralization assay (Setup 2)*

769 Neutralizing activity was measured in an assay that utilized lentiviral particles pseudotyped with full-
770 length SARS-CoV-2 Spike protein and containing a firefly luciferase (Luc) reporter gene for quantitative
771 measurements of infection by relative luminescence units (RLU). The backbone vector used in
772 pseudovirus creation, F-lucP.CNDOΔU3, encodes the HIV genome with firefly luciferase replacing the
773 HIV env gene. A codon-optimized version of the full-length spike gene of the Wuhan-1 SARS-CoV-2

774 strain (MN908947.3; GenScript) was cloned into the Monogram proprietary env expression vector,
775 pCXAS-PXMX, for use in the assay. The D614G spike mutation was introduced into the original Wuhan
776 sequence by site-directed mutagenesis. Sequences of the spike gene and expression vector were
777 confirmed by full-length sequencing using Illumina MiSeq NGS.

778 Pseudovirus stock was produced in HEK 293 cells via a calcium phosphate transfection using a
779 combination of spike plasmid (pCXAS-SARS-CoV-2-D614G) and lentiviral backbone plasmid (F-
780 lucP.CNDOΔU3). Transfected 10 cm² plates were re-fed the next day and harvested on Day 2 post
781 transfection. The pseudovirus stock (supernatant) was collected, filtered and frozen at -70°C in single
782 use aliquots. Pseudovirus infectivity was screened at multiple dilutions using HEK293 cells transiently
783 transfected with ACE2 and TMPRSS2 expression vectors. RLU were adjusted to ~ 50,000 for use in the
784 neutralization assay. Neutralization was performed in white 96-well plates by incubating pseudovirus
785 with 10 serial threefold dilutions of samples for one hour at 37°C.

786 HEK293 target cells, which had been transfected the previous day with ACE2 and TMPRSS2 expression
787 plasmids, were detached from 10 cm² plates using trypsin/EDTA and re-suspended in culture medium
788 to a final concentration that accommodated the addition of 10,000 cells per well. Cell suspension was
789 added to the serum-virus mixtures and assay plates were incubated at 37°C in 7% CO₂ for 3 days. On
790 the day of assay read, Steady Glo (Promega) was added to each well. Reactions were incubated briefly
791 and luciferase signal (RLU) was measured using a luminometer. Neutralization titers represent the
792 inhibitory concentration (IC) of samples at which RLU were reduced by either 50% (IC₅₀) or 90% (IC₉₀)
793 compared to virus control wells (no sample wells). Data of single runs are represented. This work was
794 performed independently by investigators at Monogram Biosciences, CA, US, for the US government
795 COVID-19 response efforts.⁷⁴

796 *Cells and pathogenic virus*

797 Vero E6 cells (kindly provided by Prof. Volker Thiel, University of Bern, Switzerland) were passaged in
798 Minimum Essential Medium (MEM) (Cat N° M3303) containing 10% fetal bovine serum (FBS) and
799 supplements (2 mM L-Glutamine, 1% Non-essential amino acids, 100 units/ml Penicillin, 100 µg/ml
800 Streptomycin, 0.06% Sodium bicarbonate, all from Bioswisstec, Schaffhausen, Switzerland) at 37°C,
801 >85% humidity and 5% CO₂. Vero E6/TMPRSS2 cells^{75,76} obtained from the Centre For AIDS Reagents
802 (National Institute for Biological Standards and Control) were passaged in Dulbecco's Modified Eagle
803 Medium (DMEM) (Cat N° M1452) containing 10% fetal bovine serum (FBS) and supplements (2 mM L-
804 Glutamine, 1% Non-essential amino acids, 100 U/mL Penicillin, 100 µg/mL Streptomycin, 0.06% Sodium
805 bicarbonate and 2% Geneticin G418, all from Bioswisstec, Schaffhausen, Switzerland) at 37°C, >85%
806 humidity and 5% CO₂.

807 SARS-CoV-2 (2019-nCoV/IDF0372/2020), kindly provided by Dr. Sylvie van der Werf from the National
808 Reference Centre for Respiratory Viruses hosted by Institut Pasteur (Paris, France) was propagated in
809 Vero E6 cells in MEM containing 2% FBS and supplements (2%-FBS-MEM) at 37°C, >85% humidity and
810 5% CO₂. SARS-CoV-2 variants (B.1.1.7, B.1.351 and P.1) were provided from University Hospital of
811 Geneva, Laboratory of Virology²⁵ and propagated in Vero E6/TMPRSS2 cells in DMEM containing 2%
812 FBS and supplements (2%-FBS-DMEM) at 37°C, >85% humidity and 5% CO₂. Viral titer was determined
813 by standard plaque assay, by incubating 10-fold serial dilutions of the virus for 1 h at 37°C on a confluent
814 24-well plate with Vero E6 cells. Then inoculum was removed and 1 mL overlay medium (20 ml
815 Dulbecco's Modified Eagle's Medium, 5 ml FBS, 100 U/mL Penicillin, 100 µg/mL Streptomycin, and 25
816 ml Avicel rc581) was added. After 3 days incubation at 37°C the overlay was removed and the plates
817 stained with crystal violet solution (spatula tip (~4 mg) crystal violet powder (Sigma Aldrich) solved in
818 30 ml 37% formalin and 120 mL PBS (Sigma Aldrich).

819 *Viral passaging experiment with authentic SARS-CoV-2*

820 Virus escape studies were adapted from a previously published protocol by Baum et al.²⁷. Briefly, 1:5
821 serial dilutions of DARPin molecules and monoclonal antibodies from 100 µg/mL to 0.032 µg/mL were
822 prepared in Minimum Essential Medium (MEM) containing 2% FBS, supplements and 10 µM human
823 serum albumin (HSA; CSL Behring, Switzerland; 2%-FBS-MEM + HSA). 500 µL of virus suspension
824 containing 1.5 x 10⁶ plaque forming units (pfu) SARS-CoV-2 in 2%-FBS-MEM + HSA were mixed with 500
825 µL of serially diluted DARPin molecules or monoclonal antibodies and subsequently incubated for 1
826 hour at 37°C. The mixtures were then transferred to confluent Vero E6 cells in 12 well plates and
827 incubated for 4 days at 37°C, >85% humidity and 5% CO₂. Each culture well was assessed for cytopathic
828 effect (CPE) by microscopy. Supernatant was removed from wells with the highest DARPin or antibody
829 concentrations showing significant CPE (≥20%) and used for total RNA extraction and further passaging.
830 For subsequent rounds of passaging, remaining 900 µL supernatant of selected wells was diluted in 4
831 mL in 2%-FCS-MEM + HSA and from the 4.9 mL, 500 µL mixed with serial dilutions of DARPin molecules
832 or antibodies, incubated and the mixture transferred to 12-well plates with fresh Vero E6 cells as
833 described above. Cell culture wells were assessed for CPE again after 4 days and the supernatant of
834 wells with highest DARPin or antibody concentrations with evident viral replication (CPE) harvested and
835 used for additional passages. A total of 4 passages were performed this way.

836

837

838

839 Deep sequencing of viral passages

840 RNA of the cell culture supernatant was extracted using the RNeasy Universal Plus kit (Qiagen, Basel,
841 Switzerland) according to the manufacturer's protocol. 10.5 μ L of the extract was reverse transcribed
842 using Superscript VILO (ThermoFisher Scientific, Reinach, Switzerland) following the manufacturer's
843 instructions. Barcoded libraries were prepared on the Ion Chef Instrument (ThermoFisher Scientific)
844 using the Ion AmpliSeq SARS-CoV-2 Research Panel (ThermoFisher Scientific). 8-16 barcoded samples
845 were pooled and loaded on one Ion 530 chip using the Ion Chef Instrument (ThermoFisher Scientific)
846 and sequenced on the Ion S5 System with 550 flows.

847 The resulting BAM files were converted to fastq format using Samtools 1.10⁷⁷ and subjected to adapter
848 and quality trimming using Trimmomatic 0.39⁷⁸ (options: ILLUMINACLIP:adapters.fasta:2:30:10,
849 LEADING: 3, TRAILING: 3, SLDINGWINDOW:4:15, MINLEN:36). Reads were aligned to the SARS-CoV-2
850 reference genome (NC_045512.2) using bwa 0.7.17⁷⁹ and variants were determined using LoFreq
851 v2.1.5⁸⁰. Variants were filtered for a minimal depth (DP) of 400X and a minimal allele frequency (AF) of
852 3% using bcftools 1.10⁷⁷. Functional annotation of the variants was performed using SNPEff 5.0⁸¹.
853 Variants were visualized in R 3.6.1 using ComplexHeatmap 2.2⁸².

854 *Virus neutralization of authentic wild type and variants of SARS-CoV-2 determined by Cell Titer-Glo*

855 Virus neutralization capacity of mono-valent DARPin candidate and multispecific DARPin molecules was
856 determined for 100 TCID₅₀ SARS-CoV-2 variants from lineage B.1.1.7 (H69_V70del, Y145del, N501Y,
857 A570D, D614G, P681H, T716I, S982A, D1118H), B.1.351 (L18F, D80A, D215G, L242_L244del, T302T,
858 K417N, E484K, N501Y, D571D, D614G, A701V) and P.1 (L18F, T20N, P26S, D138Y, R190S, K417T, E484K,
859 N501Y, D614G, H655Y, T1027I, V1176F) in reference to a wild-type French isolate (with the following
860 differences to the Wuhan wild-type: V367F; E990A) by measuring ATP levels of protected cells in a cell
861 viability assay. DARPin molecules were serially diluted 1:4 from 40 nM to 2.4 pM (in triplicates) in 100
862 μ L cell culture medium (2%-FBS-DMEM) supplemented with 10 μ M HSA in 96 well plates. The diluted
863 DARPin antivirals were mixed with 100 TCID₅₀ SARS-CoV-2 in 100 μ L 2%-FBS-MEM + HSA and incubated
864 for 1 h at 37°C. DARPin/virus mixtures (200 μ L) were transferred onto confluent Vero E6/TMPRSS2 cells.
865 The controls consisted of cells exposed to virus suspension only, to determine maximal cytopathic
866 effect and of cells incubated with medium only, to determine baseline cell viability. The plates were
867 incubated for 3 days at 37°C, >85% humidity and 5% CO₂. Cell viability was determined by removing
868 100 μ L supernatant from all wells and adding 100 μ L CellTiter-Glo reagent to the cells as described in
869 the manufacturers protocol (CellTiter-Glo[®] Luminescent Cell Viability Assay, Promega, Madison, USA).
870 After 2 minutes shaking on an orbital shaker, lysis of the cells during 10 min and transfer to an opaque-
871 walled plate at room temperature, luminescence was read using a GloMax instrument (Promega).

872 *Surface plasmon resonance (SRP) affinity determination of ensovibep and individual RBD-binding*
873 *domains*

874 SPR assays were used to determine the binding affinity of monovalent DARPin as well as multivalent
875 DARPin molecules to the spike protein of SARS-CoV-2. All SPR data were generated using a Bio-Rad
876 ProteOn XPR36 instrument with PBS-T (0.005% Tween20) as running buffer. A new neutravidin sensor
877 chip (NLC) was air-initialized and conditioned according to Bio-Rad manual.

878 Monovalent DARPin molecules R1, R2, R3: Chemically biotinylated (via lysines) SARS-CoV-2 spike
879 protein 20 (Sino Biologicals) was captured to ~3400 RUs (30 µg/mL, 30 µL/min, 300 s). Two buffer
880 injections (100 µL/min, 60 s) followed by two 12.5 mM NaOH regeneration steps (100 µL/min, 18 s)
881 were applied before the first injections. Mono-domain DARPin proteins were injected (at
882 50/16.7/5.6/1.9/0.6 nM) for 180 s at 100 µL/min for association and dissociation was recorded for
883 3600 s (at 100 µL/min). The ligand was regenerated with a 12.5 mM NaOH pulse (100 µL/min, 18 s).
884 The data was double referenced against the empty surface and a buffer injection and fitted according
885 to the 1:1 Langmuir model.

886 Multivalent DARPin molecules: Avi-tagged biotinylated SARS-CoV-2 S protein (Acro Biosystems) was
887 captured to ~1200 RUs (1.33 µg/mL, 30 µL/min, 300 s) on a pre-coated neutravidin chip (NLC). Two
888 buffer injections (100 µL/min, 60 s) followed by three 12.5 mM NaOH regeneration steps (100 µL/min,
889 18s) were applied before the first injections. One single concentration of 20 nM of ensovibep was
890 injected for 180 s at 100 µL/min for association and dissociation was recorded for 36'000 s (at
891 100 µL/min). The data was double referenced against the empty surface and a buffer injection. Due to
892 avidity gain, no significant dissociation could be recorded during the measured time.

893 *Surface plasmon resonance (SRP) affinity determination of wt-RBD and RBD F486V to ACE2*

894 SPR assays were used to determine the binding affinity of wt-RBD as well as RBD-F486V human ACE2
895 protein. SPR data were generated using a Bruker Sierra SPR-32 Pro instrument with PBS-T (0.005%
896 Tween20) as running buffer. A Bruker biotin tag capture sensor chip (BTC) was initialized and
897 conditioned according to Bruker manual.

898 Avi-tagged biotinylated monomeric human ACE2 (Acro Biosystems) was captured to ~170 RUs
899 (3.3 µg/mL, 10 µL/min, 60 s). SARS-CoV-2 S protein RBD (wt, Acro biosystems, 500nM-0.229nM,
900 threefold dilution series) and SARS-CoV-2 S protein RBD-F486V (in-house produced, 1500nM-0.229nM,
901 threefold dilution series) were injected for 240 s at 25 µL/min for association and dissociation was
902 recorded for 300 s (at 25 µL/min). After each injection, a 15min pause was performed to ensure full

903 dissociation of analyte from the ligand. The data was double referenced against the empty surface and
904 a buffer injection and fitted according to the 1:1 Langmuir model.

905 *Roborovski dwarf hamster model for the assessment of antiviral potency of ensovibep on wild type SARS-*
906 *CoV-2 and the B.1.1.7 (alpha) variant*

907 Materials and Methods

908 1. Cells and viruses

909 For in vivo experiments, SARS-CoV-2 isolates BetaCoV/Germany/BavPat1/2020⁸³ and
910 BetaCoV/Germany/ChVir21652/2020 (B.1.1.7) were grown on Vero E6 cells and whole genome
911 sequenced prior to infection experiments to confirm genetic integrity. Particularly the presence and
912 integrity of the furin cleavage site in the majority of the virus population was confirmed. All virus stocks
913 were titrated on Vero E6 cells prior to infection.

914 2. Animals and infection

915 A total of 120 female and male Roborovski dwarf hamsters (*Phodopus roborovskii*) was used for
916 infection experiments. Animals were housed in groups of 3 to 6 animals of the same sex in individually
917 ventilated GR900 cages (Tecniplast, Buguggiate, Italy) and provided with food and water ad libitum and
918 bountiful enrichment (Carfil, Oud-Turnhout, Belgium). Infection was performed by intranasal
919 administration of 1×10^5 pfu SARS-CoV-2 in 20 μ L cell culture medium under general anesthesia³⁸. All
920 animal procedures were performed in accordance with relevant institutional and legal regulations and
921 approved by the responsible state authority, Landesamt für Gesundheit und Soziales Berlin, Germany,
922 permit number G 0086/20.

923 3. Treatment

924 DARPin molecules and monoclonal antibodies were administered intraperitoneally in sterile PBS. The
925 final drug concentration was adjusted based on the desired dose and respective animal weight to a 100
926 μ L injection volume. For intraperitoneal administration the animal was fixed by grasping the neck skin
927 and the back skin between thumb and fingers. Subsequently, the hand was turned over so that the
928 animal rests with its back in the palm of the hand. The head of the animal was kept downwards to
929 prevent injection/damage in/of the organs and the needle was inserted left of the median line in the
930 groin area, between the 4th and the 5th mammary gland/nipple. Finally, the needle was removed in a
931 smooth motion. All animals in this study were treated once at the indicated time point, 0, 6 or 24 hours
932 post infection.

933

934 4. Experimental groups

935 From a total of 120 Roborovski dwarf hamsters, 54 were used to determine dose and time dependency
936 of treatment success. In these cohorts, 6 animals per group were infected with 1×10^5 pfu SARS-CoV-2
937 WT (BetaCoV/Germany/BavPat1/2020) and treated with either 3, 10 or 20 mg/kg ensovibep at the time
938 of infection, with 1 or 20 mg/kg 6 h post infection, or with 10 mg/kg 24h post infection, a placebo (PBS)
939 treatment group with 6 animals was also included in each of three studies performed for this purpose.
940 (Suppl. Figure 7)

941 To compare efficacy of ensovibep and Regeneron antibody cocktail treatment, 60 animals were
942 infected with 1×10^5 pfu SARS-CoV-2 variant B.1.1.7 (BetaCoV/Germany/ChVir21652/2020). Subjects
943 were divided into groups of 12 animals and treated with 10 mg/kg ensovibep, 10 mg/kg Regeneron
944 mAb cocktail or a placebo (PBS) at the time of infection or with 10 mg/kg ensovibep or 10 mg/kg
945 Regeneron mAb cocktail 24 h post infection. An additional 6 animals served as non-infected control
946 group.

947 In all animal experiments performed in this study, half of each respective group was scheduled for take
948 out at 3 dpi, the other half was to be terminated at 5 dpi. In some of the experiments, several animals
949 had to be terminated at time points other than these for humane reasons. Defined humane endpoints
950 included a body temperature $< 33^\circ\text{C}$, body weight loss $> 15\%$ together with signs of respiratory distress,
951 body weight loss $> 20\%$ or a combination of these factors. Animals were monitored at least twice a day
952 to prevent any prolonged suffering.

953 5. Virological analysis

954 RNA was extracted from throat swabs and lung tissue using the innuPREP Virus DNA/RNA Kit (Analytic
955 Jena, Jena, Germany). Viral RNA was quantified using a one-step RT qPCR reaction with the NEB Luna
956 Universal Probe One-Step RT-qPCR (New England Biolabs, Ipswich, MA, USA) and the 2019-nCoV RT-
957 qPCR primers and probe (E_Sarbeco)⁸⁴ on a StepOnePlus RealTime PCR System (Thermo Fisher
958 Scientific, Waltham, MA, USA) according to the manufacturer's instructions. Standard curves for
959 absolute quantification were generated from serial dilutions of SARS-CoV-2 DNA obtained from a full-
960 length virus genome cloned as a bacterial artificial chromosome and propagated in *E. coli*. Duplicate
961 10-fold serial dilutions were used to determine replication competent virus titers on confluent layers
962 of Vero E6 cells. To this end, serial dilutions of lung tissue homogenates were made and incubated on
963 Vero E6 monolayers for 2 hours at 37°C . Cells were washed and overlaid with semi-solid cell culture
964 medium containing 1.5% microcrystalline cellulose (Avicel) and incubated for 48 h at 37°C after which
965 plates were fixed with 4% formalin and stained with 0.75% crystal violet for plaque counting.

966 6. Histology

967 For histopathology, the left lung lobe was carefully removed, immersion-fixed in formalin, pH 7.0, for
968 48 h, embedded in paraffin, and cut in 2 µm sections. Slides were stained with hematoxylin and eosin
969 (HE) after dewaxing in xylene and rehydration in decreasing ethanol concentrations. Lung sections were
970 microscopically evaluated in a blinded fashion by a board-certified veterinary pathologist to assess the
971 character, distribution and severity of pathologic lesions using lung-specific inflammation scoring
972 parameters as described for other lung infection models before. Three different scores were used that
973 included the following parameters: (1) lung inflammation score including severity of (i) interstitial
974 pneumonia (ii) bronchiolitis, (iii) necrosis of bronchial and alveolar epithelial cells, and (iv) hyperplasia
975 of alveolar epithelial type II cells as well as (v) hyperplasia of bronchial epithelial cells; (2) immune cell
976 infiltration score taking into account the presence of (i) neutrophils, (ii) macrophages, and (iii)
977 lymphocytes in the lungs as well as (iv) perivascular lymphocytic cuffing; and (3) edema score including
978 (i) alveolar edema and (ii) perivascular edema. HE-stained slides were analyzed and images were taken
979 using an Olympus BX41 microscope with a DP80 Microscope Digital Camera and the cellSens™ Imaging
980 Software, version 1.18 (Olympus Corporation, Münster, Germany). For the display of overviews of
981 whole lung lobe sections, slides were automatically digitized using the Aperio CS2 slide scanner (Leica
982 Biosystems Imaging Inc., Vista, CA, USA), and image files were generated using the Image Scope
983 Software (Leica Biosystems Imaging Inc.). The percentages of lung tissues affected by inflammation
984 were determined histologically by an experienced board certified experimental veterinary pathologist
985 (O.K.) as described previously⁸⁵. Lung inflammation scores were determined as absent, (1) mild, (2)
986 moderate or (3) severe and quantified as described previously⁸⁵. Immune cell influx scores and edema
987 scores were rated from absent to, (1) mild, (2) moderate, or (3) severe.

988 7. Whole genome sequencing of SARS-CoV-2 isolated from treated hamsters

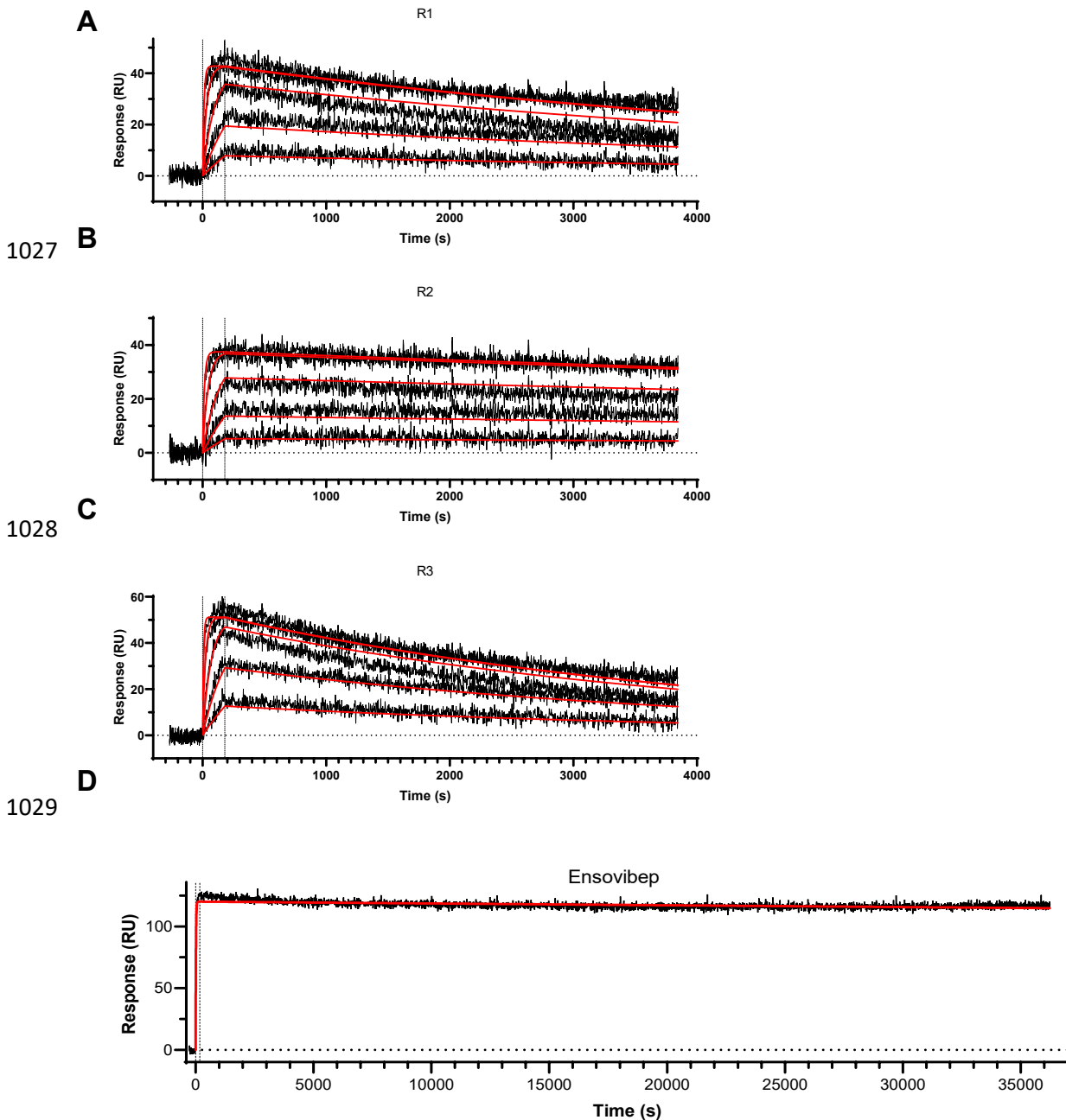
989 Following RNA extraction from swabs and lung samples, libraries were prepared and sequenced using
990 Illumina technology (Illumina, San Diego, California, USA). For library preparation, a multiplexed
991 amplicon-based whole-viral-genome approach using the NEBNext® ARTIC SARS-CoV-2 Library Prep Kit
992 (Illumina®) was employed (New England Biolabs, Ipswich, Massachusetts, USA). Briefly, this approach
993 relies on cDNA synthesis from total RNA and amplification of target SARS-CoV-2 cDNA using the V3
994 ARTIC primers; these amplicons then undergo the usual library preparation steps for Illumina
995 sequencing (end repair, adaptor ligation and PCR enrichment). Quantification of enriched sequencing
996 libraries was performed using the NEBNext® Library Quant Kit for Illumina® (New England Biolabs,
997 Ipswich, Massachusetts, USA). Libraries were then pooled and sequenced on an Illumina Miseq System
998 (Illumina, San Diego, California, USA).

999 The generated Illumina sequencing data were processed with Trimmomatic v.0.39⁷⁸ and mapped
1000 against genome reference MT270101.1, using the Burrows-Wheeler aligner v.0.7.17⁷⁹. Mapping
1001 statistics were generated using Samtools v1.10⁸⁶ and alignments were visualized using IGV v2.9.4 for
1002 Linux⁸⁷. For detection of single-nucleotide polymorphisms (SNPs), Freebayes, a Bayesian genetic variant
1003 detector was used. All SNPs with a minimum mapping quality of 5, minimum count of 3 and minimum
1004 fraction of 0.01 were considered. Consensus sequences for each sample were obtained using BCFtools.
1005 All SNP-containing open reading frame (ORFs) sequences were extracted from these consensus
1006 genomes and translated using the Expasy⁸⁸. Translate tool. The resulting protein sequences were then
1007 aligned to the corresponding reference protein sequences using the Expasy⁸ SIM Protein Alignment
1008 tool. For SNPs that resulted in amino acid substitutions, their possible effect on protein function was
1009 gauged using two predictors: PROVEAN Protein^{89 90} and SIFT⁹¹. Results from both predictors were taken
1010 into account, except on instances where the SIFT predictor could not resolve the proposed substitution
1011 or made “low confidence” predictions, then PROVEAN’s prediction was prioritized as its protein
1012 database is larger and newer.

1013 *Hamster pharmacokinetic study*

1014 Single intraperitoneal injections of 10 mg/kg were administered to female hamsters. Fifteen animals
1015 were enrolled in each study (n=3 per time point). Blood was sampled from individual animals at 2 h,
1016 24 h, 48 h, 72 h and 168 h post administration and processed to serum. MP0420 serum
1017 concentrations were determined by sandwich ELISA using an anti-DARPin antibody as capture reagent
1018 and biotinylated RBD and HRP conjugated Streptavidin as detection reagent and quantified against a
1019 standard curve. Serum concentrations for detection of both antibodies REGN10933 and REGN10987
1020 were determined by sandwich ELISA using an anti-IgG antibody as capture reagent and biotinylated
1021 RBD and HRP conjugated Streptavidin as detection reagent and using a standard curve.
1022 Pharmacokinetic parameters were determined with non-compartmental analyses using the software
1023 Phoenix WinNonLin (Certara, Princeton, USA) or GraphPadPrism (GraphPad Software, La Jolla, USA).
1024 For the *in vivo* efficacy study, terminal bleed samples were collected at 2, 3 or 5 days p.i. according to
1025 study description.

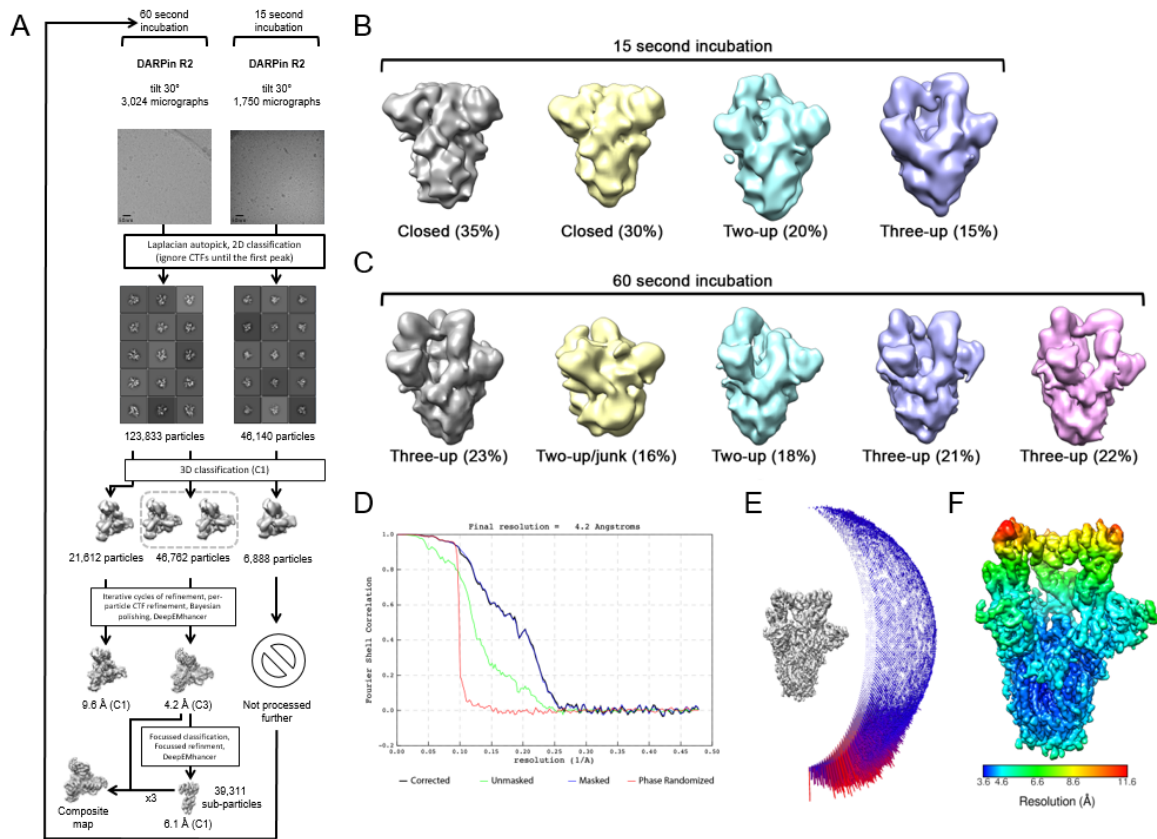
1026 Supplementary Figures



1030

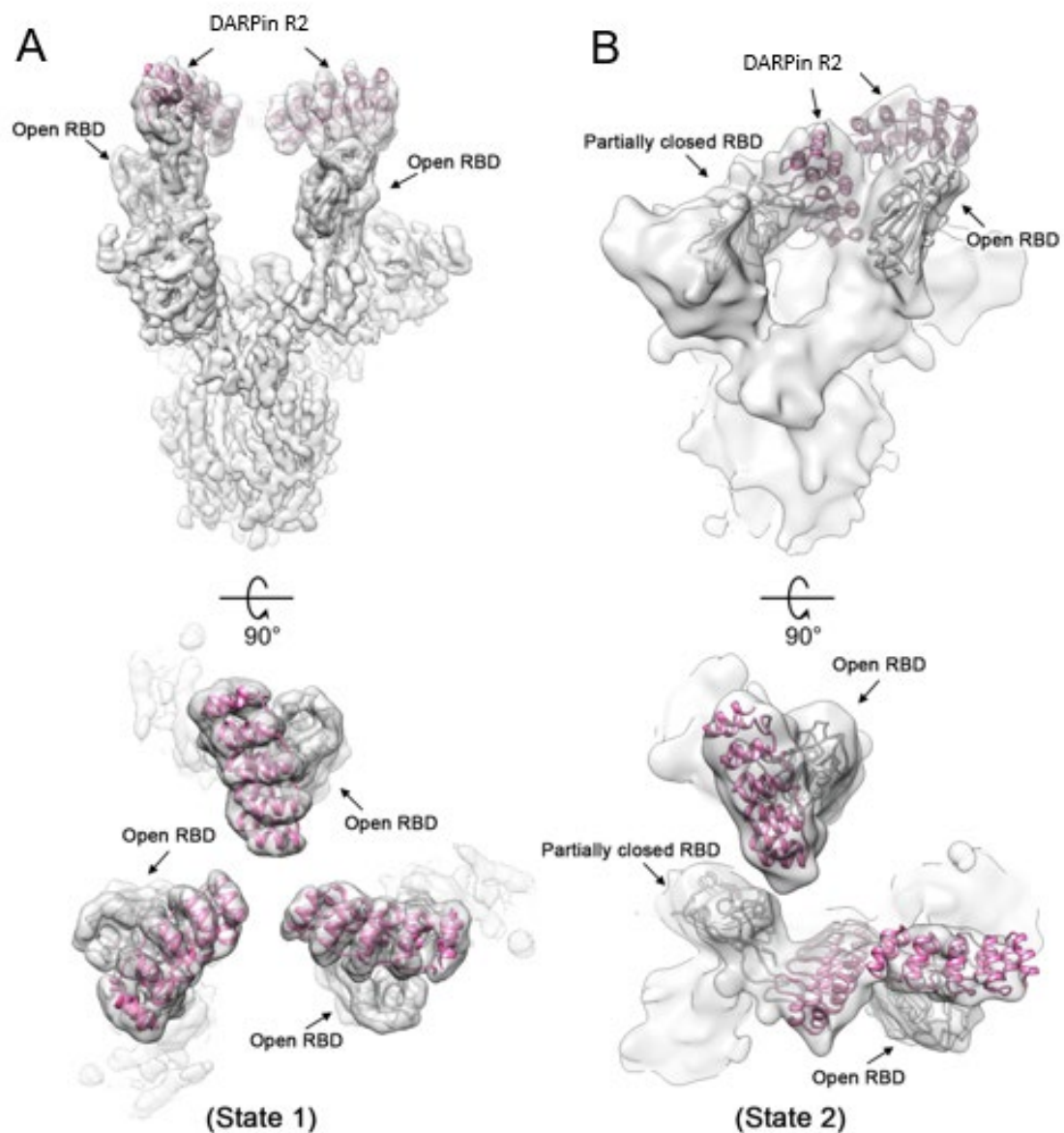
1031 **Supplementary Figure 1:** A-C) Surface plasmon resonance (SPR) sensorgrams of the
1032 monovalent DARPin modules (R1, R2, R3), incorporated in ensovibep binding to immobilized
1033 trimeric spike protein. DARPin concentrations for A-C: 50/16.67/5.56/1.85/0.62 nM.
1034 Determined K_D values: A) 80 pM, B) 30 pM, C) 90 pM. D) SPR sensorgram of ensovibep
1035 binding to immobilized spike protein. Off-rate was measured over 10 h and no physical off-
1036 rate could be determined by SPR due to very strong avidity of the three interlinked RBD
1037 binding modules.

1038



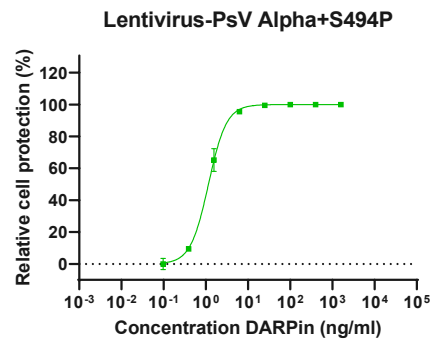
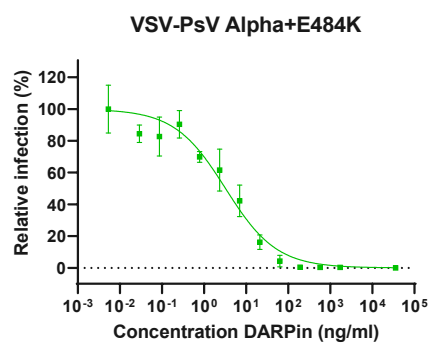
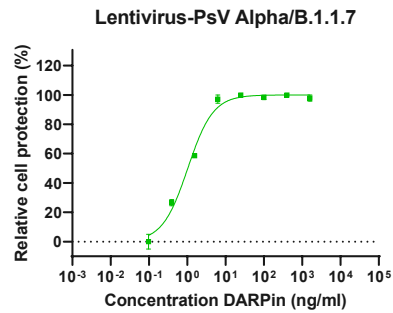
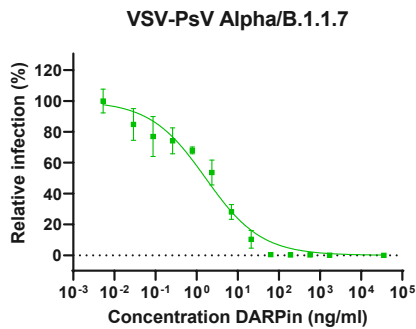
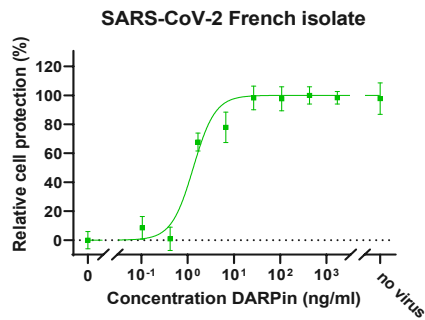
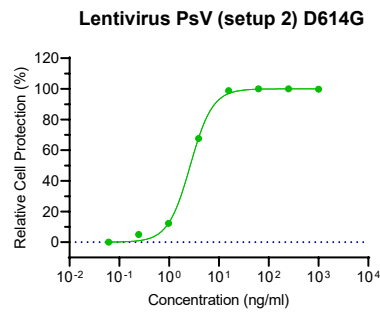
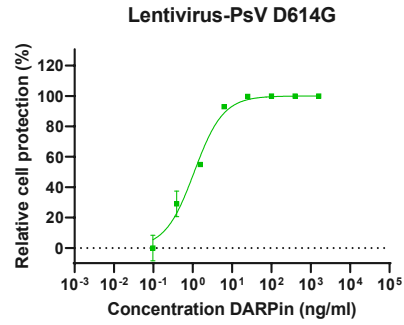
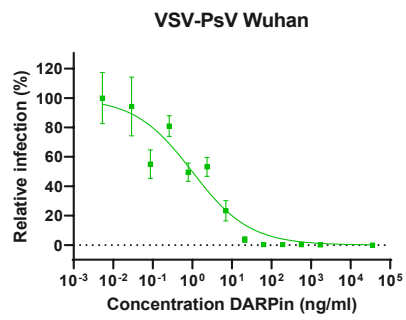
1039

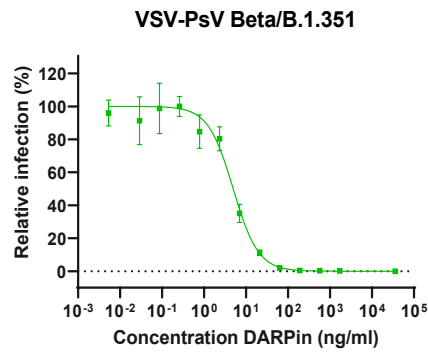
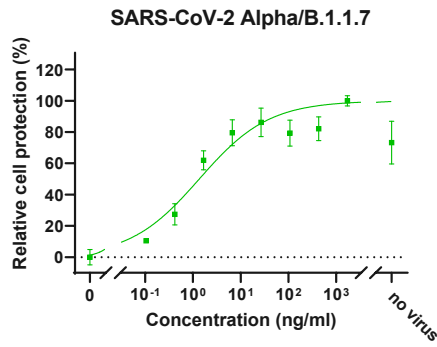
1040 **Supplementary Figure 2: Single-particle cryo-EM data processing.** A) Single-particle
 1041 cryo-EM image processing workflow for the monovalent DARPin R2 data collections. B) 3D
 1042 classes obtained from spike ectodomains incubated with monovalent DARPin R2 for 15
 1043 seconds, and C) for 60 seconds. D) Gold-standard Fourier shell correlation (FSC) curve
 1044 generated from the independent half maps contributing to the 4.2 Å resolution density map.
 1045 E) Angular distribution plot of the final C3 refined EM density map. F) The EM density map of
 1046 the spike ectodomain bound to three copies of monovalent DARPin R2, colored according to
 1047 local resolution.



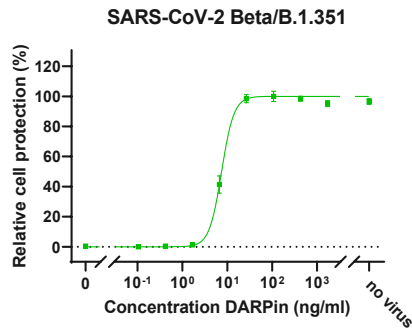
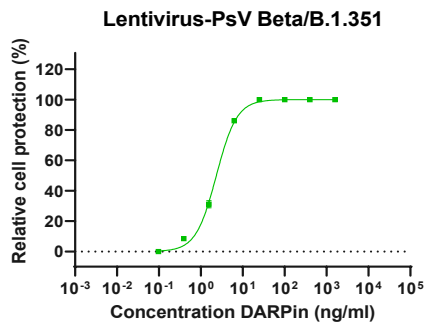
1048

1049 **Supplementary Figure 3: Monovalent DARPIn R2 prevents full closure of the RBD.** A)
1050 Cryo-EM density for state 1 and B) state 2 of the SARS-CoV-2 spike ectodomain in complex
1051 with the RBD targeting monovalent DARPIn R2, shown as two orthogonal views. The pseudo-
1052 atomic model of monovalent DARPIn R2 in complex with RBD, derived from molecular docking
1053 experiments, is fitted in each of the spike protomers and colored grey and pink, respectively.

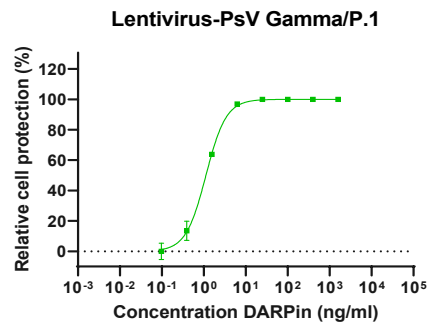
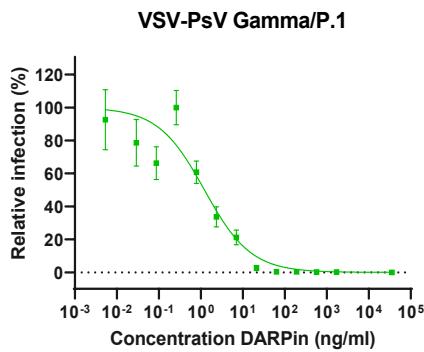




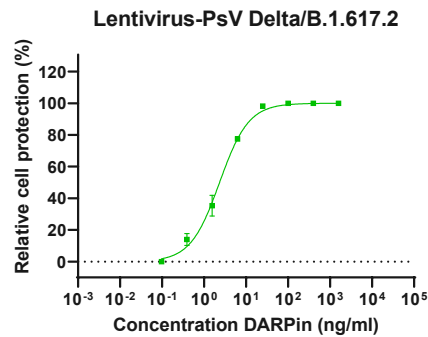
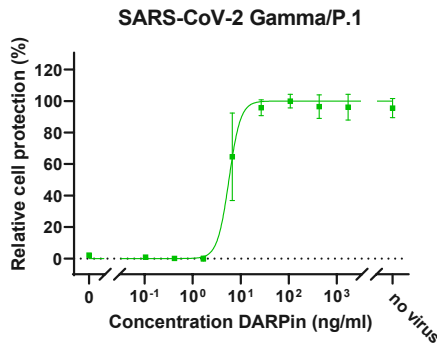
1058



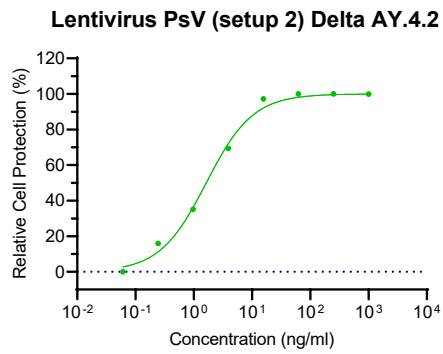
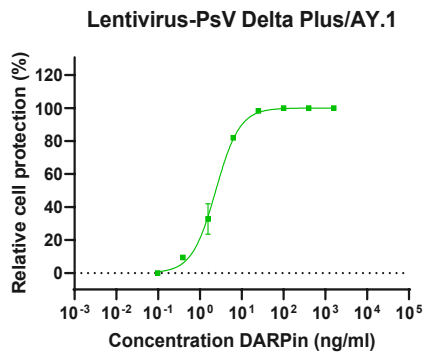
1059



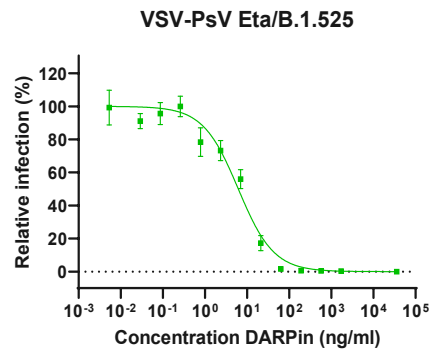
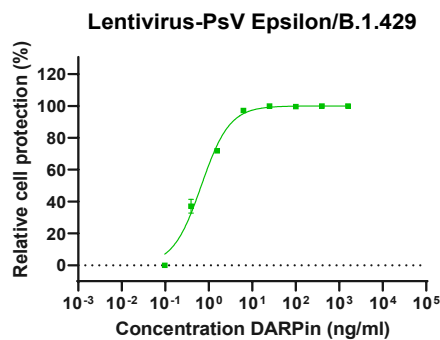
1060



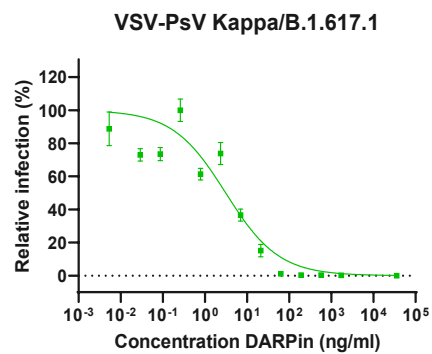
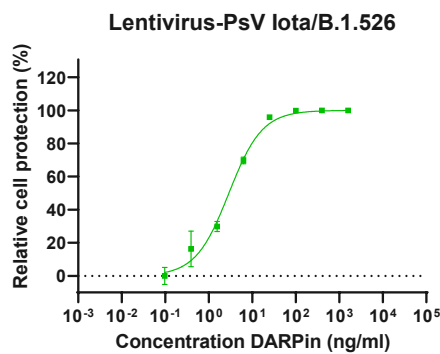
1061



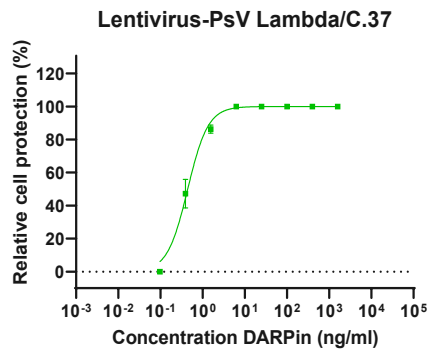
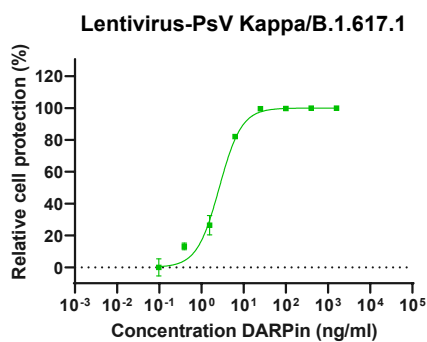
1062



1063

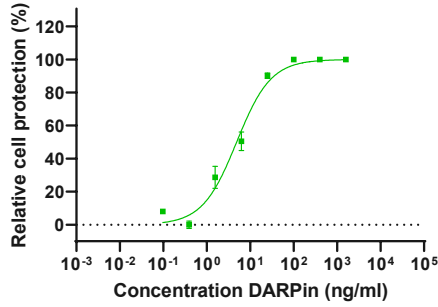


1064

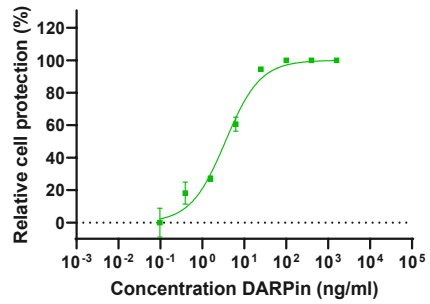


1065

Lentivirus-PsV Mu/B.1.621

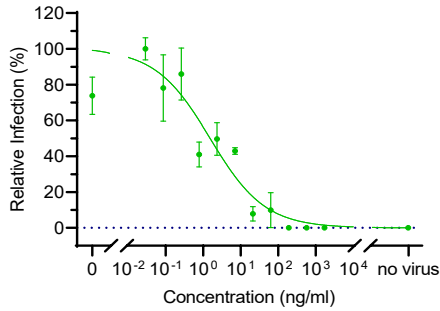


Lentivirus-PsV Omicron/B.1.1.529 BA.1

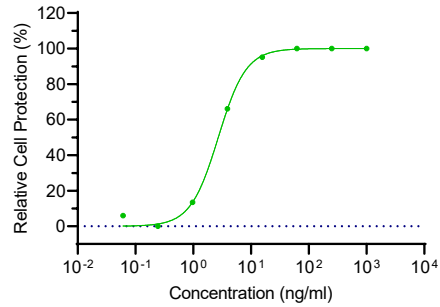


1066

VSV-PsV Omicron BA.2

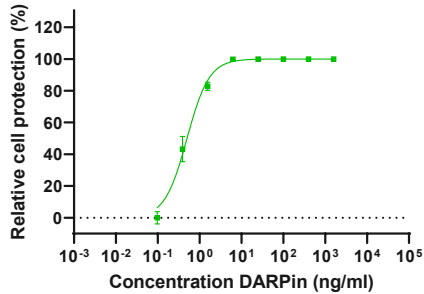


Lentivirus PsV (setup 2) Omicron BA.2

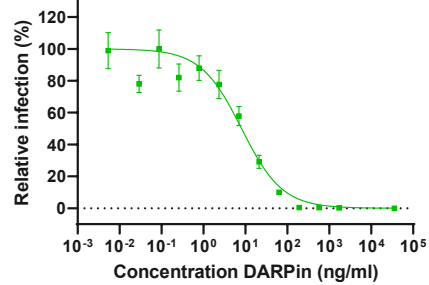


1067

Lentivirus-PsV A.23.1

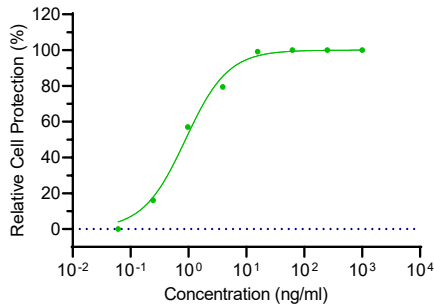


VSV-PsV B.1.618

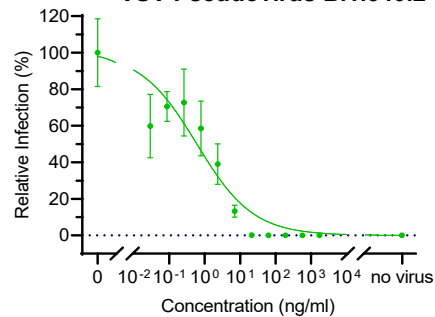


1068

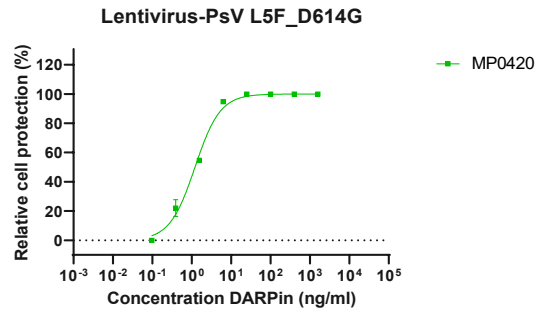
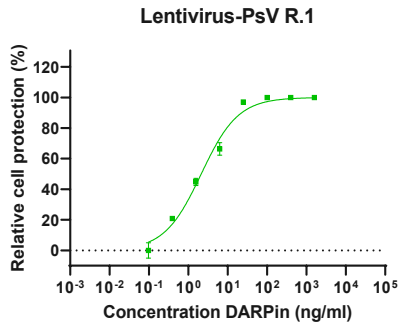
Lentivirus-PsV (setup 2) B.1.640.1



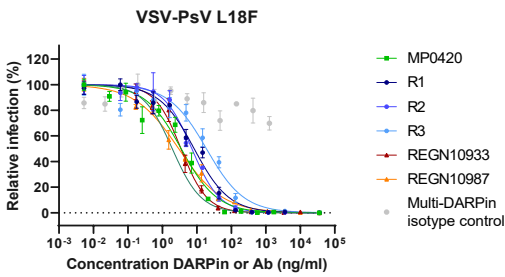
VSV Pseudovirus B.1.640.2



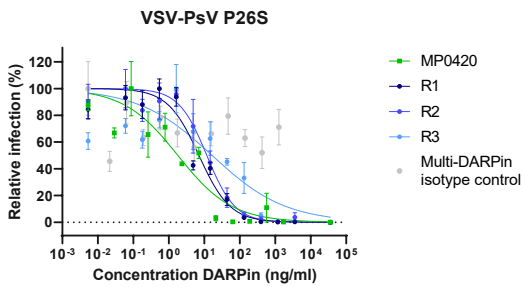
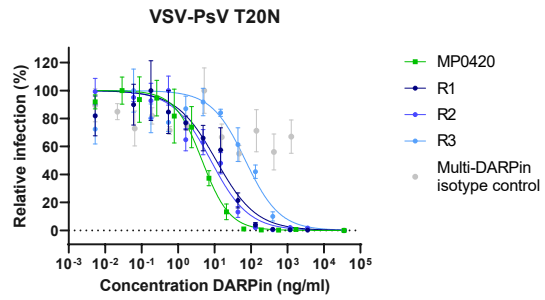
1069



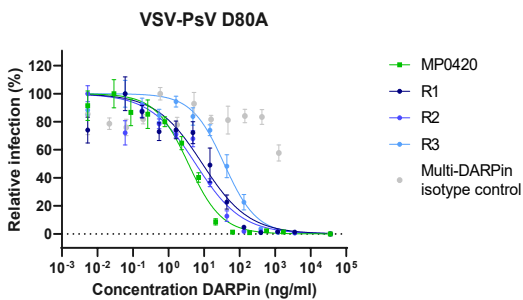
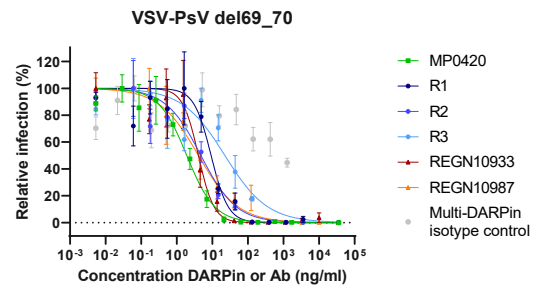
1070



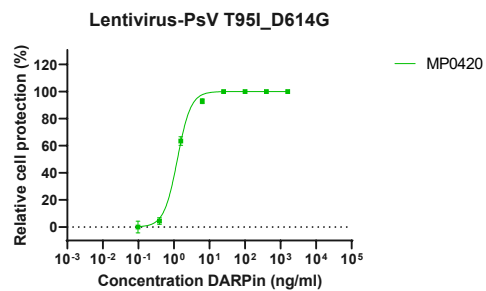
1071

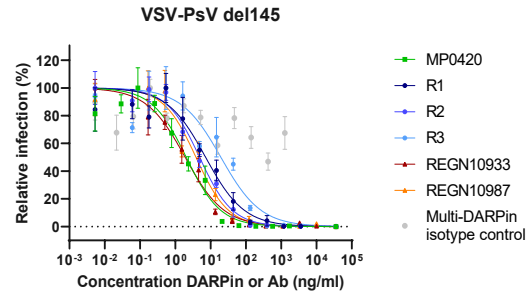
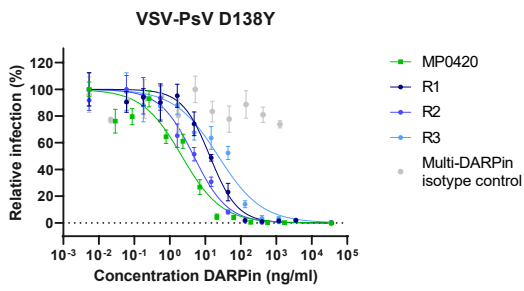


1072

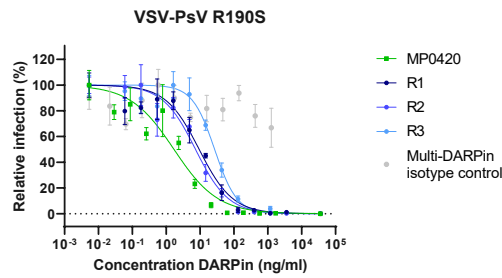
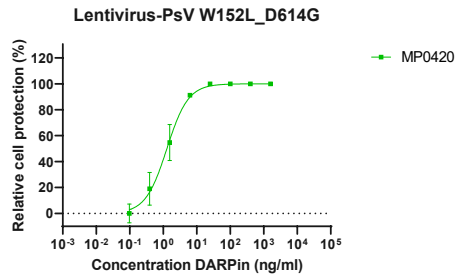


1073

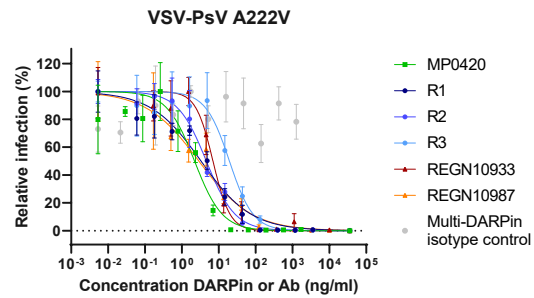
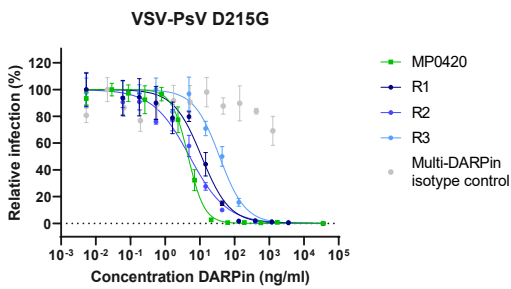




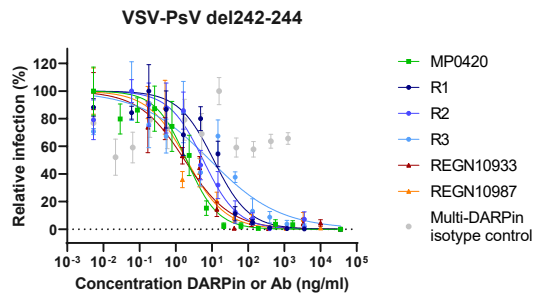
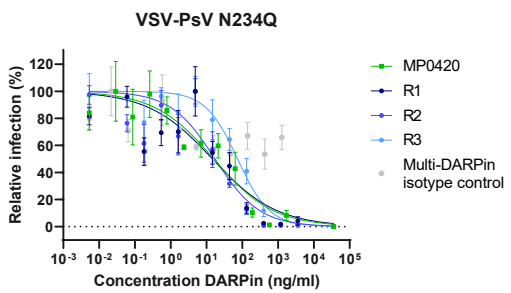
1074



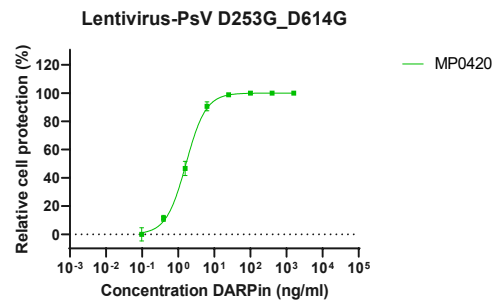
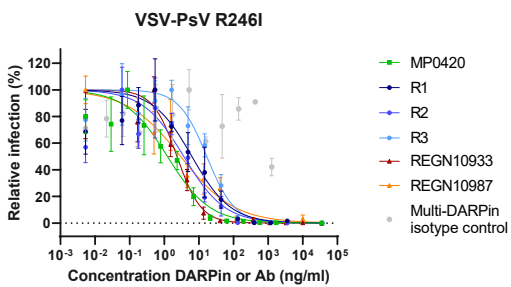
1075



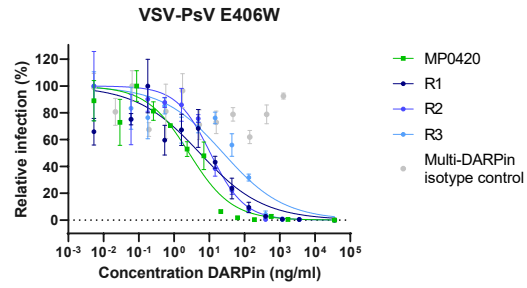
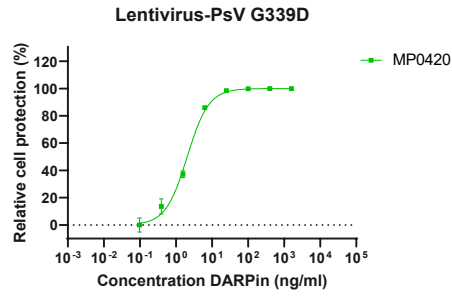
1076



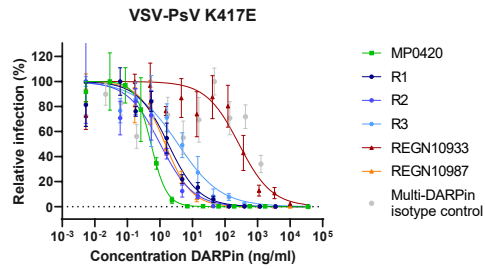
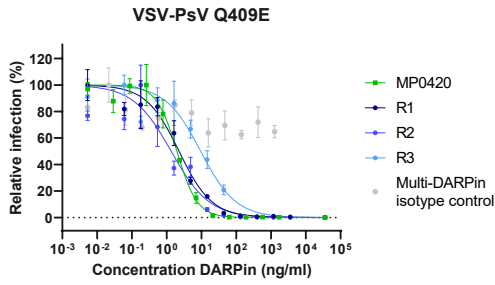
1077



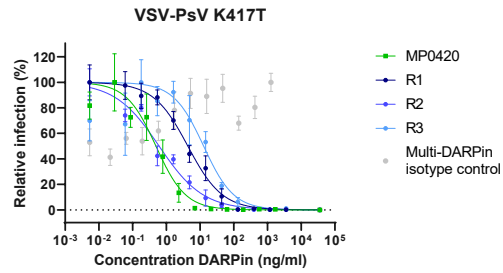
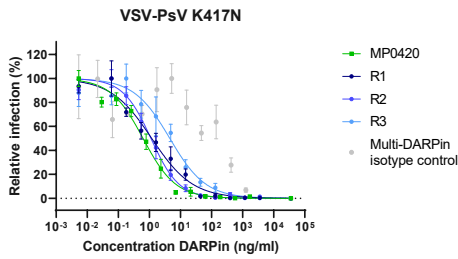
1078



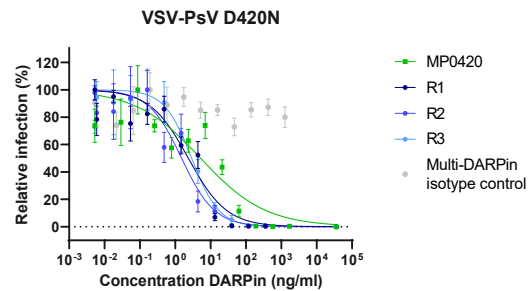
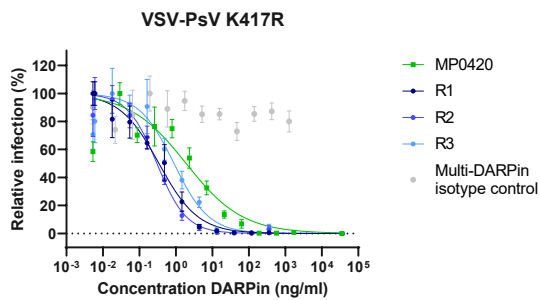
1079



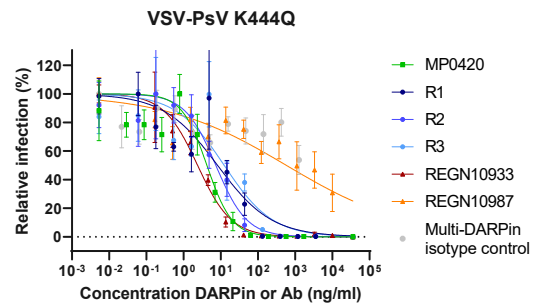
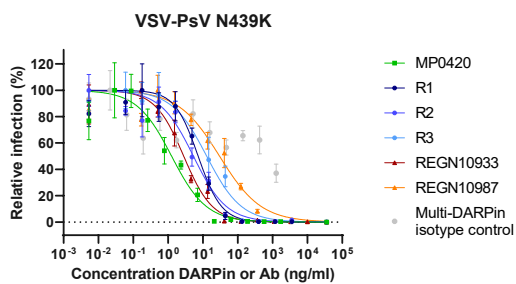
1080



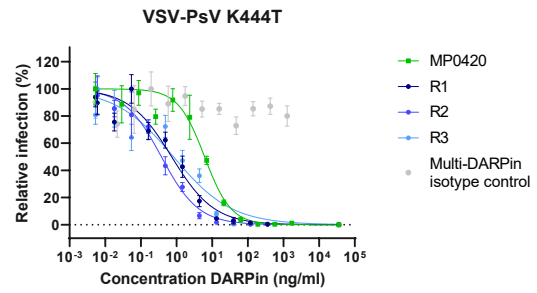
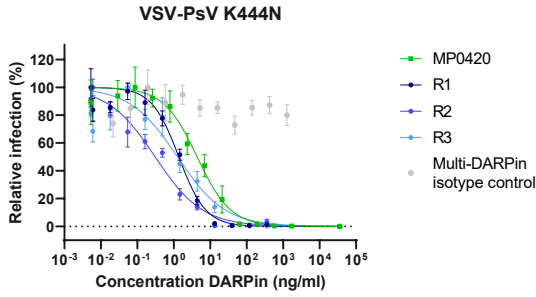
1081



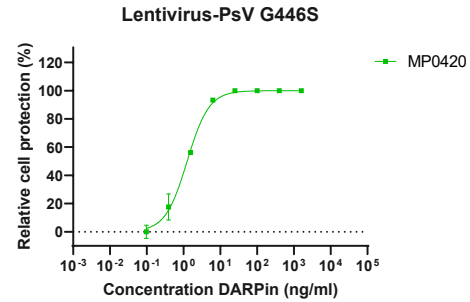
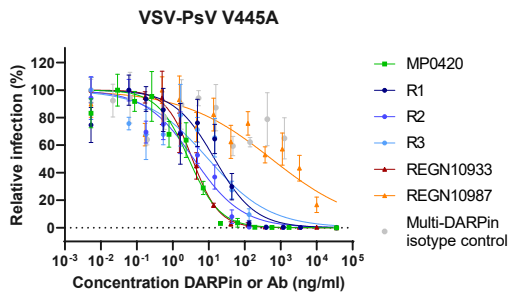
1082



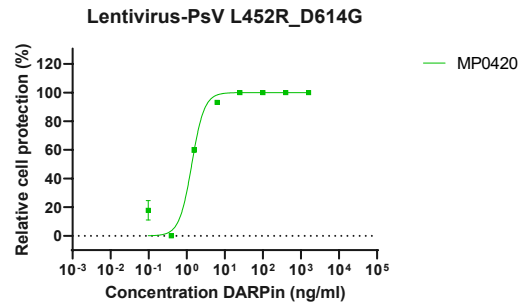
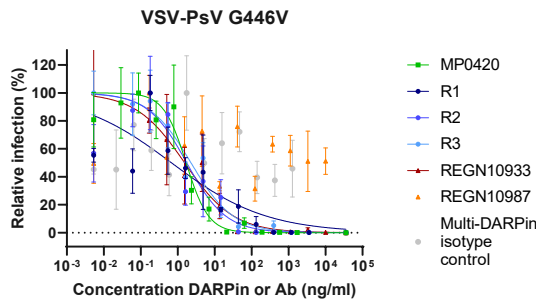
1083



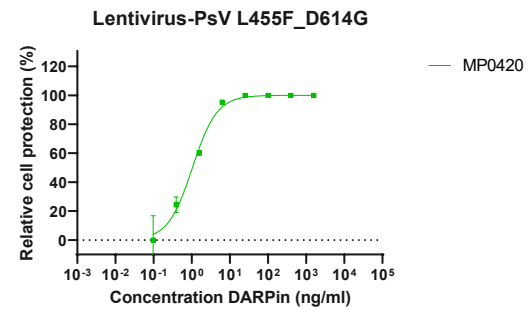
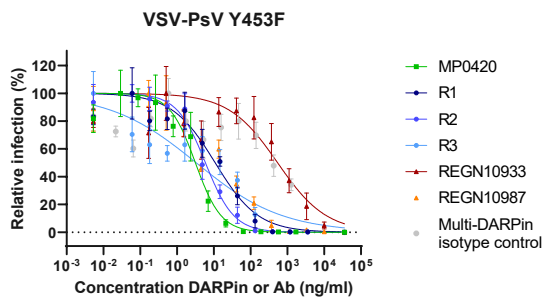
1084



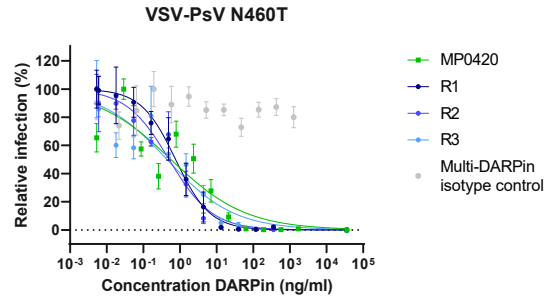
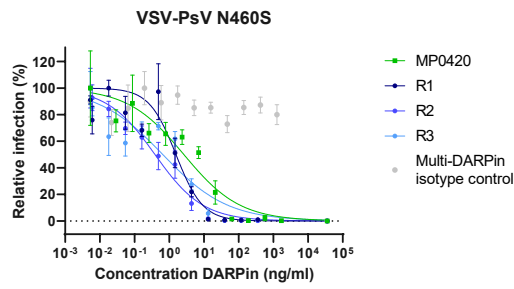
1085



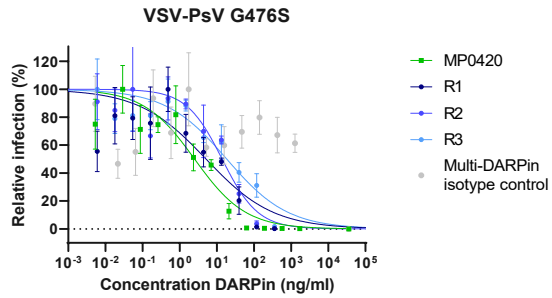
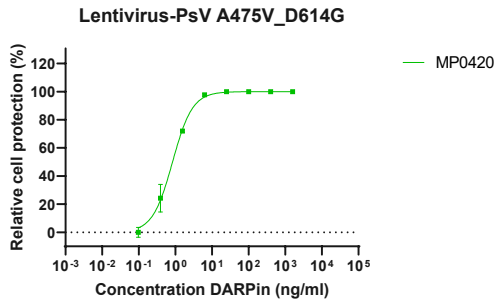
1086



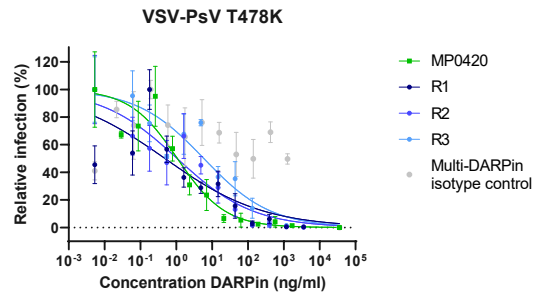
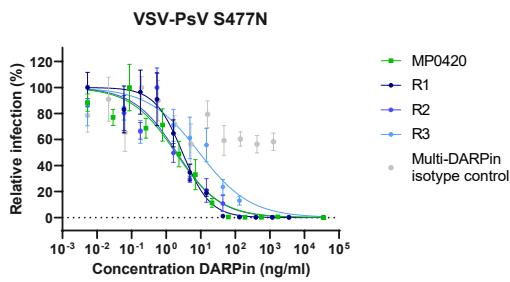
1087



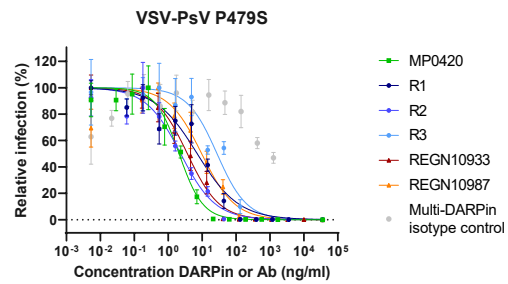
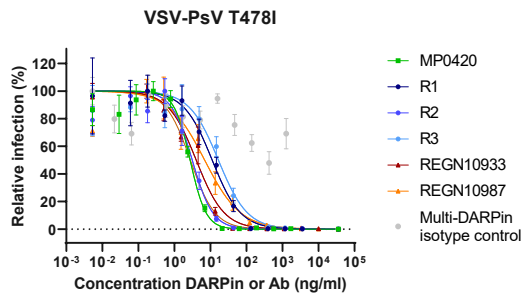
1088



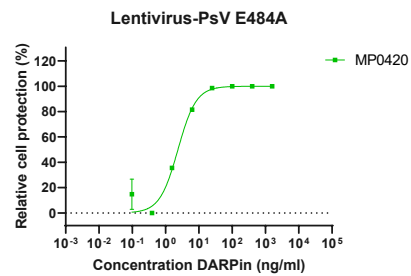
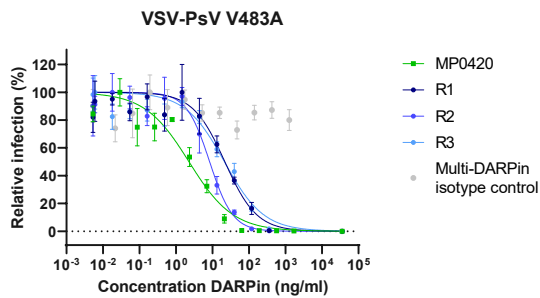
1089



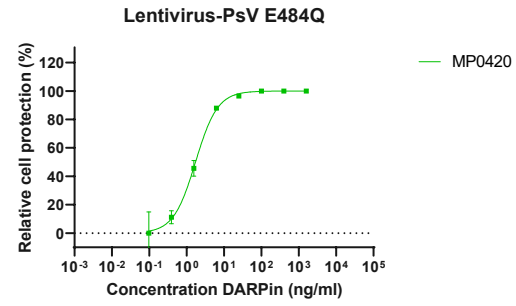
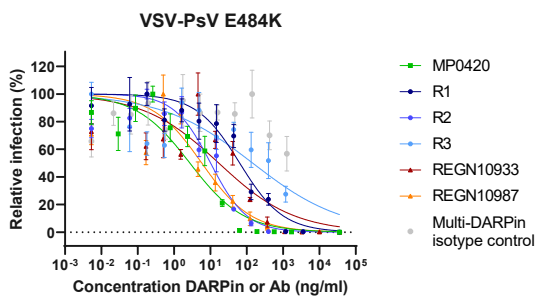
1090



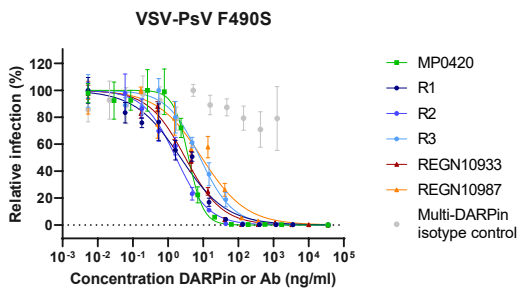
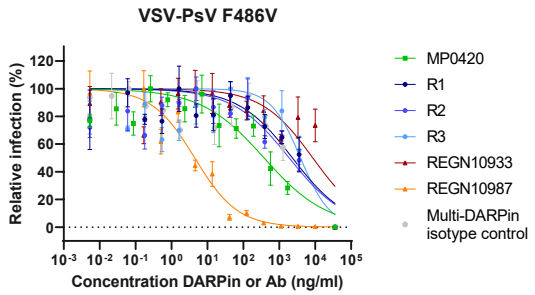
1091



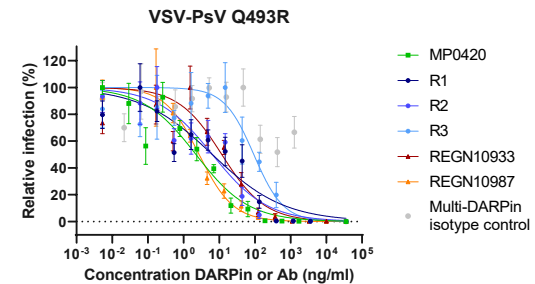
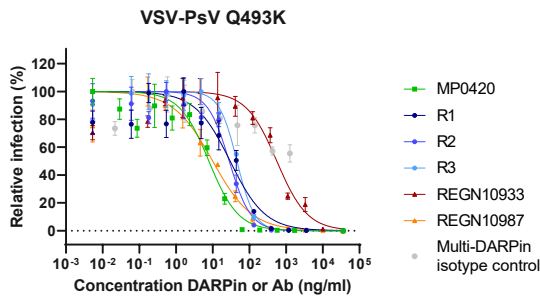
1092



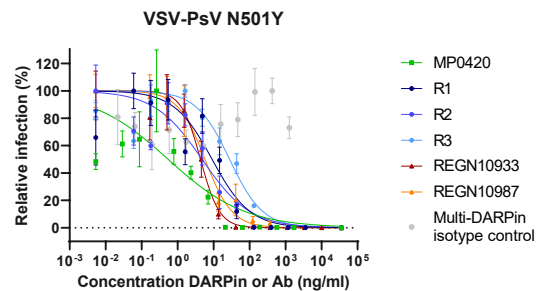
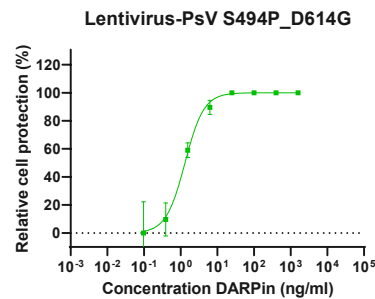
1093



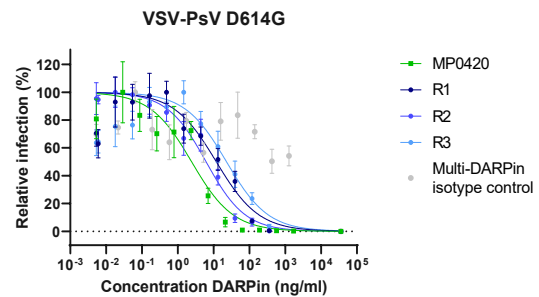
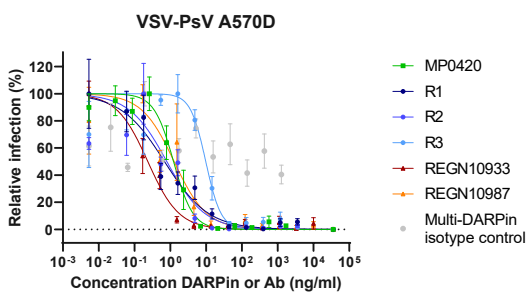
1094



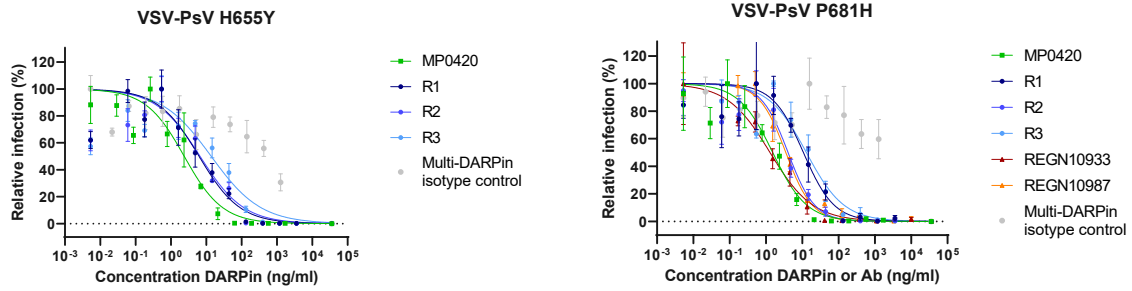
1095



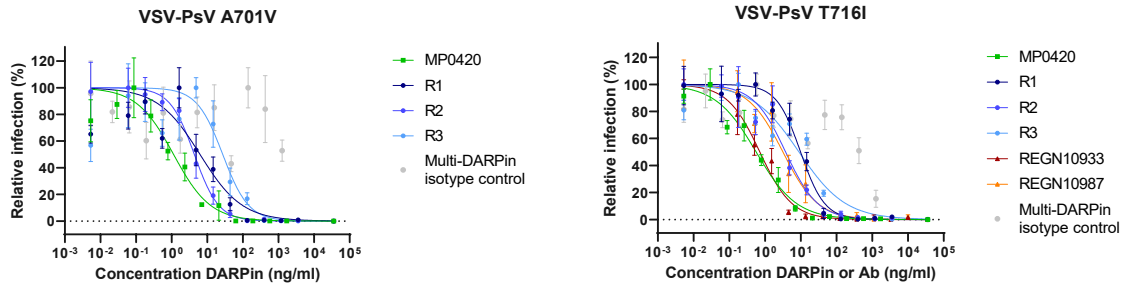
1096



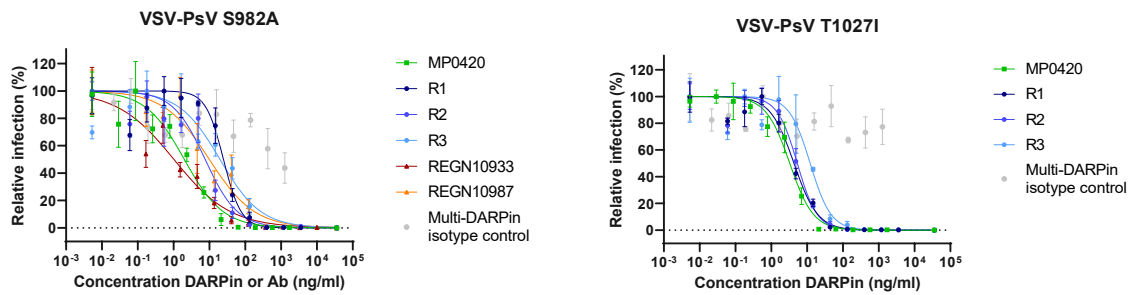
1097



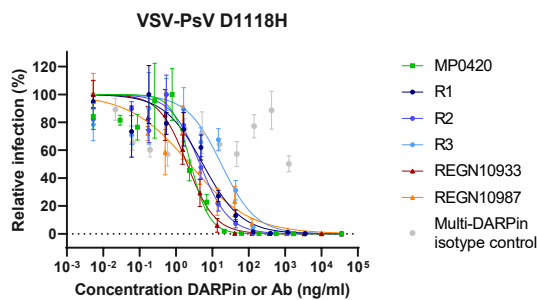
1098



1099



1100



1101

1102 **Supplementary Figure 4:** Titration curves for ensovibep (MP0420) and its RBD-binding
1103 domains (i.e. R1, R2 and R3), REGN10933 and REGN10987 to determine IC_{50} neutralization
1104 potencies on multiple spike mutants or only for ensovibep (MP0420) on the variants, which
1105 are summarized in Figure 2, Table 2 and Table 3. Reported is the mean \pm SEM (standard
1106 error of the mean).

SARS-CoV-2 Passage: # X

Therapeutic concentration [$\mu\text{g/mL}$]



Supernatant with SARS-CoV-2 of the well with the highest concentration showing $>20\%$ CPE was transferred to fresh Vero E6 cells in the presence of increasing concentration

SARS-CoV-2 Passage: # X + 1

Therapeutic concentration [$\mu\text{g/mL}$]



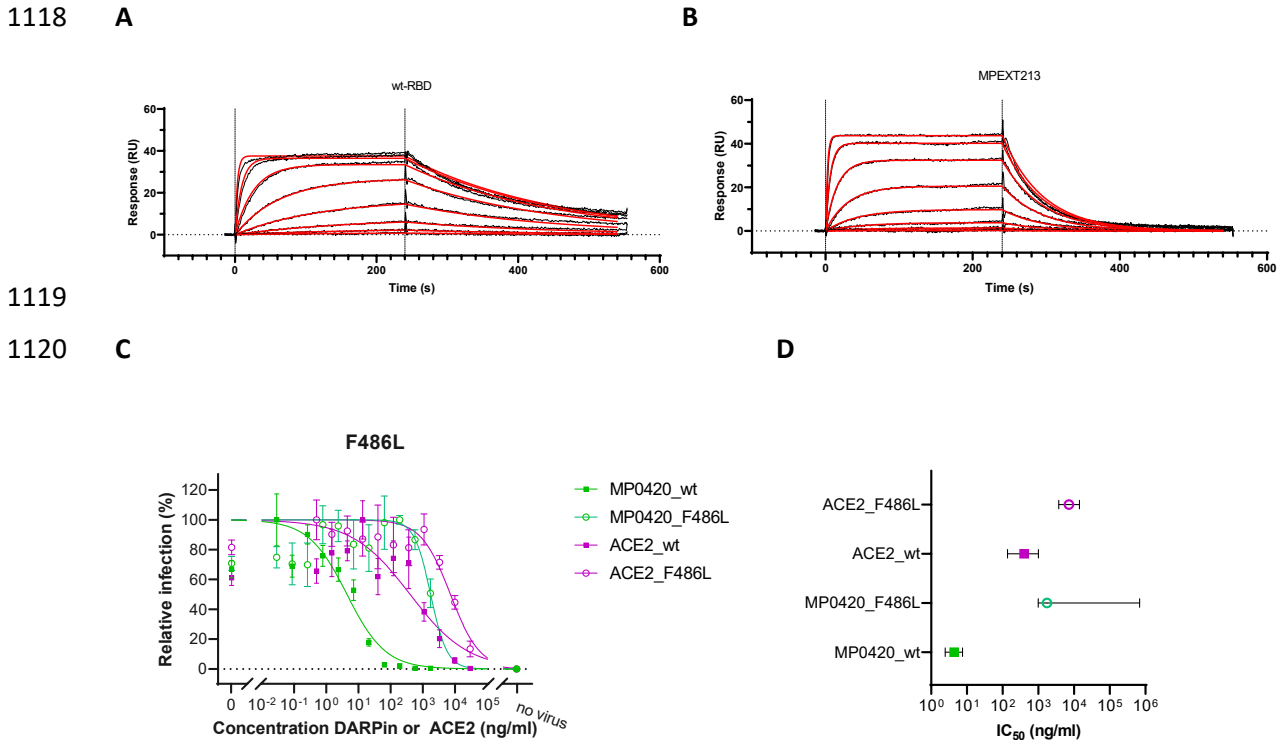
Passage # X + 2

CPE: Cytopathic effect; no CPE: no or minor ($<20\%$) cytopathic effect (by crystal violet staining)

1107

1108

1109 **Supplementary Figure 5: Overview of the experimental protocol for viral passaging:** A
1110 patient SARS-CoV-2 isolate from early 2020 (1.5×10^6 pfu) was incubated in presence of
1111 increasing concentrations of DARPin candidate or antibody for 4 days on Vero E6 cells and
1112 virus-induced cytopathic effects (CPE) were determined by microscopy. For each DARPin
1113 and antibody condition, cultures showing significant cytopathic effect ($\geq 20\%$) under the
1114 greatest selective pressure were selected and virus-containing supernatant collected to start
1115 a new culture passage on Vero E6 cells (bold circle), again under increasing concentrations
1116 of the corresponding DARPin candidate or antibody condition. Passaging of virus containing
1117 supernatant was continued in the same manner for a total of 4 passages.



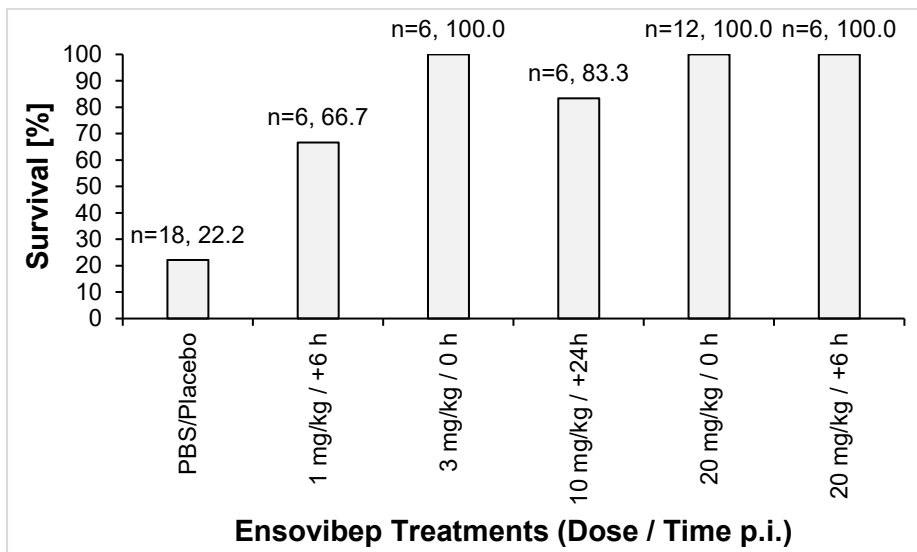
Supplementary Figure 6: Impact of mutation F486V/L in the RBD on ACE2 binding and neutralization potency of ACE2 or ensovibep (MP0420) in a pseudotype assay

A, B) Binding kinetics for different concentrations of ACE2 was determined by SPR (surface plasmon resonance) with A) immobilized wild type RBD and B) immobilized RBD with the substitution F486V (MPEXT213). Consequently, a drop in affinity was observed upon tested substitution from a KD of 7.8 nM for wild type (k_{on} : $6.0E+05$; k_{off} : $4.8E-03$) to a KD of 68.1 nM for F486V (k_{on} : $2.7E+05$; k_{off} : $1.8E-02$)

C, D) Titration of ACE2 and ensovibep (MP0420) for neutralization of a VSV pseudotype with SARS-CoV-2 wild type spike protein compared to F486L substituted in the spike protein. D) IC_{50} values with 95% confidential interval for the titrations shown in C) demonstrating the loss of potency for ACE2 and ensovibep due to the F486L substitution. In accordance with the SPR measurement, a >10-fold drop in neutralization potency was observed in a VSV pseudotype assay, when ACE2 was used as a competitor. In relation, a >100-fold drop in potency was observed for ensovibep based on the F486L substitution. Reported is the mean +/- SEM (standard error of the mean).

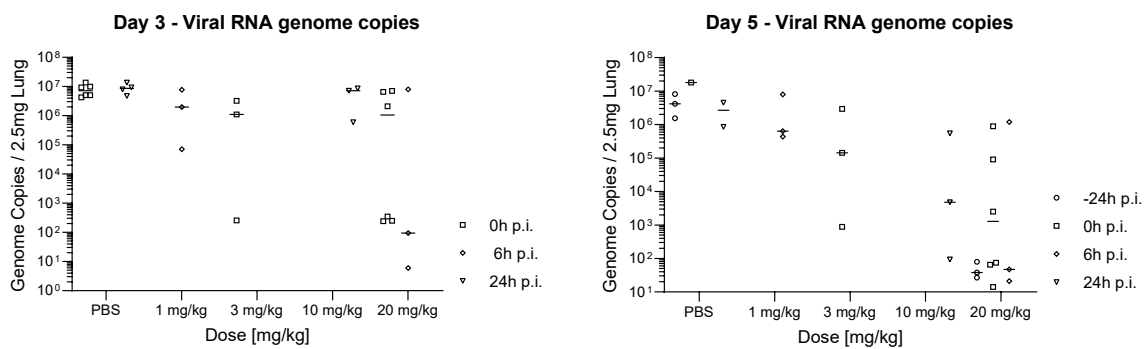
Shown experiments further underlines the reduction in binding of ACE2 to F486 substitutions and the importance of F486 for the SARS-CoV-2 virus to maintain the interaction with the human ACE2 receptor. So far, based on the global SARS-CoV-2 database sequences published in GISAID, mutations in position F486 (the core RBD-interaction residue for ensovibep) occur at very low frequencies.

1142 **A**

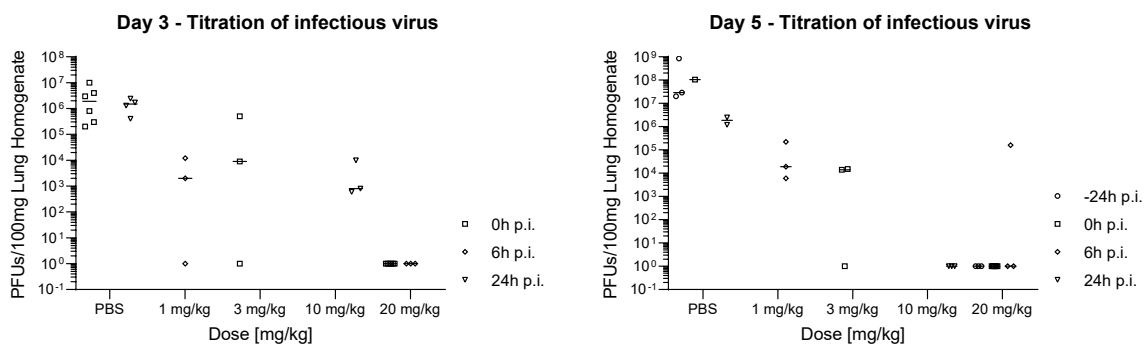


1143

1144 **B**



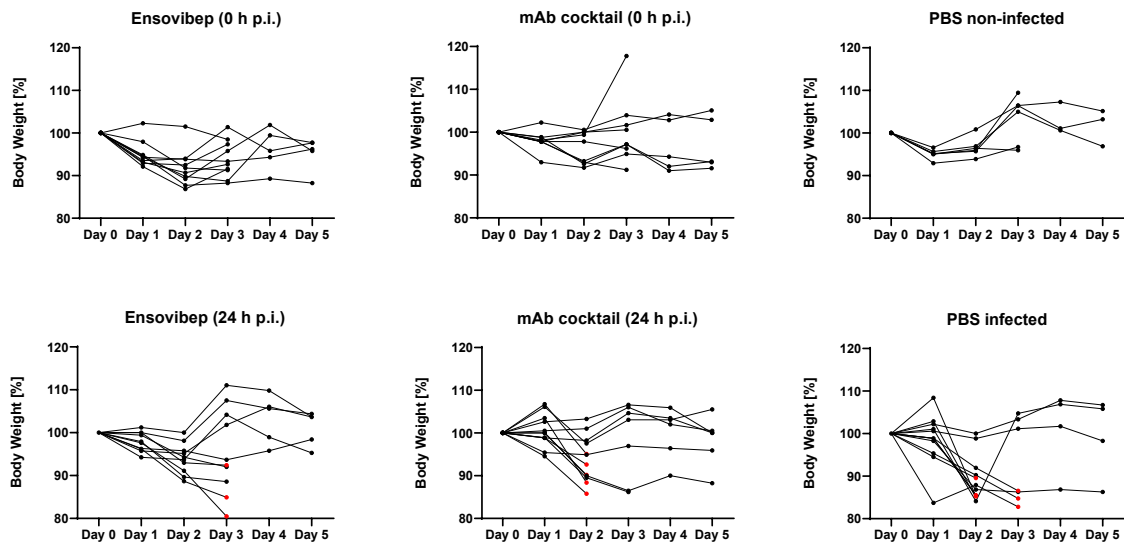
1146 **C**



1148 **Supplementary Figure 7: Summarized previous in vivo studies with Roborovski dwarf**
 1149 **hamster infected with WT SARS-CoV-2 and treated with ensovibep at various doses and**
 1150 **administration time points. A) Animal survival, end-point analysis, animals that had to be**
 1151 **euthanized according to score sheet criteria were considered non-survived, animals that**
 1152 **reached their respective defined take-out at day 3 or 5 post infection were considered**

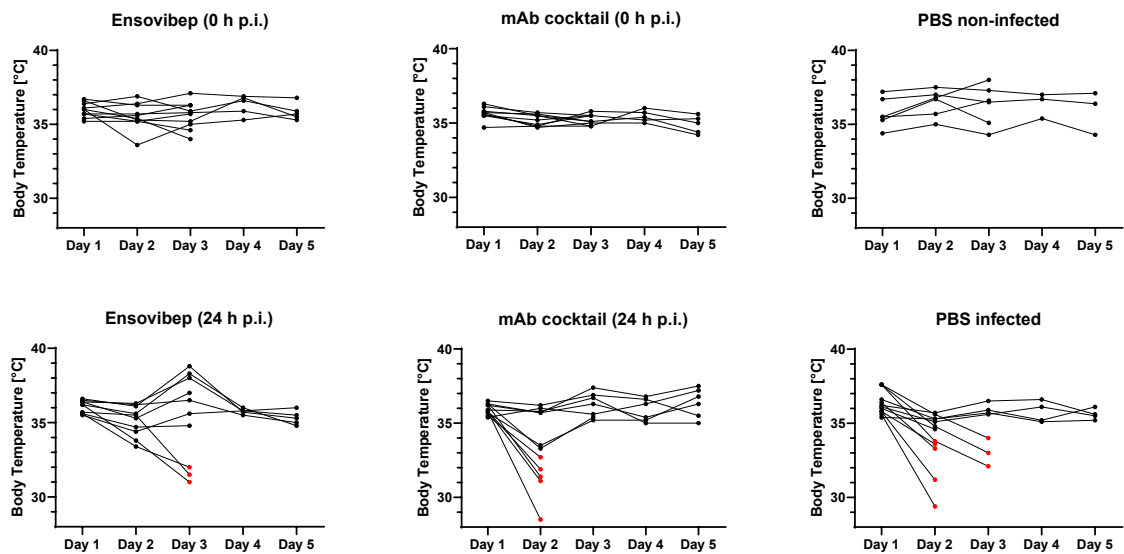
1153 *survived. B) qPCR analysis of virus gRNA copy numbers in oropharyngeal swabs and lung*
1154 *homogenates at day 3 or day 5 post infection C) Titration of replication competent virus from*
1155 *lung homogenates as plaque assay on Vero E6 cells at day 3 or day 5 post infection.*
1156 *Reported are the values of the individual animals and the median.*

1157 **A**



1158

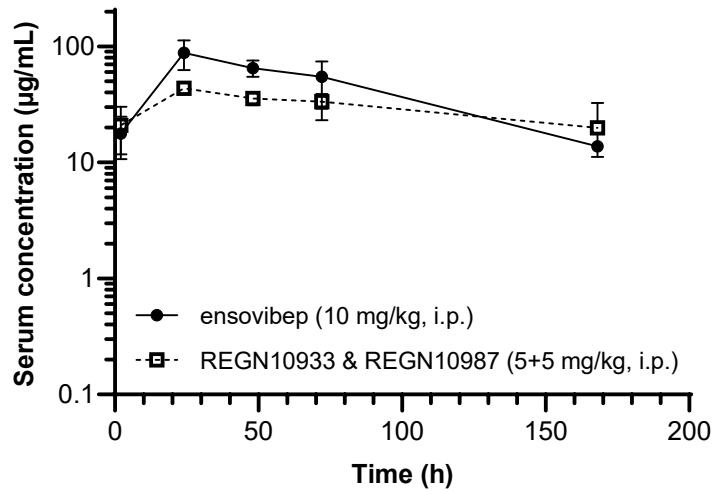
1159 **B**



1160

1161 **Supplementary Figure 8: Clinical Parameters of individuals over the course of**
1162 **infection, (mean +/- SD presented in Figure 5C) A) Body weight changes of individual**
1163 **hamsters B) Body temperatures of individual hamsters. Animals that had to be euthanized**
1164 **based on score sheet criteria are marked in red.**

Pharmacokinetics in Roborovski dwarf hamster following i.p. administration of 10 mg/kg



1165

1166 **Supplementary Figure 9:** Pharmacokinetics profiles of non-infected Roborovski dwarf
1167 hamsters injected i.p. with either 10 mg/kg of ensovibep or the cocktail of REGN10933 and
1168 REGN10987 at 5 mg/kg for each of the monoclonal antibodies. Three animals were
1169 sacrificed for determination of the therapeutic concentration in the serum of the terminal
1170 bleeds. Obvious outliers due to likely a failure of the intraperitoneal injection were removed
1171 from the evaluation. Reported is the mean \pm SEM (standard error of the mean).
1172 Pharmacokinetic parameters for ensovibep: $T_{1/2}$: 52.0 h; C_{max} : 87.8 $\mu\text{g/mL}$; T_{max} : 24 h.
1173 Pharmacokinetic parameters for the cocktail of REGN10933 and REGN10987: $T_{1/2}$: 139 h;
1174 C_{max} : 43.5 $\mu\text{g/mL}$; T_{max} : 24h.

1175 **Supplementary Table 1: Cryo-EM data collection and image processing information.**

Incubation time (seconds)	60	60	15
Magnification	75,000	75,000	92,000
Voltage ⁹²	300	300	200
Electron exposure (e-/Å²)	40	40	40
Defocus range (µm)	1.25-2.5	1.25-2.5	1.25-2.5
Pixel size (Å)	1.045	1.045	1.1
Symmetry imposed	C3	C1	N/A
Initial particle images (no.)	123,833	123,833	46,140
Final particle images (no.)	46,762	21,612	6,888
Map resolution (Å)	4.2	9.6	N/A
FSC threshold	0.143	0.143	N/A
Map resolution range (Å)	3.6-14.1	8.2-26	N/A

1176

1177 **Supplementary Table 2: In vitro protection against emerging SARS-CoV-2 variants for**
 1178 **ensovibep**

Variant	Substitutions / Deletions	Assay Type	Neutralizing IC ₅₀ [ng/mL]
References	Wuhan wild type	VSV pseudotype	1
	D614G background	Lentivirus pseudotype	1.1
	D614G background	Lentivirus pseudotype Setup 2	2.7
	French isolate: V367F; E990A	Authentic virus	1.3
Alpha / B.1.1.7	69-70 del, del145, N501Y, A570D, D614G, P681H, T716I, S982A, D1118H	VSV	1.7
	69-70 del, del145, E484K, N501Y, A570D, D614G, P681H, T716I, S982A, D1118H	VSV	3.2
	69-70 del, del145, N501Y, A570D, D614G, P681H, T716I, S982A, D1118H	Lentivirus pseudotype	0.9
	69-70 del, del145, S494P, N501Y, A570D, D614G, P681H, T716I, S982A, D1118H	Lentivirus pseudotype	0.8
	H69_V70del, Y145del, N501Y, A570D, D614G, P681H, T716I, S982A, D1118H	Authentic	1.3
Beta / B.1.351	D80A, D215G, E484K, N501Y, A701V	VSV	5.5
	L18F, D80A, D215G, Del242-244, R246I, K417N, E484K, N501Y, D614G, A701V	VSV	5
	L18F, D80A, D215G, Del242-244, K417N, E484K, N501Y, D614G, A701V	Lentivirus pseudotype	1.2
	L18F, D80A, D215G, L242_L244del, T302T, K417N, E484K, N501Y, D571D, D614G, A701V	Authentic	7.5
Gamma / P.1	L18F, T20N, P26S, D138Y, R190S, K417T, E484K, N501Y, D614G, H655Y, T1027I	VSV	1.2
	L18F, T20N, P26S, D138Y, R190S, K417T, E484K, N501Y, D614G, H655Y, T1027I, V1176F	Lentivirus pseudotype	0.7
	L18F, T20N, P26S, D138Y, R190S, K417T, E484K, N501Y, D614G, H655Y, T1027I, V1176F	Authentic	5.7
Delta/DeltaPlus / B.1.617.2	T19R, G142D, E156G, F157del, R158del, L452R, T478K, D614G, P681R, D950N	Lentivirus pseudotype	2.4
	T19R, T95I, G142D, E156G, F157del, R158del, W258L, K417N, L452R, T478K, D614G, P681R, D950N	Lentivirus pseudotype	2.6
	T19R, T95I, G142D, Y145H, E156G, F157-, R158-, A222V, L452R, T478K, D614G, P681R, D950N	Lentivirus pseudotype (Setup 2)	1.6
Epsilon/B.1.429	S13I, W152C, L452R, D614G	Lentivirus pseudotype	0.9
	S13I, P26S, W152C, L452R, D614G	Lentivirus pseudotype	0.5
Iota/B.1.526	L5F, T95I, D253G, E484K, D614G, A701V	Lentivirus pseudotype	3.0
Kappa / B.1.617.1	T95I, G142D, E154K, L452R, E484Q, D614G, P681R, Q1071H	Lentivirus pseudotype	2.0
	G142D, E154K, V382L, L452R, E484Q, D614G, P681R, Q1071H, D1153Y	Lentivirus pseudotype	1.9
Lambda / C37	G75V, T76I, R246del, S247-G252del, D253N, L452Q, F490S, D614G, T859N	Lentivirus pseudotype	0.4

Mu / B.1.621	T95I, Y144S, Y145N, R346K, E484K, N501Y, D614G, P681H, D950N	Lentivirus pseudotype	6.1
Omicron / B.1.1.529 / BA.1	A67V, Δ69-70, T95I, G142D, Δ143-145, Δ211, L212I, ins214EPE, G339D, S371L, S373P, S375F, K417N, N440K, G446S, S477N, T478K, E484A, Q493R, G496S, Q498R, N501Y, Y505H, T547K, D614G, H655Y, N679K, P681H, N764K, D796Y, N856K, N969K, L981F	VSV pseudotype	2.2
	A67V, Δ69-70, T95I, G142D, Δ143-145, Δ211, L212I, ins214EPE, G339D, S371L, S373P, S375F, K417N, N440K, G446S, S477N, T478K, E484A, Q493K, G496S, Q498R, N501Y, Y505H, T547K, D614G, H655Y, N679K, P681H, N764K, D796Y, N856K, Q954H, N969K, L981F	VSV pseudotype	2.1
	A67V, Δ69-70, T95I, G142D, Δ143-145, Δ211, L212I, ins214EPE, G339D, S371L, S373P, S375F, K417N, N440K, G446S, S477N, T478K, E484A, Q493R, G496S, Q498R, N501Y, Y505H, T547K, D614G, H655Y, N679K, P681H, N764K, D796Y, N856K, Q954H, N969K, L981F	Lentivirus pseudotype	3.6
Omicron / B.1.1.529 / BA.2	T19I, L24-, P25-, P26-, A27S, G142D, V213G, G339D, S371F, S373P, S375F, T376A, D405N, R408S, K417N, N440K, S477N, T478K, E484A, Q493R, Q498R, N501Y, Y505H, D614G, H655Y, N679K, P681H, N764K, D796Y, Q954H, N969K	Lentivirus pseudotype (Setup 2)	2.7
	T19I, L24-, P25-, P26-, A27S, G142D, V213G, G339D, S371F, S373P, S375F, T376A, D405N, R408S, K417N, N440K, S477N, T478K, E484A, Q493R, Q498R, N501Y, Y505H, D614G, H655Y, N679K, P681H, N764K, D796Y, Q954H, N969K	VSV pseudotype	1.5
B.1.640.1	P9L_E96Q_C136del_N137del_D138del_P139del_F140del_L141del_G142del_V143del_Y144del_R190S_I210T_R346S_N394S_Y449N_F490R_N501Y_D614G_P681H_T859N_D936H	Lentivirus pseudotype (Setup 2)	0.9
B.1.640.2	P9L, E96Q, delC136-Y144, R190S, D215H, R346S, N394S, Y449N, E484K, F490S, N501Y, D614G, P681H, T859N, D1139H	VSV pseudotype	0.6
R.1	W152L, E484K, D624G, G769V	Lentivirus pseudotype	2.4
A.23.1	F157L, V367F, Q613H, D614G, P681R	Lentivirus pseudotype	0.3

1180 **Supplementary Table 3:** In vitro protection against SARS-CoV-2 spike protein substitutions
 1181 or deletions for ensovibep.

Amino acid position	Substitution / deletion	Assay Type	Neutralizing IC ₅₀ [ng/mL]
L18	F	VSV	3.5
T20	N	VSV	4.6
P26	S	VSV	1.8
69-70	del	VSV	1.9
D80	A	VSV	3.6
T95	I	Lenti	0.9
D138	Y	VSV	2.2
145	del	VSV	2.1
W152	L	Lenti	1.2
R190	S	VSV	1.7
A222	V	VSV	2.2
N234	Q	VSV	16.2
242-244	del	VSV	2.0
G339	D	Lenti	2.0
E406	Q	Lenti	1.5
	W	VSV	2.7
Q409	E	VSV	2.0
K417	E	VSV	0.5
	N	VSV	0.6
	R	VSV	2.1
	T	VSV	0.5
D420	N	VSV	5.6
N439	K	VSV	1.3
K444	E	Lenti	0.8
	N	VSV	4.4
	Q	Lenti	1.3
	T	VSV	6.1
V445	A	Lenti	1.3
G446	V	VSV	1.7
	S	Lenti	1.3
N450	D	Lenti	0.9
L452	R	Lenti	0.4
Y453	F	VSV	3.2

L455	F	Lenti	1.1
N460	S	VSV	2.6
	T	VSV	0.6
A475	V	Lenti	0.9
G476	S	VSV	1.5
S477	N	VSV	1.9
T478	I	VSV	2.7
	K	Lenti	1.5
P479	S	VSV	2.1
V483	A	VSV	2.3
E484	A	Lenti	2.4
	K	VSV	2.7
	Q	Lenti	2.3
G485	D	VSV	28.5
F486	V	VSV	>100
	L	VSV	>100
F490	S	VSV	3.8
Q493	K	VSV	7.9
	R	VSV	2.2
S494	P	Lenti	1.3
N501	Y	VSV	0.6
A570	D	VSV	1.2
D614	G	VSV	2.4
H655	Y	VSV	2.4
P681	H	VSV	1.5
A701	V	VSV	1.1
T716	I	VSV	0.6
S982	A	VSV	2.0
T1027	I	VSV	3.3
D1118	H	VSV	2.6

1182

Supplementary Table 4: drug exposure levels in serum at day of euthanization.

Animals with drug exposure levels below 10% of the group average were removed from the study analysis (depicted in bold).

Ensovibep (10 mg/kg i.p.; 0 h p.i)			Ensovibep (10 mg/kg i.p.; 24 h p.i)		
#	Animal ID	Serum concentration [µg/mL]	#	Animal ID	Serum concentration [µg/mL]
1	DN5_1	86.9	1	DN5_25	17.0
2	DN5_2	2.7	2	DN5_26	1.8
3	DN5_3	169.7	3	DN5_27	39.1
4	DN5_4	44.5	4	DN5_28	N/A
5	DN5_5	92.9	5	DN5_29	48.0
6	DN5_6	39.2	6	DN5_30	5.7
7	DN5_7	1.5	7	DN5_31	225.1
8	DN5_8	109.4	8	DN5_32	27.3
9	DN5_9	51.8	9	DN5_33	66.6
10	DN5_10	127.9	10	DN5_34	109.5
11	DN5_11	70.2	11	DN5_35	128.4
12	DN5_12	38.6	12	DN5_36	78.3

REGN10933 & REGN10987 (5 + 5 mg/kg i.p.; 0 h p.i)			REGN10933 & REGN10987 (5 + 5 mg/kg i.p.; 24 h p.i)		
#	Animal ID	Serum concentration [µg/mL]	#	Animal ID	Serum concentration [µg/mL]
1	DN5_13	29.0	1	DN5_37	72.0
2	DN5_14	0.3	2	DN5_38	60.9
3	DN5_15	26.5	3	DN5_39	42.8
4	DN5_16	1.1	4	DN5_40	32.6
5	DN5_17	34.0	5	DN5_41	46.7
6	DN5_18	1.4	6	DN5_42	41.9
7	DN5_19	41.9	7	DN5_43	43.7
8	DN5_20	30.3	8	DN5_44	45.3
9	DN5_21	43.5	9	DN5_45	46.1
10	DN5_22	38.0	10	DN5_46	61.9
11	DN5_23	28.1	11	DN5_47	37.2
12	DN5_24	32.7	12	DN5_48	41.8

N/A: Not available due to low amount of serum extracted from terminal bleeds

Bold: animals removed from the study data due to low therapeutic exposure

Red: animals euthanized at 2 dpi

Blue: animals euthanized at 3 dpi

Green: animals euthanized at 5dpi

1183

1184

Supplementary Table 5: Identification of escape mutations by deep sequencing of SARS-CoV-2 Alpha variant B.1.1.7 in animals at day 5 p.i., which indicated remaining viral titers. As a control, three non-treated animals were also deep sequenced. Deep Sequencing was performed from either swab (S) or lung (L) extracted RNA.

Treatment group	Animal identifier	Throat swab (S) or lung homogenate (L)	Identified spike protein amino acid substitution	Potential Impact
Ensovibep 0 dpi	DN5_2	L	-	-
		S	-	-
	DN5_4	L	-	-
		S	K1034M	Neutral / outside ensovibep epitope
antibody cocktail 0 dpi	DN5_15	L	-	-
		S	-	-
	DN5_24	L	-	-
		S	-	-
Ensovibep 1 dpi	DN5_30	L	-	-
		S	-	-
Placebo group	DN5_50	L	-	-
		S	R671L	At furin cleavage site
	DN5_52	L	-	-
		S	R671L	At furin cleavage site
	DN5_53	L	-	-
		S	-	-

1185

1186

1187 **Supplementary Table 6: Histopathology data table**

Stimulus	Necropsy day post infection	Inflammation Parameters				Bronchi			Alveoli			Vasculature			
		% affected	Degree of inflammation	Lymphocytes	Macrophages	Neutrophils	Broncho-epithelial necroses	Bronchitis	Broncho-epithelial hyperplasia	Alveolar epithelium necroses	Alveolar edema	Typ. II Hyperplasia	Perivascular lymphocyte cuffs	Perivascular edema	Endoheilitis
PBS / non-infected	3	20	1	0	1	1	0	1	0	0	1	0	0	1	0
PBS / non-infected	3	<5	0	0	0	0	0	0	0	0	0	0	0	0	0
PBS / non-infected	5	<5	0	0	0	0	0	0	0	0	0	0	0	0	0
PBS / non-infected	5	10	1	1	1	1	0	0	0	0	0	0	0	0	0
PBS / non-infected - Excluded from analysis	3	50	2	2	2	2	0	0	1	1	2	0	3	2	1
PBS / Infected	2	80	1	1	1	1	1	1	1	1	0	0	0	3	1
PBS / Infected	2	80	3	1	3	1	1	1	1	1	2	0	0	2	0
PBS / Infected	2	80	3	1	2	3	1	2	1	2	0	0	0	2	2
PBS / Infected	3	70	1	1	1	1	1	0	1	2	0	0	0	2	2
PBS / Infected	3	70	3	1	3	3	1	0	2	2	1	0	2	2	2
PBS / Infected	3	20	1	1	1	1	1	0	1	2	0	0	1	1	1
PBS / Infected	5	40	3	2	2	0	0	2	1	2	0	0	2	1	1
PBS / Infected	5	60	3	2	2	2	0	2	0	2	1	2	2	1	3
PBS / Infected	5	50	2	1	1	1	0	2	0	0	0	2	2	1	0
PBS / Infected	5	30	1	2	1	1	0	1	0	0	1	1	1	1	3
PBS / Infected - excluded from analysis	2	100	0	0	0	0	0	0	0	0	0	0	0	0	0
ensowbep (0mg/kg (dpr))	3	50	2	1	2	1	1	1	1	1	1	2	4	1	0
ensowbep (0mg/kg (dpr))	3	40	3	1	2	3	1	2	1	2	0	0	1	1	0
ensowbep (0mg/kg (dpr))	3	40	3	1	2	2	1	3	1	1	2	1	1	0	0
ensowbep (0mg/kg (dpr))	3	5	1	0	0	1	1	0	0	0	0	0	0	0	0
ensowbep (0mg/kg (dpr))	3	5	4	0	0	0	0	0	0	0	0	0	0	0	0
ensowbep (0mg/kg (dpr))	5	90	3	1	3	3	1	2	2	1	3	2	2	1	0
ensowbep (0mg/kg (dpr))	5	50	2	1	2	1	1	2	0	1	1	1	4	0	0
ensowbep (0mg/kg (dpr))	5	15	1	1	1	1	1	1	0	1	1	2	1	1	0
ensowbep (0mg/kg (dpr))	5	50	3	1	2	1	2	2	0	1	2	1	2	1	0
ensowbep (0mg/kg (dpr))	5	<5	0	0	0	0	0	0	0	0	0	0	0	0	0
ensowbep (0mg/kg (dpr))	5	100	1	1	1	1	1	0	0	0	3	2	0	3	0
ensowbep (0mg/kg (dpr))	3	20	1	1	1	1	1	1	1	1	1	1	0	0	1
ensowbep (0mg/kg (dpr))	3	<5	0	0	0	0	0	0	0	0	0	0	0	0	1
ensowbep (0mg/kg (dpr))	3	100	1	1	1	1	1	1	2	2	1	1	0	3	2
ensowbep (0mg/kg (dpr))	3	80	2	1	2	2	1	2	0	1	1	0	0	2	2
ensowbep (0mg/kg (dpr))	5	<5	0	0	0	0	0	0	0	0	0	0	0	0	0
ensowbep (0mg/kg (dpr))	5	20	1	1	1	1	1	1	1	1	1	1	1	1	0
ensowbep (0mg/kg (dpr))	5	100	2	1	2	2	1	3	1	3	0	0	1	1	0
ensowbep (0mg/kg (dpr))	5	80	2	1	2	2	1	2	1	2	2	1	1	0	0
ensowbep (0mg/kg (dpr))	5	<5	1	0	1	1	0	0	0	0	1	0	0	0	0
ensowbep (0mg/kg (dpr))	3	70	3	2	2	2	1	2	1	1	1	2	1	1	1
mAb cocktail (0mg/kg (dpr))	3	90	2	1	2	1	1	1	1	1	1	1	1	1	0
mAb cocktail (0mg/kg (dpr))	3	30	1	1	1	1	1	1	1	1	1	1	1	1	0
mAb cocktail (0mg/kg (dpr))	3	50	2	1	2	1	0	2	2	1	0	0	1	1	0
mAb cocktail (0mg/kg (dpr))	5	<5	0	0	0	0	0	0	0	0	0	0	0	0	0
mAb cocktail (0mg/kg (dpr))	5	50	3	1	3	3	1	3	1	1	2	1	1	1	1
mAb cocktail (0mg/kg (dpr))	5	10	1	1	1	1	1	1	1	1	1	1	1	1	0
mAb cocktail (0mg/kg (dpr))	5	<5	1	0	1	1	0	0	0	0	0	0	0	0	0
mAb cocktail (0mg/kg (dpr))	5	30	1	1	1	1	1	1	1	1	1	1	1	1	0
mAb cocktail (0mg/kg (dpr))	2	50	3	3	3	3	1	3	1	2	3	0	0	1	1
mAb cocktail (0mg/kg (dpr))	2	80	3	1	3	1	1	0	1	1	1	0	0	2	1
mAb cocktail (0mg/kg (dpr))	2	90	3	0	3	3	1	3	1	1	1	0	2	3	2
mAb cocktail (0mg/kg (dpr))	2	90	3	0	3	3	1	2	1	3	0	0	2	3	0
mAb cocktail (0mg/kg (dpr))	2	20	2	0	2	1	1	1	1	1	1	0	0	2	0
mAb cocktail (0mg/kg (dpr))	3	60	3	0	3	3	1	2	0	3	1	1	1	2	1
mAb cocktail (0mg/kg (dpr))	5	40	1	1	1	1	0	1	0	1	3	0	0	1	0
mAb cocktail (0mg/kg (dpr))	5	90	1	1	1	1	0	1	0	1	3	0	0	1	0
mAb cocktail (0mg/kg (dpr))	5	10	1	1	1	1	0	0	0	0	1	3	0	1	0
mAb cocktail (0mg/kg (dpr))	5	10	1	1	1	1	0	0	0	0	1	3	0	1	0
mAb cocktail (0mg/kg (dpr))	5	10	1	1	1	1	0	0	0	0	1	3	0	1	0
mAb cocktail (0mg/kg (dpr))	5	10	1	1	1	1	0	0	0	0	1	3	0	1	0
mAb cocktail (0mg/kg (dpr))	5	<5	1	1	1	1	0	0	0	0	0	0	0	1	0

1189 References

- 1190 1 Zhou, P. *et al.* A pneumonia outbreak associated with a new coronavirus of probable bat origin. *Nature*
1191 **579**, 270-273, doi:10.1038/s41586-020-2012-7 (2020).
- 1192 2 Shang, J. *et al.* Structural basis of receptor recognition by SARS-CoV-2. *Nature* **581**, 221-224,
1193 doi:10.1038/s41586-020-2179-y (2020).
- 1194 3 Tortorici, M. A. & Veesler, D. Structural insights into coronavirus entry. *Adv Virus Res* **105**, 93-116,
1195 doi:10.1016/bs.aivir.2019.08.002 (2019).
- 1196 4 Letko, M., Marzi, A. & Munster, V. Functional assessment of cell entry and receptor usage for SARS-
1197 CoV-2 and other lineage B betacoronaviruses. *Nat Microbiol* **5**, 562-569, doi:10.1038/s41564-020-0688-
1198 y (2020).
- 1199 5 Walls, A. C. *et al.* Structure, Function, and Antigenicity of the SARS-CoV-2 Spike Glycoprotein. *Cell* **181**,
1200 281-292 e286, doi:10.1016/j.cell.2020.02.058 (2020).
- 1201 6 Walls, A. C. *et al.* Cryo-electron microscopy structure of a coronavirus spike glycoprotein trimer. *Nature*
1202 **531**, 114-117, doi:10.1038/nature16988 (2016).
- 1203 7 Walls, A. C. *et al.* Tectonic conformational changes of a coronavirus spike glycoprotein promote
1204 membrane fusion. *Proc Natl Acad Sci U S A* **114**, 11157-11162, doi:10.1073/pnas.1708727114 (2017).
- 1205 8 Hoffmann, M. *et al.* SARS-CoV-2 Cell Entry Depends on ACE2 and TMPRSS2 and Is Blocked by a Clinically
1206 Proven Protease Inhibitor. *Cell* **181**, 271-280 e278, doi:10.1016/j.cell.2020.02.052 (2020).
- 1207 9 Jun Zhang¹, Yongfei Cai^{1,2†}, Tianshu Xiao^{1,2}, Jianming Lu³, Hanqin Peng¹, Sarah M. Sterling^{4,5},
1208 Richard M. Walsh Jr.^{4,5}, Sophia Rits-Volloch¹, Haisun Zhu⁶, Alec N. Woosley⁶, Wei Yang⁶, Piotr
1209 Sliz^{1,2,5}, Bing Chen^{1,2*}. Structural impact on SARS SoV-2 spike protein by D614G substitution. *Science*
1210 (2021).
- 1211 10 Garcia-Beltran, W. F. *et al.* Multiple SARS-CoV-2 variants escape neutralization by vaccine-induced
1212 humoral immunity. *Cell* **184**, 2372-2383 e2379, doi:10.1016/j.cell.2021.03.013 (2021).
- 1213 11 Greaney, A. J. *et al.* Complete Mapping of Mutations to the SARS-CoV-2 Spike Receptor-Binding Domain
1214 that Escape Antibody Recognition. *Cell host & microbe* **29**, 44-57.e49, doi:10.1016/j.chom.2020.11.007
1215 (2021).
- 1216 12 Lusvardi, S. *et al.* Key substitutions in the spike protein of SARS-CoV-2 variants can predict resistance
1217 to monoclonal antibodies, but other substitutions can modify the effects. *bioRxiv*,
1218 2021.2007.2016.452748, doi:10.1101/2021.07.16.452748 (2021).
- 1219 13 Starr, T. N. *et al.* Deep Mutational Scanning of SARS-CoV-2 Receptor Binding Domain Reveals
1220 Constraints on Folding and ACE2 Binding. *Cell* **182**, 1295-1310.e1220, doi:10.1016/j.cell.2020.08.012
1221 (2020).
- 1222 14 Thomson, E. C. *et al.* Circulating SARS-CoV-2 spike N439K variants maintain fitness while evading
1223 antibody-mediated immunity. *Cell* **184**, 1171-1187.e1120, doi:10.1016/j.cell.2021.01.037 (2021).
- 1224 15 Wang, P. *et al.* Increased Resistance of SARS-CoV-2 Variants B.1.351 and B.1.1.7 to Antibody
1225 Neutralization. *bioRxiv*, doi:10.1101/2021.01.25.428137 (2021).
- 1226 16 Yi, C. *et al.* Key residues of the receptor binding motif in the spike protein of SARS-CoV-2 that interact
1227 with ACE2 and neutralizing antibodies. *Cell Mol Immunol* **17**, 621-630, doi:10.1038/s41423-020-0458-z
1228 (2020).
- 1229 17 Liu, Z. *et al.* Identification of SARS-CoV-2 spike mutations that attenuate monoclonal and serum
1230 antibody neutralization. *Cell host & microbe* **29**, 477-488.e474, doi:10.1016/j.chom.2021.01.014 (2021).
- 1231 18 Zhou, D. *et al.* Evidence of escape of SARS-CoV-2 variant B.1.351 from natural and vaccine-induced sera.
1232 *Cell* **184**, 2348-2361.e2346, doi:https://doi.org/10.1016/j.cell.2021.02.037 (2021).
- 1233 19 Gobeil, S. M.-C. *et al.* Effect of natural mutations of SARS-CoV-2 on spike structure, conformation, and
1234 antigenicity. *Science* **373**, eabi6226, doi:doi:10.1126/science.abi6226 (2021).
- 1235 20 Tegally, H. *et al.* Emergence and rapid spread of a new severe acute respiratory syndrome-related
1236 coronavirus 2 (SARS-CoV-2) lineage with multiple spike mutations in South Africa. *medRxiv*,
1237 doi:10.1101/2020.12.21.20248640 (2020).
- 1238 21 Voloch, C. M. *et al.* Novel circulating lineage of SARS-CoV-2 in the state of Rio de Janeiro Brazil
1239 originated from B.1.1.28 lineage. *medRxiv*, doi:10.1101/2020.12.23.20248598 (2020).
- 1240 22 Cele, S. *et al.* SARS-CoV-2 Omicron has extensive but incomplete escape of Pfizer BNT162b2 elicited
1241 neutralization and requires ACE2 for infection. *medRxiv*, 2021.2012.2008.21267417,
1242 doi:10.1101/2021.12.08.21267417 (2021).
- 1243 23 Thomson, E. C. *et al.* The circulating SARS-CoV-2 spike variant N439K maintains fitness while evading
1244 antibody-mediated immunity. *bioRxiv*, doi:10.1101/2020.11.04.355842 (2020).

- 1245 24 Laffeber, C., de Koning, K., Kanaar, R. & Lebbink, J. H. G. Experimental Evidence for Enhanced Receptor
1246 Binding by Rapidly Spreading SARS-CoV-2 Variants. *Journal of Molecular Biology* **433**, 167058,
1247 doi:10.1016/j.jmb.2021.167058 (2021).
- 1248 25 Planas, D. *et al.* Reduced sensitivity of SARS-CoV-2 variant Delta to antibody neutralization. *Nature* **596**,
1249 276-280, doi:10.1038/s41586-021-03777-9 (2021).
- 1250 26 Ledford, H. The race to make COVID antibody therapies cheaper and more potent. *Nature* **587**, 18,
1251 doi:10.1038/d41586-020-02965-3 (2020).
- 1252 27 Baum, A. *et al.* Antibody cocktail to SARS-CoV-2 spike protein prevents rapid mutational escape seen
1253 with individual antibodies. *Science* **369**, 1014-1018, doi:10.1126/science.abd0831 (2020).
- 1254 28 Copin, R. *et al.* The monoclonal antibody combination REGEN-COV protects against SARS-CoV-2
1255 mutational escape in preclinical and human studies. *Cell* **184**, 3949-3961.e3911,
1256 doi:10.1016/j.cell.2021.06.002 (2021).
- 1257 29 Ku, Z. *et al.* Molecular determinants and mechanism for antibody cocktail preventing SARS-CoV-2
1258 escape. *Nat Commun* **12**, 469, doi:10.1038/s41467-020-20789-7 (2021).
- 1259 30 Binz, H. K. *et al.* High-affinity binders selected from designed ankyrin repeat protein libraries. *Nat*
1260 *Biotechnol* **22**, 575-582, doi:10.1038/nbt962 (2004).
- 1261 31 Walser, M. *et al.* Highly potent anti-SARS-CoV-2 multivalent DARPins therapeutic candidates. *bioRxiv*
1262 (2020).
- 1263 32 Stumpp, M. T., Dawson, K. M. & Binz, H. K. Beyond Antibodies: The DARPins((R)) Drug Platform. *BioDrugs*
1264 **34**, 423-433, doi:10.1007/s40259-020-00429-8 (2020).
- 1265 33 Binz, H. K. *et al.* Design and characterization of MPO250, a tri-specific anti-HGF/anti-VEGF DARPins(R)
1266 drug candidate. *MAbs* **9**, 1262-1269, doi:10.1080/19420862.2017.1305529 (2017).
- 1267 34 Fiedler, U. *et al.* MPO250, a VEGF and HGF neutralizing DARPins((R)) molecule shows high anti-tumor
1268 efficacy in mouse xenograft and patient-derived tumor models. *Oncotarget* **8**, 98371-98383,
1269 doi:10.18632/oncotarget.21738 (2017).
- 1270 35 Steiner, D. *et al.* Half-life extension using serum albumin-binding DARPins(R) domains. *Protein Eng Des*
1271 *Sel* **30**, 583-591, doi:10.1093/protein/gzx022 (2017).
- 1272 36 Copin, R. *et al.* In vitro and in vivo preclinical studies predict REGEN-COV protection against emergence
1273 of viral escape in humans. *bioRxiv*, doi:10.1101/2021.03.10.434834v3 (2021).
- 1274 37 Cathcart, A. *et al.* The dual function monoclonal antibodies VIR-7831 and VIR-7832 demonstrate potent
1275 in vitro and in vivo activity against SARS-CoV-2. *bioRxiv*, doi:10.1101/2021.03.09.434607v1 (2021).
- 1276 38 Trimpert, J. *et al.* The Roborovski Dwarf Hamster Is A Highly Susceptible Model for a Rapid and Fatal
1277 Course of SARS-CoV-2 Infection. *Cell reports* **33**, 108488, doi:10.1016/j.celrep.2020.108488 (2020).
- 1278 39 Walls, A. C. *et al.* Unexpected Receptor Functional Mimicry Elucidates Activation of Coronavirus Fusion.
1279 *Cell* **176**, 1026-1039 e1015, doi:10.1016/j.cell.2018.12.028 (2019).
- 1280 40 Corti, D., Purcell, L. A., Snell, G. & Veasler, D. Tackling COVID-19 with neutralizing monoclonal
1281 antibodies. *Cell* **184**, 3086-3108, doi:10.1016/j.cell.2021.05.005 (2021).
- 1282 41 Falsey, A. R. *et al.* SARS-CoV-2 Neutralization with BNT162b2 Vaccine Dose 3. *N Engl J Med*,
1283 doi:10.1056/NEJMc2113468 (2021).
- 1284 42 Hoffmann, M. *et al.* SARS-CoV-2 variants B.1.351 and P.1 escape from neutralizing antibodies. *Cell* **184**,
1285 2384-2393.e2312, doi:10.1016/j.cell.2021.03.036 (2021).
- 1286 43 Pulliam, J. R. C. *et al.* Increased risk of SARS-CoV-2 reinfection associated with emergence of the
1287 Omicron variant in South Africa. *medRxiv*, 2021.2011.2011.21266068,
1288 doi:10.1101/2021.11.11.21266068 (2021).
- 1289 44 Casalino, L. *et al.* Beyond Shielding: The Roles of Glycans in the SARS-CoV-2 Spike Protein. *ACS Cent Sci*
1290 **6**, 1722-1734, doi:10.1021/acscentsci.0c01056 (2020).
- 1291 45 Andreano, E. *et al.* SARS-CoV-2 escape in vitro from a highly neutralizing COVID-19 convalescent
1292 plasma. *bioRxiv*, doi:10.1101/2020.12.28.424451 (2020).
- 1293 46 Osterrieder, N. *et al.* Age-Dependent Progression of SARS-CoV-2 Infection in Syrian Hamsters. *Viruses*
1294 **12**, doi:10.3390/v12070779 (2020).
- 1295 47 Nouailles, G. *et al.* Temporal omics analysis in Syrian hamsters unravel cellular effector responses to
1296 moderate COVID-19. *Nat Commun* **12**, 4869, doi:10.1038/s41467-021-25030-7 (2021).
- 1297 48 Kumari, P. *et al.* Neuroinvasion and Encephalitis Following Intranasal Inoculation of SARS-CoV-2 in K18-
1298 hACE2 Mice. *Viruses* **13**, doi:10.3390/v13010132 (2021).
- 1299 49 Schoof, M. *et al.* An ultrapotent synthetic nanobody neutralizes SARS-CoV-2 by stabilizing inactive Spike.
1300 *Science* **370**, 1473-1479, doi:10.1126/science.abe3255 (2020).

- 1301 50 Cao, L. *et al.* De novo design of picomolar SARS-CoV-2 miniprotein inhibitors. *Science* **370**, 426-431,
1302 doi:10.1126/science.abd9909 (2020).
- 1303 51 Linsky, T. W. *et al.* De novo design of potent and resilient hACE2 decoys to neutralize SARS-CoV-2.
1304 *Science* **370**, 1208-1214, doi:10.1126/science.abe0075 (2020).
- 1305 52 Walter, J. D., Hutter, C. A. J., Garaeva, A. A., Scherer, M. & Zimmermann, I. Highly potent bispecific
1306 sybodies neutralize SARS-CoV-2. *bioRxiv* (2020).
- 1307 53 Hunt, A. C. *et al.* Multivalent designed proteins protect against SARS-CoV-2 variants of concern. *bioRxiv*,
1308 doi:10.1101/2021.07.07.451375 (2021).
- 1309 54 Jones, B. E. *et al.* LY-CoV555, a rapidly isolated potent neutralizing antibody, provides protection in a
1310 non-human primate model of SARS-CoV-2 infection. *bioRxiv*, doi:10.1101/2020.09.30.318972 (2020).
- 1311 55 Pinto, D. *et al.* Cross-neutralization of SARS-CoV-2 by a human monoclonal SARS-CoV antibody. *Nature*
1312 **583**, 290-295, doi:10.1038/s41586-020-2349-y (2020).
- 1313 56 Shi, R. *et al.* A human neutralizing antibody targets the receptor-binding site of SARS-CoV-2. *Nature*
1314 **584**, 120-124, doi:10.1038/s41586-020-2381-y (2020).
- 1315 57 Starr, T. N. *et al.* Deep Mutational Scanning of SARS-CoV-2 Receptor Binding Domain Reveals
1316 Constraints on Folding and ACE2 Binding. *Cell* **182**, 1295-1310 e1220, doi:10.1016/j.cell.2020.08.012
1317 (2020).
- 1318 58 Zahradnik, J. *et al.* SARS-CoV-2 RBD in vitro evolution follows contagious mutation spread, yet generates
1319 an able infection inhibitor. *bioRxiv*, doi:10.1101/2021.01.06.425392v3 (2021).
- 1320 59 Cao, Y. *et al.* B.1.1.529 escapes the majority of SARS-CoV-2 neutralizing antibodies of diverse epitopes.
1321 *bioRxiv*, 2021.2012.2007.470392, doi:10.1101/2021.12.07.470392 (2021).
- 1322 60 Zivanov, J. *et al.* New tools for automated high-resolution cryo-EM structure determination in RELION-
1323 3. *Elife* **7**, doi:10.7554/eLife.42166 (2018).
- 1324 61 Zheng, S. Q. *et al.* MotionCor2: anisotropic correction of beam-induced motion for improved cryo-
1325 electron microscopy. *Nat Methods* **14**, 331-332, doi:10.1038/nmeth.4193 (2017).
- 1326 62 Zhang, K. Gctf: Real-time CTF determination and correction. *J Struct Biol* **193**, 1-12,
1327 doi:10.1016/j.jsb.2015.11.003 (2016).
- 1328 63 Pettersen, E. F. *et al.* UCSF Chimera--a visualization system for exploratory research and analysis. *J*
1329 *Comput Chem* **25**, 1605-1612, doi:10.1002/jcc.20084 (2004).
- 1330 64 Wrapp, D. *et al.* Cryo-EM structure of the 2019-nCoV spike in the prefusion conformation. *Science* **367**,
1331 1260-1263, doi:10.1126/science.abb2507 (2020).
- 1332 65 Sanchez-Garcia, R. *et al.* DeepEMhancer: a deep learning solution for cryo-EM volume post-processing.
1333 *bioRxiv*, doi:10.1101/2020.06.12.148296 (2020).
- 1334 66 Cianfrocco, M. A., Wong, M., Youn, C. & Wagner, R. in *The Practice and Experience in Advanced*
1335 *Research Computing* (New Orleans, LA 2017).
- 1336 67 Chaudhury, S. *et al.* Benchmarking and analysis of protein docking performance in Rosetta v3.2. *PLoS*
1337 *One* **6**, e22477, doi:10.1371/journal.pone.0022477 (2011).
- 1338 68 Huang, P. S. *et al.* RosettaRemodel: a generalized framework for flexible backbone protein design. *PLoS*
1339 *One* **6**, e24109, doi:10.1371/journal.pone.0024109 (2011).
- 1340 69 Leaver-Fay, A. *et al.* ROSETTA3: an object-oriented software suite for the simulation and design of
1341 macromolecules. *Methods Enzymol* **487**, 545-574, doi:10.1016/B978-0-12-381270-4.00019-6 (2011).
- 1342 70 Laskowski, R. A. & Swindells, M. B. LigPlot+: multiple ligand-protein interaction diagrams for drug
1343 discovery. *J Chem Inf Model* **51**, 2778-2786, doi:10.1021/ci200227u (2011).
- 1344 71 Goddard, T. D. *et al.* UCSF ChimeraX: Meeting modern challenges in visualization and analysis. *Protein*
1345 *Sci* **27**, 14-25, doi:10.1002/pro.3235 (2018).
- 1346 72 Neerukonda, S. N. *et al.* Establishment of a well-characterized SARS-CoV-2 lentiviral pseudovirus
1347 neutralization assay using 293T cells with stable expression of ACE2 and TMPRSS2. *PLoS One* **16**,
1348 e0248348, doi:10.1371/journal.pone.0248348 (2021).
- 1349 73 Wollscheid, B. *et al.* Mass-spectrometric identification and relative quantification of N-linked cell
1350 surface glycoproteins. *Nat Biotechnol* **27**, 378-386, doi:10.1038/nbt.1532 (2009).
- 1351 74 Huang, Y. *et al.* Calibration of two validated SARS-CoV-2 pseudovirus neutralization assays for COVID-19
1352 vaccine evaluation. *Scientific Reports* **11**, 23921, doi:10.1038/s41598-021-03154-6 (2021).
- 1353 75 Matsuyama, S. *et al.* Enhanced isolation of SARS-CoV-2 by TMPRSS2-expressing cells. *Proc Natl Acad Sci*
1354 *U S A* **117**, 7001-7003, doi:10.1073/pnas.2002589117 (2020).
- 1355 76 Nao, N. *et al.* Consensus and variations in cell line specificity among human metapneumovirus strains.
1356 *PLoS One* **14**, e0215822, doi:10.1371/journal.pone.0215822 (2019).

1357 77 Li, H. *et al.* The Sequence Alignment/Map format and SAMtools. *Bioinformatics* **25**, 2078-2079,
1358 doi:10.1093/bioinformatics/btp352 (2009).

1359 78 Bolger, A. M., Lohse, M. & Usadel, B. Trimmomatic: a flexible trimmer for Illumina sequence data.
1360 *Bioinformatics* **30**, 2114-2120, doi:10.1093/bioinformatics/btu170 (2014).

1361 79 Li, H. & Durbin, R. Fast and accurate short read alignment with Burrows-Wheeler transform.
1362 *Bioinformatics* **25**, 1754-1760, doi:10.1093/bioinformatics/btp324 (2009).

1363 80 Wilm, A. *et al.* LoFreq: a sequence-quality aware, ultra-sensitive variant caller for uncovering cell-
1364 population heterogeneity from high-throughput sequencing datasets. *Nucleic Acids Res* **40**, 11189-
1365 11201, doi:10.1093/nar/gks918 (2012).

1366 81 Cingolani, P. *et al.* A program for annotating and predicting the effects of single nucleotide
1367 polymorphisms, SnpEff: SNPs in the genome of *Drosophila melanogaster* strain w1118; iso-2; iso-3. *Fly*
1368 (*Austin*) **6**, 80-92, doi:10.4161/fly.19695 (2012).

1369 82 Gu, Z., Eils, R. & Schlesner, M. Complex heatmaps reveal patterns and correlations in multidimensional
1370 genomic data. *Bioinformatics* **32**, 2847-2849, doi:10.1093/bioinformatics/btw313 (2016).

1371 83 Copin, R. *et al.* In vitro and in vivo preclinical studies predict REGEN-COV protection against emergence
1372 of viral escape in humans. doi:10.1101/2021.03.10.434834 (2021).

1373 84 Corman, V. M. *et al.* Detection of 2019 novel coronavirus (2019-nCoV) by real-time RT-PCR. *Euro Surveill*
1374 **25**, doi:10.2807/1560-7917.ES.2020.25.3.2000045 (2020).

1375 85 Gruber, A. D. *et al.* Standardization of Reporting Criteria for Lung Pathology in SARS-CoV-2-infected
1376 Hamsters: What Matters? *Am J Respir Cell Mol Biol* **63**, 856-859, doi:10.1165/rcmb.2020-0280LE
1377 (2020).

1378 86 Danecek, P. *et al.* Twelve years of SAMtools and BCFtools. *GigaScience* **10**,
1379 doi:10.1093/gigascience/giab008 (2021).

1380 87 Robinson, J. T. *et al.* Integrative genomics viewer. *Nat Biotechnol* **29**, 24-26, doi:10.1038/nbt.1754
1381 (2011).

1382 88 Duvaud, S. *et al.* Expasy, the Swiss Bioinformatics Resource Portal, as designed by its users. *Nucleic*
1383 *Acids Res* **49**, W216-w227, doi:10.1093/nar/gkab225 (2021).

1384 89 Choi, Y., Sims, G. E., Murphy, S., Miller, J. R. & Chan, A. P. Predicting the functional effect of amino acid
1385 substitutions and indels. *PLoS One* **7**, e46688, doi:10.1371/journal.pone.0046688 (2012).

1386 90 Choi, Y. in *Proceedings of the ACM Conference on Bioinformatics, Computational Biology and*
1387 *Biomedicine* 414-417 (Association for Computing Machinery, Orlando, Florida, 2012).

1388 91 Sim, N. L. *et al.* SIFT web server: predicting effects of amino acid substitutions on proteins. *Nucleic Acids*
1389 *Res* **40**, W452-457, doi:10.1093/nar/gks539 (2012).

1390 92 Friedrich, M. *et al.* Preclinical characterization of AMG 330, a CD3/CD33-bispecific T-cell-engaging
1391 antibody with potential for treatment of acute myelogenous leukemia. *Mol Cancer Ther* **13**, 1549-1557,
1392 doi:10.1158/1535-7163.MCT-13-0956 (2014).

1393